SPECTROSCOPIC AND KINETIC INVESTIGATION OF N-OXYGENATION BY CMLI, A DIIRON-CLUSTER-CONTAINING OXYGENASE INVOLVED IN ANTIBIOTIC BIOSYNTHESIS

A DISSERTATION
SUBMITTED TO THE FACULTY OF
UNIVERSITY OF MINNESOTA
BY

Anna Jo Komor

IN PARTIAL FULFILLMENT OF THE REQUIREMENTS
FOR THE DEGREE OF
DOCTOR OF PHILOSOPHY

Advisors: Lawrence Que, Jr. and John D. Lipscomb

April 2017

Acknowledgements

During my graduate career I had the privilege of being advised by two excellent scientists, Professors Larry Que and John Lipscomb. Larry taught me a great deal about scientific rigor and thinking fast on my feet, and supported my interest in biochemistry even as its range superseded that of his research focus. Professor Lipscomb then welcomed me into his laboratory and onto the projects that would form my graduate career. The hours spent dissecting data, debating mechanisms, and discussing the best way to tell a story are what truly make a scientific scholar, and I am deeply grateful.

A million thank yous to current and past members of the Que and Lipscomb groups for their years of support, mentorship, and friendship. Most importantly is Dr. Brent Rivard, who was an invaluable mentor and sounding board for our three years together on the CmlI project. I hope one day we can get the band back together. Thank you to Dr. Rahul Banerjee for his assistance with all things kinetic and for invigorating discussions on a wide range of topics, to Dr. Melanie Rogers for her work in keeping the Lipscomb lab (and especially the stopped-flow instrument) running, and to Dr. Tom Makris for mentorship from near and afar. I would also like to thank the members of the Que BioCave who provided my introduction to biochemistry, Drs. Lisa Engstrom and Andy Fielding. And thanks to my Que laboratory colleagues, with whom I hope to cross paths with in the future: Dr. Caleb Allpress (and Teresa, Nova, and Sasha), Andrew Jasniewski, Dr. Johannes Klein, Dr. Scott Kleespies, Dr. Mayank Puri (and Nirja), Waqas Rasheed, Dr. Greg Rhode (and Louie), Dr. Kathy Van Heuvelen, and Ang Zhou.

I had wonderful collaborators both within and outside of the university: UMN Team CmlI Structural Division heads Andrew Jasniewski (XAS) and Dr. Cory Knoot (XRD), and Mössbauer collaborators Dr. Yisong (Alex) Guo and Ruixi Fan at Carnegie Mellon University. I would also like to thank the professors who served as informal mentors during my time in graduate school, including Mark Distefano, Wendy Gordon, Connie Lu, Will Pomerantz, and Larry Wackett.

I would also like to thank my science literacy collaborators who worked to develop SciMentors. Primary acknowledgements go to program co-founder and co-director Nicole Gagnon, who worked tirelessly with me to get the program off the ground and running, now for three (!) successful years. This success would not have been possible without the wonderful staff at the

Minnesota Literacy Council, especially Kat Aymeloglu and Vadim Rubinchik. Thank you to the many patient and generous volunteers, and to the students, whose dedication and curiosity are an inspiration to us all. And a special thanks to Nancy Thornbury and everyone at the Franklin Learning Center, for introducing me to the incredible warmth of the adult education community, and providing me a home on Saturday mornings for the past six years.

Finally, this work would not have been possible without the love and support of my friends and family. I am extremely lucky to have a family that has always been genuinely interested in my life and work, and this is especially true of my parents, Pat Dutt and Stephen Komor, and my grandparents Judy and Peter Komor. Thank you to my mother and grandmother for the weekly calls that keep me on an even keel in the hard times and share my joy in the good times, and to my entire family for their love and very particular sense of humor, which brings me joy even in the hardest of times. A huge thank you to my bedrock of friendship: Samantha, who shares this journey in a parallel dimension, and Brent and Hannah, for welcoming me into their family. And of course to a very special big hearted bioinorganic chemist, Andy, with whom life is always easier, more interesting, and more joyful.

Dedication

Dedicated to all of the persistent women in my life

Especially

To Lucia, Luul, Nimco and all the other ladies who cheerfully do the work of ten

To Jalene, that you may do the work of one and receive equal praise

To Laurie, who does the work of angels: may it become easier over time

Abstract

Diiron-cluster-containing oxygenases catalyze a wide range of biological reactions. The chemical and biological breadth of the field is still being defined by discovery of new enzymes. The N-oxygenase CmlI, which plays a role in the biosynthesis of the broad-spectrum antibiotic chloramphenicol, is a new entry that brings two significant characteristics to this enzyme class. First, the active oxidant of CmlI is a diferric peroxo species (**P**), in contrast to the high-valent intermediates that often serve as oxidants in the cycles of nonheme iron oxygenases. **P** has unique spectroscopic features and a long lifetime in the absence of substrate ($t_{1/2}$ ~ 3 h at 4 °C, pH 9), which facilitated the discovery of its novel η^1- η^1 or η^1- η^2 diferric peroxo geometry that distinguishes it from the common cis-μ-1,2 geometry and may account for its unique reactivity. Characterization of the structure and function of **P** has led to a new understanding of the role of peroxo species in oxygen activation and insertion chemistry. The second novel aspect of CmlI is the chemistry that it performs, the six-electron conversion of an aryl-amine precursor to the aryl-nitro group of the active antibiotic. Utilization of **P** in single turnover reactions allowed spectroscopic and kinetic characterization of each step of this conversion. The six-electron transformation begins when **P** converts the aryl-amine substrate into an aryl-hydroxylamine, which acts as a mid-cycle reductant to re-reduce and prime CmlI to regenerate **P** by reaction with O_2 while itself being converted to the aryl-nitroso species. The regenerated **P** species then performs the last oxidation to convert the aryl-nitroso into the aryl-nitro group of chloramphenicol. Transient kinetic studies show that the substrate is likely to stay in a single active site during the entire, multistep reaction. Herein is described a new and highly efficient diiron-cluster-mediated N-oxygenase mechanism.

Table of Contents

List of Tables

List of Figures

List of Schemes

Abbreviations

Δ9D, stearoyl-ACP Δ9 desaturase

ADO, aldehyde deformylating oxygenase

AT-L-pAPA, L-pAPA loaded covalently onto the thiolation domain of a CmlP (the NRPS) construct consisting of only the adenylation and thiolation domains

AurF, N-oxygenase on the aureothin biosynthesis pathway

BMM, bacterial multicomponent monooxygenases

CmlI, N-oxygenase on the chloramphenicol biosynthesis pathway

CAM, chloramphenicol

$CmlI^{ox}$, diferric CmlI

$CmlI^{red}$, chemically reduced diferrous CmlI

EPR, electron paramagnetic resonance

hDOHH, human deoxyhypusine hydroxylase

HPLC, high performance liquid chromatography

LCMS, liquid chromatography mass spectrometry

L-pAPA, L-*para* amino phenylalanine

MMOH, hydroxylase component of methane monooxygenase

NH_2-Ar, aryl-amine moiety

NH_2-CAM, D-threo-1-(4-aminophenyl)-2-dichloroacetylamino-1,3-propanediol

NH(OH)-Ar, aryl-hydroxylamine moiety

NH(OH)-CAM, D-threo-1-(4-hydroxylaminophenyl)-2-dichloroacetylamino-1,3-propanediol

$NH(OH)_2$-Ar, aryl-dihydroxylamine moiety

NO-Ar, aryl-nitroso moiety

NO-CAM, D-threo-1-(4-nitrosophenyl)-2-dichloroacetylamino-1,3-propanediol

NO_2-CAM, chloramphenicol

NRPS, nonribosomal peptide synthetase

P, CmlI peroxo species

pABA, *para*-aminobenzoate

pAP, *para*-aminophenol

pNA, *para*-nitroaniline

Q, MMOH diferryl intermediate

R2, subunit of RNR that contains a diiron cluster active site

RNR, ribonucleotide reductase

RRT, reciprocal relaxation time

TMO, undefined toluene monooxygenase

ToMO, toluene/*o*-xylene monooxygenase

X, RNR R2 Fe(III)Fe(IV) intermediate

Chapter 1
Introduction

Oxygen Activation in Biology

The Role of Dioxygen in Biology

Approximately 2.2 billion years ago Earth completed its Great Oxidation Event, in which ambient O_2 levels rose from < 10^{-5} times the current atmospheric level.[1] This precipitous increase in O_2 resulted from the rise of photosynthetic organisms and the serendipitous concomitant decrease in the presence of reduced organic and inorganic species at the surface of the earth, where they could serve as O_2 sinks.[2] Organisms had two options for survival: retreat into anoxic environments, or evolve to mitigate oxygen toxicity while taking advantage of the molecule as a high potential redox couple. This evolutionary pressure resulted in the development of new biological pathways and novel enzymes that allowed for the expansion of the complexity of life.[3] In just one example of the awesome power of dioxygen metabolism, aerobic respiration is estimated to be sixteen times more efficient at generating ATP than anaerobic fermentation.[4] Today, dioxygen is one of the most utilized compounds in the set of chemical reactions that make life possible, its use surpassing even that of important biomolecules such as ATP and NAD^+.[3] Dioxygen serves in two main roles, as a substrate to be incorporated into new products, and as an electron sink and an oxidizing agent to provide driving force for a chemical reaction. Often, it serves both roles at the same time.

The Kinetics and Thermodynamics of O_2 Activation

Activation of dioxygen allows the strong O-O bond to be broken, in preparation for separating the oxygen atoms and inserting one or both into a product. Moreover, it provides a driving force for some of Nature's most thermodynamically uphill reactions. The potential for the complete reduction of dioxygen to two molecules of water is + 0.815 V (Table 1-1), which is thermodynamically very favorable. Fortunately, Nature has provided two stopgaps to prevent runaway spontaneous reduction of O_2 and the concomitant oxidation of all organic molecules in its path. First, although the net four-electron reduction is energetically favorable, the first single electron reduction of O_2 to O_2^- is thermodynamically uphill at -0.33 V. Second, any attempt at a concerted two-electron transfer (thermodynamically downhill at +0.89 V) is kinetically throttled by the difference in spin states between dioxygen and organic molecules. Dioxygen has a triplet spin state whereas most organic molecules have a singlet spin state. The direct reaction between two species of differing spin state requires a spin flip or the conversion of one reactant to an

excited state with a different spin state, both of which are energetically unfavorable and have high activation barriers.

Table 1-1: Standard reduction potentials for O_2 in aqueous solution, pH 7, 25 °C. Values from ref [5].

Reaction	**E°(V) vs. NHE**
$O_2 + e^- \rightarrow O_2^-$	-0.33
$O_2^- + e^- + 2H^+ \rightarrow H_2O_2$	+ 0.89
$H_2O_2 + e^- + H^+ \rightarrow H_2O + OH$	+0.38
$OH + e^- + H^+ \rightarrow H_2O$	+2.31
$O_2^- + 2e^- + 2H^+ \rightarrow H_2O_2$	+0.281
$H_2O_2 + 2e^- + 2H^+ \rightarrow 2\ H_2O$	+1.349
$O_2^- + 4e^- + 4H^+ \rightarrow 2\ H_2O$	+0.815

Due to kinetic constraints, uncatalyzed reactions between O_2 and organic substrates generally occur only via a free radical autoxidation. This process requires an initiator to generate the first organic radical species R·, after which the reaction can proceed in a chain reaction as long as O_2 and the organic substrate are available. No spin inversion is required for the reaction of free radical R· and triplet oxygen, resulting in an efficient pathway that is both kinetically and thermodynamically feasible. However, free radical oxidation lacks specificity regarding both the substrates it oxygenates and the products it yields. Free radical oxidation can wreak havoc in the cell and is so damaging that biology has developed a host of defenses that arrest this process through trapping and neutralization of free radical species. This process presents the opposite problem of the spin state kinetic barrier: it happens too readily and without intention of action.

The Role of O_2-Activating Enzymes

Oxidation thus poses a conundrum for biology: either the process is too slow for the pace of life or too indiscriminate so that it becomes destructive. As a solution, Nature has developed a wide variety of enzymes for which the role is to overcome or direct around these thermodynamic and kinetic barriers, while at the same time ensuring specificity. One such class of enzymes, metalloenzymes, use an active site containing one or more metal atoms to reductively activate dioxygen to produce one of the following oxidants: the superoxide (O_2^{1-}), the peroxide (O_2^{2-}) or the oxide (O^{2-}). These enzymes overcome the initial -0.33 V barrier to transfer an electron to O_2 via a variety of strategies, including the use of reducing metal centers, the formation of a complex

between the metal center and the substrate(s), and controlling other redox-dependent properties such as solvent access and pH. In addition, the design of the enzyme active site ensures that oxidizing power of O_2 is directed only to a specific site on a specific substrate.

Diiron Oxygenases and Related Proteins

Iron Containing Oxygenases and Related Proteins

Iron is the fourth most abundant element in the earth's crust, followed by oxygen, silicon, and aluminum. Given its high environmental availability and its ability to access a wide range of redox states, it is not surprising that Nature chose iron to populate many proteins that facilitate the reaction with dioxygen. The iron (II/III) redox couple has a low redox potential that allows it to interact with a variety of biological reductants to facilitate electron transfer and redox reactions.

One way to categorize the increasingly numerous proteins that have an iron co-factor and dioxygen as a substrate is by the way the protein uses O_2. By this division there are three categories: oxygen transport proteins, oxidase enzymes, and oxygenase enzymes. Oxygen transport proteins simply reversibly bind O_2 for transport to respiring cells. For example, hemerythrin (Hr) is a diiron-cluster-containing protein found in invertebrates that binds O_2 and converts it to the O_2^{2-} form for transport.[6] Oxidase enzymes use O_2 as an electron sink to catalyze oxidation reactions. One example is stearoyl-ACP Δ9 desaturase (Δ9D), which uses the oxidizing power of O_2 to desaturate fatty acids. The O_2 is incorporated into two molecules of water that are produced concomitantly with the desaturation reaction.[7] Finally, oxygenase enzymes incorporate O_2 into the final product. Monooxygenase enzymes incorporate one atom of O_2 into their product; for example, the conversion of methane to methanol is catalyzed by the diiron cluster enzyme soluble methane monooxygenase (sMMO).[8] Dioxygenase enzymes incorporate both atoms of O_2 into the product. Homoprotocatechuate 2,3-dioxygenase, a monoiron containing enzyme, is one such example. This enzyme catalyzes the cleavage of the aromatic ring of its catechol substrate and inserts both atoms of oxygen into the muconic semialdehyde product.[9]

The Biological and Chemical Landscape of Diiron Oxygenases

Iron-containing oxygenases can be further distinguished by the type of iron cofactors present: heme monoiron, nonheme monoiron, and nonheme diiron cluster. Diiron-cluster-containing oxygenases are the least well characterized of the three classes, though their popularity is growing as new chemical and biological functions are discovered. As a class, diiron

oxygenases facilitate so many different biological and chemical functions, across the bacterial, plant, and animal kingdoms, that functional diversity is almost a class hallmark. These enzymes play a role in a wide variety of biological processes, including the primary metabolism of methane by sMMO, control of eukaryotic cell proliferation by human deoxyhypusine hydroxylase (hDOHH), the biosynthesis of the antibiotic chloramphenicol by CmlA/I, and the generation of deoxyribonucleotides by ribonucleotide reductase (RNR). The range of biological functions is matched by the variety of chemistries these enzymes carry out, including hydroxylation of C-H bonds, the generation of radicals, desaturation, deformylation, and, the focus of this work, N-oxygenation. A complete list of chemical and biological functions of known diiron-cluster containing oxygenases and related proteins is found in Table 1-2.

Diiron oxygenases are characterized by two aspects: a diiron cluster in a carboxylate and histidine rich active site, and the ability to activate oxygen to perform a chemical reaction. Other unifying characteristics are increasingly shown to not be universal as more diiron enzymes are discovered and characterized. For example, sMMO houses its diiron cluster in a four α-helix-bundle fold ligated by two histidine and four carboxylate amino acid residues. This fold and ligation was thought to be standard as it is shared by several diiron proteins, including the oxygenases sMMO and cyanobacterial aldehyde deformylating oxygenase (cADO), the oxidase stearoyl-ACP Δ9 desaturate (Δ9D), and the oxygen transport protein hemerythrin. However, the diiron oxygenases hDOHH and CmlA do not share the same protein fold or diiron cluster ligation as the canonical diiron oxygenases such as sMMO. Structural divergence in the diiron oxygenase class is accompanied by mechanistic differences, as is discussed below.

Table 1-2: Chemical and biological function of known diiron-cluster-containing proteins

Protein	Transformation	Chemical Reaction	Biological Function	ref
sMMO	hydroxylation	$O_2 + CH_4 \rightarrow CH_3OH$	Central metabolism	8
AlkB	hydroxylation	alkanes → alcohols	Central metabolism	10
TMOs	hydroxylation	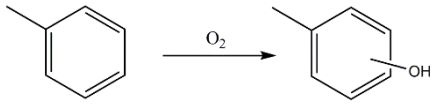	Central metabolism	11-13
CmlA	hydroxylation	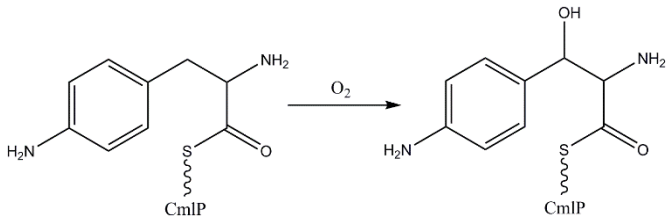	Antibiotic biosynthesis	14
hDOHH	hydroxylation	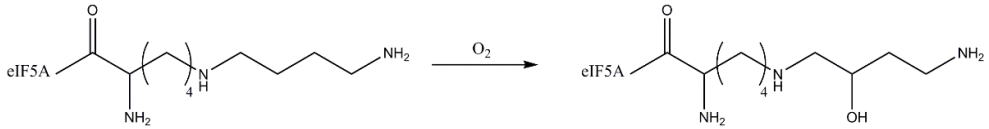	Cell proliferation	15
Clk-1	hydroxylation	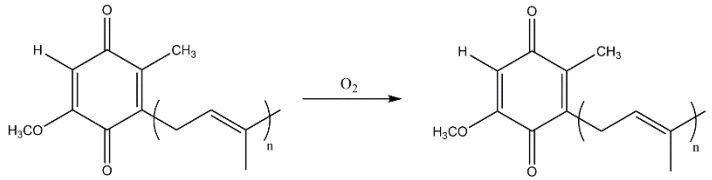	Ubiquinone biosynthesis and mediation of the aging process	16

Protein	Transformation	Chemical Reaction	Biological Function	ref
MiaE	hydroxylation	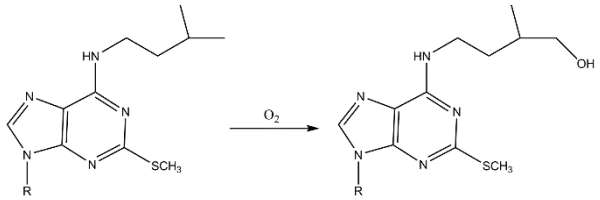	Posttranslational modification of tRNA, specific function unknown	17
CmlI and AurF	N-oxygenation	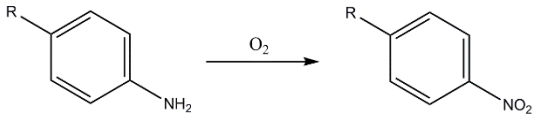	Antibiotic biosynthesis	18-19
RNR R2	radical generation	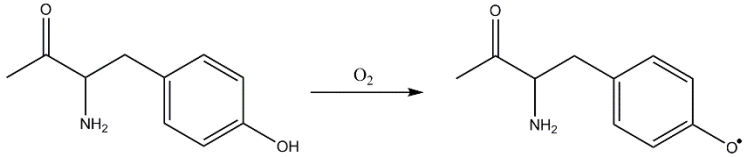	Synthesis of deoxyribonucleotides	20
Δ9D	desaturation	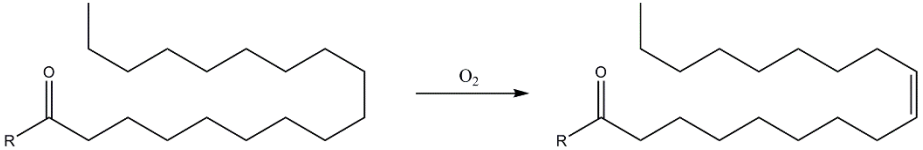	Fatty acid metabolism	7
Hr	reversible O_2 binding	$O_2 \rightleftharpoons O_2^-$	O_2 transport	6

Protein	Transformation	Chemical Reaction	Biological Function	ref
cADO	deformylation	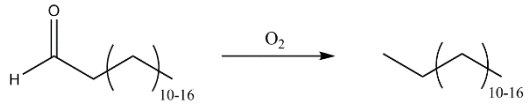	Unknown	21
MIOX	C-C bond cleavage	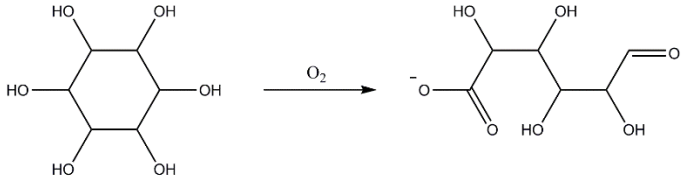	Inositol metabolism, insulin regulation	22
PhnZ	C-P bond cleavage	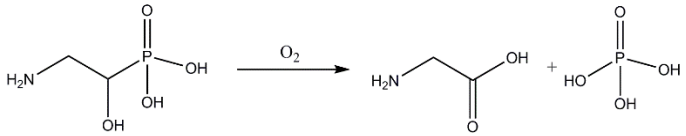	Phosphate metabolism	23

Aims in the Study of Diiron Oxygenases

Study of a particular metalloenzyme, diiron oxygenases included, balances two goals: one, to understand the chemical and biological function of the specific enzyme, and two, to elucidate structure-function correlations and generate mechanistic insight that can be extrapolated to the class of diiron enzymes as a whole. In addition to the particular research goals, diiron enzymes are studied with two applications in mind. The first is to understand their biological function with an eye to either supplementing or inhibiting that function, as the application dictates. For example, the diiron enzyme hDOHH is upregulated in cancer cells and in cells that infected with HIV, so work on this enzyme focuses on developing methods of hDOHH downregulation to treat these diseases.[24] A second example is cADO, found in the cyanobacterium *Prochlorococcus marinus* where it deformylates aldehydes into alkanes. The host (algae) and the product (drop-in ready alkane fuels) of this enzyme make it an ideal component of a biofuels production system.[25] As such, mechanistic work focuses on optimization and upregulation.

The second application aim is to understand how these enzymes perform their particular chemistries so that biomimetic complexes can be synthesized to serve as efficient and environmentally friendly catalysts. Most metalloenzymes function under ambient temperature and pressures, an ideal goal for synthetic catalysts from both an economics and a safety perspective. Furthermore, the reactions they perform are stereospecific and substrate specific, another important industrial requirement. This aim requires both understanding how the metal centers facilitate electron movement and bond making, as well as how the protein architecture surrounding the active site helps ensure specificity and efficiency. For example, sMMO has been studied for decades with the ultimate goal of generating complexes that can cheaply oxidize methane to methanol on an industrial scale. Similarly, enzymes involved in natural product biosynthesis are studied to learn new ways of synthesizing pharmaceuticals, chemical building blocks, and other essential molecules.

Mechanisms of Dioxygen Activation by Diiron Oxygenases

Proposed Mechanism for Dioxygen Activation based on sMMO Catalytic Cycle

A consensus mechanism for oxygen activation and substrate oxidation by diiron oxygenases is based on the cycle of the most studied of the diiron oxygenases, sMMO. As shown

in Figure 1-1, activation begins when the diferrous cluster (MMO^{red}, **I**) binds oxygen and forms via several steps a diferric peroxo (MMO^{P}, **II**) species. The O-O bond in MMO^{P} is then cleaved to form a high valent diferryl closed core species called Q (**III**), which abstracts a H atom from the substrate to initiate the hydroxylation of the substrate C-H bond (**IV**).[26] The cluster must be reduced by two electrons from the ending diferric state (MMO^{ox}, **V**) to perform another turnover. On the cycle of RNR R2, the diiron-cluster-containing subunit of RNR, the high valent active oxidant is instead proposed to be a Fe(III)Fe(IV) open core species X.[27] sMMO and RNR are the only two diiron enzymes with an identified high valent species that serves as the active oxidant, but the ubiquity of high-valent metal oxo oxidants in mononuclear iron enzymes, both heme and nonheme,[28-30] led to the inaccurate conclusion that such oxidants were the invariable choice of oxidation reactions by iron-containing enzymes.

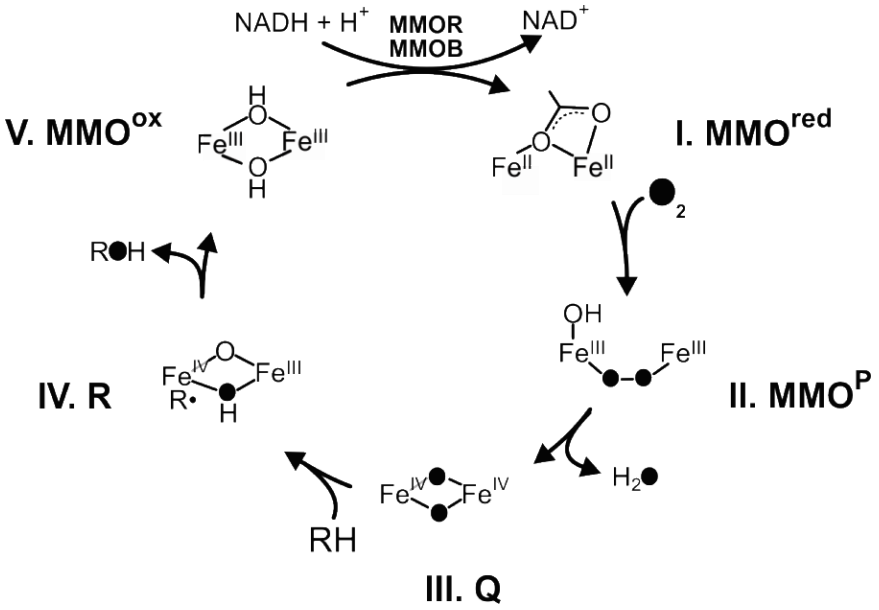

Figure 1-1: Catalytic cycle of soluble methane monooxygenase. The diiron cluster is contained in the hydroxylase component of MMO. MMO contains two additional components, a reductase MMOR and an accessory protein that guides substrate access, MMOB. *In vivo* the reduction of MMO to prime O_2 binding is facilitated by $NADH_2^+$ although *in vitro* the cycle can be primed by chemical reduction as well. Cycle adapted from refs. [31-32]

Peroxo Species Isolated from Diiron Oxygenases

Recent work has shown that the peroxo species, once thought to be exclusively the precursor to the real oxidant workhorse, may in fact be the active oxidant in many diiron oxygenase cycles. While high valent metal oxo species have been studied in depth over the past

two decades, the importance of diferric peroxo species as more than a means to the end has only emerged in the past five years. That diferric peroxo (**P**) species have been overlooked as oxidants in their own right is not surprising given the types of **P** species found in the classical diiron oxygen activating enzymes, sMMO, RNR R2, and Δ9D. Due to the short half-life of MMO^{P}, (0.3 – 11 s, depending on sMMO bacterial source),[33,34] characterization is limited to UV-vis and Mössbauer spectroscopy (see Table 1-3 for a compilation of known diiron peroxos and their spectroscopic parameters). MMO^{P} is overshadowed by interest in Q, which does the impressive job of breaking an 104 kcal/mol bond to convert methane into methanol.[35] MMO^{P} is not capable of oxidizing methane or other strong C-H bonds, but can oxidize some electron-rich substrates.[36] The structure of MMO^{P}, described by the binding mode of O_2, is proposed to be cis μ-1,2 (Figure 1-2) based on theoretical calculations and comparison of spectroscopic parameters to those of crystallized synthetic complexes (*vide infra*).[37] Peroxo species have also been observed in the enzyme toluene/o-xylene monooxygenase (ToMO), which falls into the diiron oxygenase subclass bacterial multicomponent monooxygenases (BMM) with MMO. $ToMO^{P}$ isolated from wild type ToMO is a short-lived ($t_{1/2}$ ~ 15 s) diferric species that appears to be active towards arene substrates, but is identified only by Mössbauer spectroscopy, with no corroborating spectroscopic data (not even UV-vis, curiously $ToMO^{P}$ has no optical signature).[38] The Mössbauer parameters significantly differ from those observed for MMO and other cis μ-1,2-diferric peroxos, and the structure remains unknown. An inactive mutant form T201S $ToMO^{P}$ has also been generated, and the spectroscopic signatures of this species match those of MMO.[39]

The peroxo species of RNR R2 (RNR^{P}) is also short lived, though a double mutation of an iron ligand and a surface residue responsible for electron transfer (W48F/D84E) yielded a longer-lived species that has been more extensively characterized. The longer lifetime allowed for resonance Raman studies which also characterized this **P** species as cis μ-1,2 peroxo.[40-42] A **P** species is isolated in Δ9D when the enzyme is pre-incubated with substrate prior to O_2 addition. $\Delta9D^{P}$ is long lived (half-life ~ 30 min at 25 °C), allowing a suite of spectroscopic techniques to be applied in its characterization. UV-vis, Mössbauer, and resonance Raman spectroscopies indicated a cis μ-1,2 binding mode. However, $\Delta9D^{P}$ is not active; in the presence of substrate, it undergoes autodecay to yield two equivalents of water instead of performing its native desaturase reaction. [43]

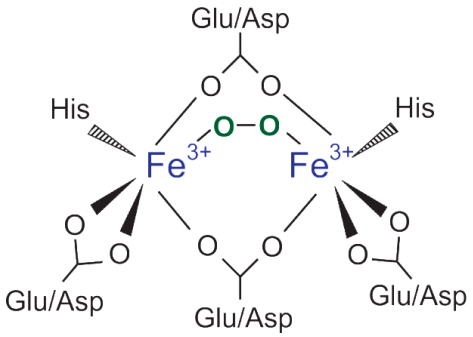

Figure 1-2: Cis-μ-1,2-diferric peroxo geometry.

The results of analysis of **P** species from the three classic diiron enzymes suggested: first, that diiron peroxo intermediates universally assume the cis μ-1,2 O_2 binding mode, and second, with the possible exception of the putative wild type ToMO$^{\mathbf{P}}$, they are not oxidants on the native catalytic cycles. This paradigm was first definitively broken in 2009, with the discovery of a hyperstable ($t_{1/2}$ > 24 h at room temperature) cis μ-1,2 peroxo species from hDOHH that reacts directly with substrate and therefore is presumed to be the active intermediate.[15, 44] This enzyme further broke the mold with a HEAT repeat fold and 4-his 2-carboxylate diiron cluster ligation.[45] In 2013, another example of a diferric peroxo serving as the active oxidant was reported. This peroxo species, on the cycle of cADO, was spectroscopically characterized as a peroxy-hemiacetal species, or a diferric peroxo bound to substrate.[46]

Geometric assignments of enzymatic **P** intermediates are largely based on the comparison of their spectroscopic parameters to those of crystallized synthetic **P** species. There are four synthetic diferric peroxo species that have been crystallized and spectroscopically characterized (Table 1-3). These complexes are built with N and O rich ligands to mimic the histidine and carboxylate rich active sites of the enzymes, and all are symmetric with a cis μ-1,2 O_2 binding mode. These synthetic complexes have been extensively spectroscopically characterized, giving a set of spectroscopic parameters to which enzymatic **P** species can be compared. However, these biomimetic synthetic peroxos are fairly stable and unreactive, and therefore do not provide much insight into the mechanism of oxidation by a **P** species.

In addition to the crystal structures of synthetic diferric peroxo intermediates, three crystal structures for enzymatic **P** species have been published: hDOHH,[45] T4MO,[47] and CmlI.[48] The hDOHH crystal structure confirms the cis μ-1,2 O_2 binding mode earlier determined by resonance Raman studies, although the Fe-Fe bond distance in the structure suggests that the crystallized enzyme may have been cryoreduced by the x-ray beam, and so the specific distances should be viewed with some skepticism. Crystals of T4MO$^{\mathbf{P}}$ were prepared by soaking crystals of diferric T4MO in H_2O_2, and the resulting O_2 binding mode is cis-μ-1,2. T4MO is active via the

peroxide shunt, though the reaction is ~600 times slower than that carried out with the native biological reductants and O_2. This lower reactivity suggests that the H_2O_2-generated T4MO^P may not be a native active species. The crystallized CmlI **P** also shows a cis μ-1,2 O_2 binding mode, but the species does not react with substrate and consequently is not thought to be the active or native peroxo. Of the three crystallized enzymatic **P** species, only hDOHH$^{\mathbf{P}}$ is shown to be active on the native cycle. The high stability and low reactivity of many of the cis μ-1,2 **P** species, both synthetic and enzymatic, combined with new evidence that enzymatic **P** species are, on some cycles, the active oxidant, suggest that this geometry may not be the active species.

Diferric Peroxo Species Produced by CmlI

In 2015, Lipscomb and coworkers published the first report of a unique **P** species from the newly discovered diiron enzyme CmlI. CmlI$^{\mathbf{P}}$ is the active oxidant on the enzymatic cycle and its unique spectroscopic features suggest a completely new O_2 binding mode. In addition, CmlI$^{\mathbf{P}}$ can be prepared in way that renders it highly stable in the absence of substrate while maintaining reactivity in the presence of substrate, thus enabling spectroscopic and mechanistic characterization, respectively. The study of CmlI$^{\mathbf{P}}$, and the overall CmlI mechanism, represents a unique opportunity to begin to understand the role of diferric peroxos beyond a simple conduit to a high valent oxidant. In addition, the novelty of the enzyme CmlI extends beyond its unusual oxidant to also include the chemical transformation it directs, as discussed in the next section.

Table 1-3: Spectroscopic parameters and proposed structure of enzymatic diiron peroxos and crystallized synthetic peroxos.

Species	λ_{max}, nm (ε, mol^{-1} cm^{-1})	δ, mm/s (ΔE_Q, mm/s)	ν (O-O) cm^{-1}	Proposed structure	Ref(s)
MMOH^P *M. capsulatus* (Bath)	420 (4000), 725 (1800)	0.66 (1.51)		cis μ-1,2	[34]
MMOH^P *M. trichosporium* (OB3b)	700 (2500)			cis μ-1,2	[33]
ToMO	not observed	0.54 (0.67)			[38]
T201S ToMO	675 (1500)	0.67 (1.51)			[39]
Δ9D^P	700 (1100)	0.68 (1.90), 0.64 (1.06)	898	cis μ-1,2	[43, 49]
RNR R2^P (mouse)	700 (1500)	0.63 (1.74)		cis μ-1,2	[50]
W48F/D84E RNR R2^P (*E. coli*)	700 (1800)	0.63 (1.58)	870	cis μ-1,2	[41, 51]
cADO^P	450 (1200)	0.48 (0.49), 0.55 (1.23)		μ-η^2-η^2 or peroxoyhemiacetal	[46]
CmlI^P	500 (500)	0.62 (-0.23), 0.54 (-0.68)	791	μ-η^1-η^2 or μ-η^2	[52] and this work
AurF^P	500 (500)	0.54 (-0.66), 0.61 (0.35)			[53]
hDOHH^P	630 (1500)	0.55 (1.16), 0.58 (0.88)	855	cis μ-1,2	[15]
Fe_2(Ph-BIMP)(O_2)(O_2CPh)$^{2+}$	500 – 800 (1700)	0.58 (0.74), 0.65 (1.70)		cis μ-1,2	[54]
Fe_2(N-Et-hptb)(O_2)($OPPh_3$)$_2^{3+}$	588 (1500)	0.52 (0.72)	900	cis μ-1,2	[55-56]
$Fe_2(Tp^{iPr2})_2(O_2)(CO_2CH_2C_6H_5)_2$	694 (2650)	0.66 (1.40)		cis μ-1,2	[57]
$Fe_2(6Me_2\text{-}BPP)_2(O_2)(O)^{2+}$	644 (3000)	0.5 (1.31), 0.5 (1.46)	847	cis μ-1,2	[58]

N-oxygenase Enzymes

Nitro-Containing Natural Products

There are over 200 known nitro-containing natural products, and those that have been functionally characterized show a promising array of antibiotic, antifungal, and cytostatic properties.[59] The correct incorporation of the nitro group is essential for function. In the past 20 years, the gene clusters aryl-nitro-containing natural products have been mapped, but the method by which the aryl-nitro moiety is synthesized is not well understood. The nitro group may be incorporated into a natural product either by direct nitration or by oxidation of an amine precursor. Enzymes that facilitate the latter transformation are known as N-oxygenase enzymes, and known members of this class are shown in Table 1-4. All contain some type of redox active co-factor, and several identified employ nonheme iron for that purpose.

Biosynthesis of Chloramphenicol, an Aryl-Nitro-Containing Natural Product

Chloramphenicol is perhaps the best studied aryl-nitro-containing natural product, on account of its commercial availability as a broad spectrum antibiotic used to treat a wide variety of bacterial infections. The mechanism of action is arresting protein synthesis by binding to the peptidyl transferase center of the 50S ribosomal subunit.[60] First prescribed in 1948, its use today is restricted to serious cases in which other antibiotics have failed due to toxicity of chloramphenicol in the form of aplastic anemia and bone marrow suppression. However, there is resurgent interest in chloramphenicol due to its wide efficacy in light of the global antibiotic resistance crisis.[61-62] In addition, the general interest in natural products has brought this and other naturally derived antibiotics back into the research sphere.

Chloramphenicol is synthesized in *Streptomyces venezuelae* by the non-ribosomal peptide synthetase (NRPS) CmlP and associated tailoring enzymes. A biosynthetic scheme is shown in Figure 1-3, although the exact order of the tailoring reactions in the later stages of synthesis is not definitively determined.[63-65] CAM biosynthesis begins with a derivative of the shikimate pathway, a metabolic route used by bacteria and fungi for the assembly of aromatic metabolites. The resultant *p*-aminophenylalanine is modified by a non-ribosomal peptide synthetase (NRPS) system and several tailoring enzymes, of which CmlI is the last. There are two diiron oxygenases present on this pathway; β-hydroxylase CmlA, which is responsible for hydroxylating CmlP-bound *p*-aminophenylalanine midway through the biosynthetic pathway, and

CmlI, which is an N-oxygenase that does the last step in chloramphenicol biosynthesis and acts on the free, not CmlP-bound, precursor.

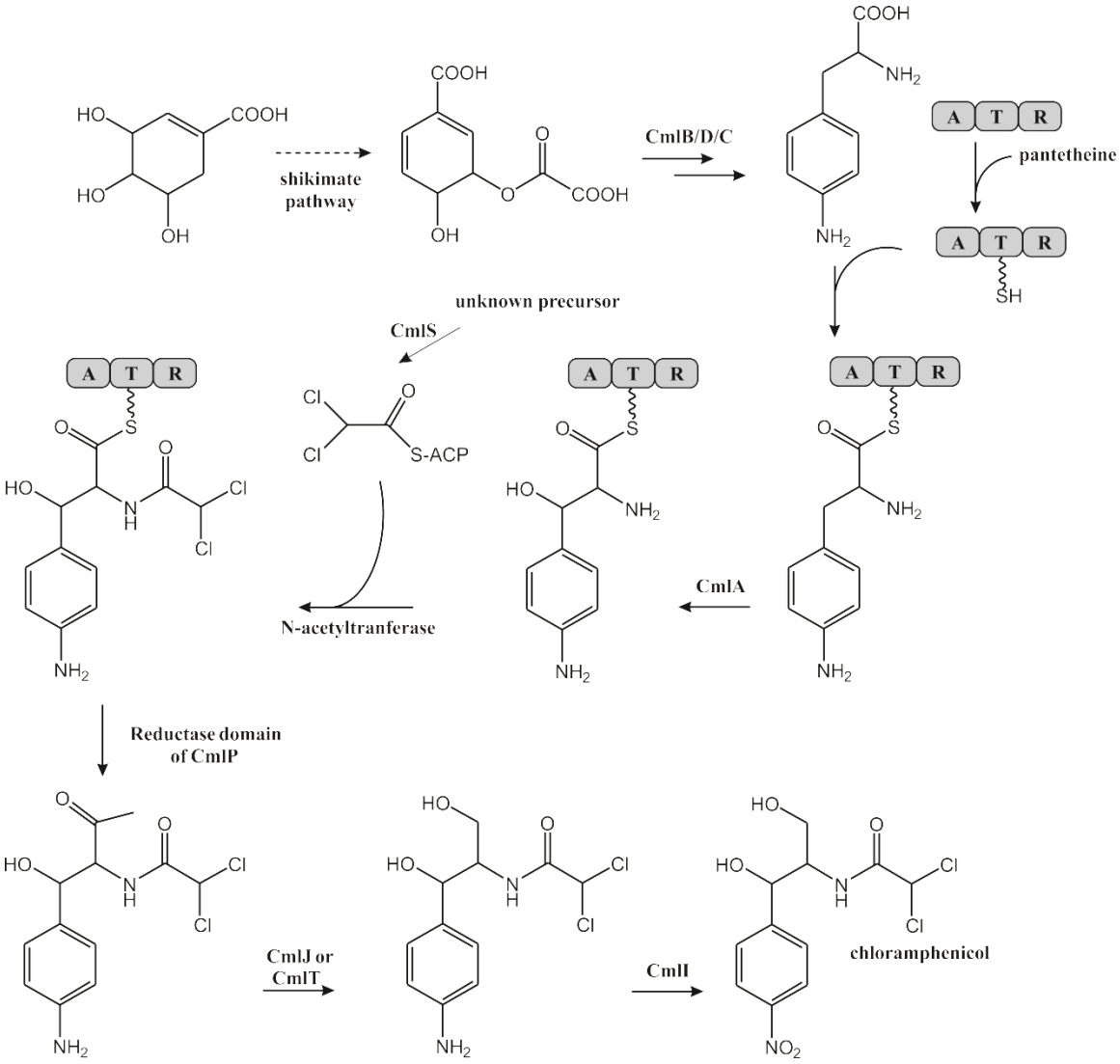

Figure 1-3: Chloramphenicol biosynthetic pathway based on refs. [63, 65]

N-oxygenases with Nonheme Iron Co-factors

There are only three N-oxygenases shown to do the full six-electron conversion of an amine precursor to the nitro-containing final product, all of which utilize iron cofactors. Two of these enzymes employ a diiron cofactor: AurF acts on a precursor of the antimicrobial natural product aureothin, catalyzing the oxidation of aminobenzoate to nitrobenzoate,[18] and CmlI performs the last step in the biosynthesis of the antibiotic chloramphenicol (CAM).[63] The third six-electron N-oxygenase is PrnD, which utilizes a monoiron cofactor in conjunction with a Rieske cluster, and catalyzes the final step in the biosynthesis of the antifungal natural product

pyrrolnitrin.[66] Not much is known about how these enzymes catalyze the full six-electron oxidation of their respective aryl-amine substrates and the reaction is especially puzzling given that these types of enzymes can generate oxidants that can catalyze, at most, a two electron oxidation.

Table 1-4: Known N-oxygenase enzymes: source organism, function, and redox co-factor.

Name	Organism	Reaction	Co-factor	Ref
AurF	Bacterial: *Streptomyces thioluteus*	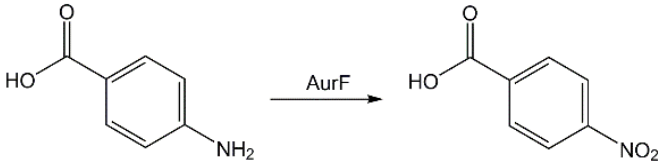	diiron	**67**
RHAI	Bacterial: *Rhodococcus jostii*	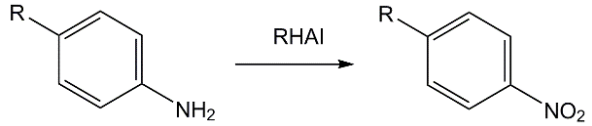	diiron	68
PsAAO	Bacterial: *Pseudomonas syringae*	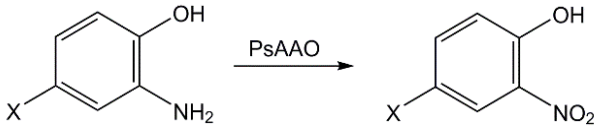	diiron	69
CmlI	Bacterial: *Streptomyces venezuelae*	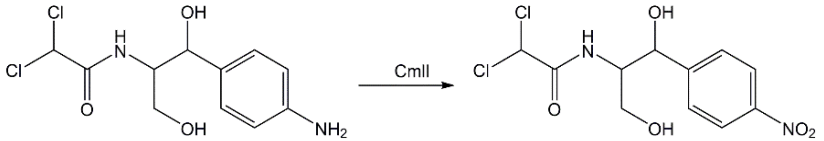	diiron	**19**
PrnD	Bacterial: *Pseudomonads*	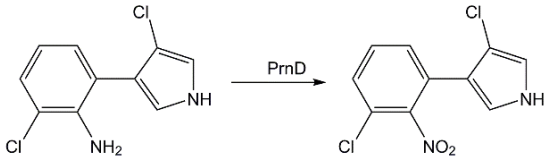	monoiron Rieske	**66**

Name	Organism	Reaction	Co-factor	Ref
NocL	Bacterial: *Nocardia uniformis*	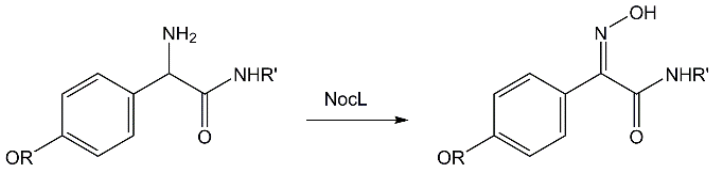	P450	70
KijD3	Bacterial: *Actinomadura kijaniata* and *Micromonospora chalcea*	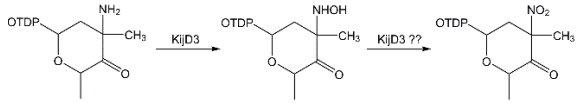	flavin	71
Senecionine N-oxygenase (SNO)	Plant: *Crotalaria scassellatii* Insect: haemolymph of specialized insects (i.e. Arctiids, Lepidoptera)	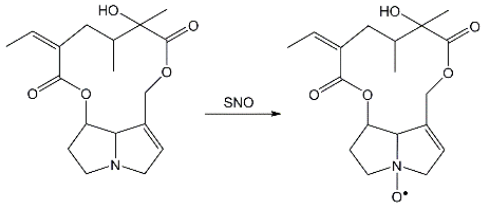	flavin	72
Flavin monooxygenase (hFMO)	Human	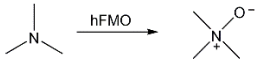	flavin	73

Diiron Cluster Containing N-oxygenases

In 2004 Hertweck and coworkers discovered an unusual enzyme on the biosynthetic pathway of the metabolite aureothin.[18] Aureothin is a natural product produced by the soil bacterium *Streptomyces thiolutues*, and contains an aryl-nitro moiety.[74] Analysis of the gene cluster did not reveal any genes correlating to enzymes known to do nitro insertion reactions, nor standard redox enzymes that might perform an oxidation. Gene deletion mutants and subsequent product assays revealed the responsible enzyme, named AurF, was indeed an "N-oxygenase" rather than a nitration enzyme.[18] AurF is part of a polyketide synthetase system in which it catalyzes a mid-pathway reaction, the conversion of *p*-aminobenzoate to *p*-nitrobenzoate. In 2006 Zhao and co-workers showed that AurF was metal-cofactor dependent and likely part of the diiron oxygenase family.[75] Although there was for a time a debate in the literature about whether AurF was perhaps a dimanganese enzyme,[76-77] it has been shown since, via both crystal structure and activity assays, that AurF contains a diiron cofactor.[78]

In 2012 Zhao and coworkers isolated a putative oxidase from the chloramphenicol biosynthesis pathway called CmlI, and showed that this enzyme too is a diiron N-oxygenase. CmlI is the ultimate enzyme on the chloramphenicol biosynthesis pathway found in the soil bacterium *Streptomyces venezuelae*, where it converts D-threo-1-(4-aminophenyl)-2-dichloroacetylamino-1,3-propanediol (NH_2-CAM) to the final chloramphenicol (CAM) product. Discovery of CmlI as a diiron enzyme was made possible by the elucidation of the CAM biosynthesis pathway, largely undertaken by Vining and co-workers (Figure 1-3).

There exist a small handful of additional diiron N-oxygenases that have been isolated for initial characterization. These include RHAI and PsAAO, which were identified in 2011 and 2015, respectively, by in-silico search for AurF gene homologs.[68-69] The sequence identity to AurF for RHAI and PsAAO are 38% and 25%, respectively, and both are adjacent to the gene for a putative NRPS. RHAI was isolated from the soil bacterium *Rhodococcus jostii*, and PsAAO was isolated from the plant pathogenic bacterium *Pseudomonas syringae*. The absorption spectrum of the purified enzymes are consistent with that of the diferric state of a diiron oxygenase, but no other structural or spectroscopic data is available. The native substrate for RHAI is proposed to be *p*-aminobenzoate, although in vitro the enzyme shows preference for aminophenol substrates. The true substrate for PsAAO is also unknown, although it is presumed to be a relatively small substituted aryl-amine, as the enzyme shows preference for 5'-substituted aminophenols.

Protein blast searches show that there are likely hundreds of additional AurF and CmlI homologs. Those that have been characterized so far are present in soil bacteria and/or plant pathogenic bacteria, and are associated with polyketide synthase or non-ribosomal peptide synthetase operons. [18, 68-69] This finding indicates that diiron enzymes play a significant role in natural product biosynthesis.

Structural Characteristics of CmlI and AurF

CmlI and AurF are part of the ferritin-like superfamily of diiron proteins, the characteristics of which include a diiron cluster located inside a four α-helix bundle, and histidine and carboxylate metal center ligands. CmlI is a homodimer made up of two 10 α-helix monomers, and has a 22 Å separation between the diiron clusters housed in each monomer (Figure 1-4A). CmlI has been crystallized in the diferric and diferrous forms as CmlIΔ33, an N-terminally truncated form of CmlI that shows the same activity as the wild-type enzyme. Crystallization of wild type CmlI was not successful.[48] The crystal structures of AurF are quite similar with those of CmlI, reflecting the 37% sequence identity between the two proteins and the identification of the two as homologs. Wild type AurF has been crystallized in the diferric resting state[67, 78] and in complex with its product *p*-nitrobenzoic acid.[78]

The active sites of AurF and CmlI nearly overlay, both containing a diiron cluster ligated by three histidine and four carboxylate residues (Figure 1-4C). Drawing conclusions based on structural differences between the two active sites as shown in their respective oxidized crystals is not straight forward, as it is likely that the CmlI structure is of a form that is not catalytically active. However, the major difference observed in these two structures is the position of Glu236/227. In AurF E227 is bound bidentate to a single Fe atom while in CmlI E236 is swung out to bridge between the two iron atoms and occupy the space where in AurF there exists a single atom bridge. The CmlI crystal structure does not show any oxo bridge between the two iron atoms. However, the spectrum of diferric CmlI in solution includes an UV-vis absorption band with a shoulder at ~375 nm, a feature characteristic of such a bridge and ascribed to a Fe(III)-O charge transfer band in diiron proteins such as Hr and CmlA.[79] Furthermore, XAS analysis of CmlI shows a solvent-derived bridge in the diferric and diferrous forms of the enzyme (unpublished data). Thus, the rotation of E236 in CmlI (relative to its corollary's position in

AurF) may be an artifact of crystal packing, or it may represent an alternative conformation related to the regulation of oxygen activation in the system.

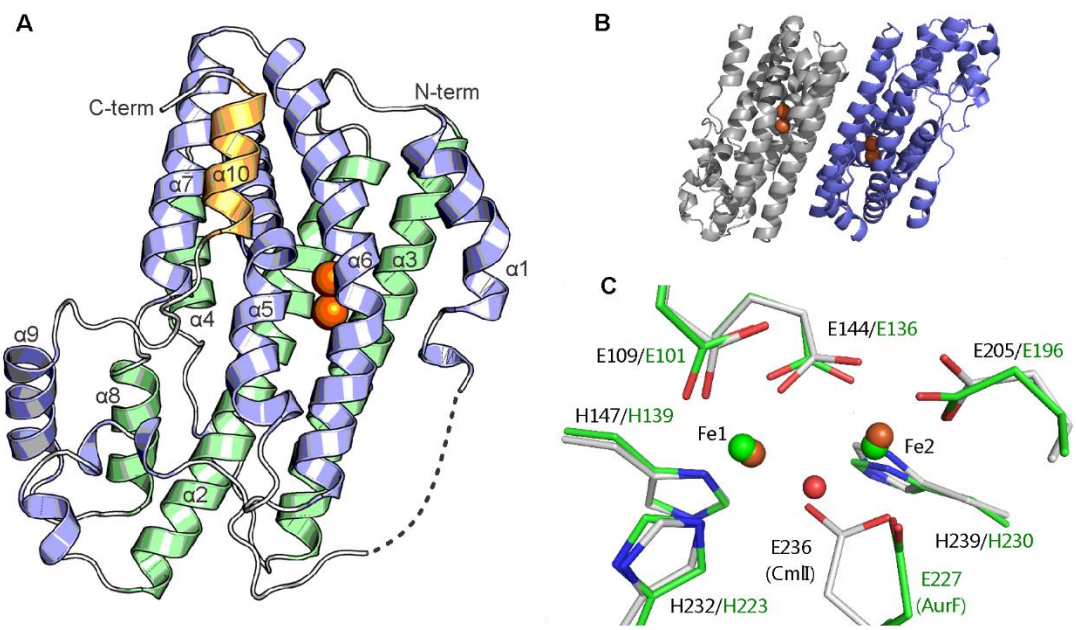

Figure 1-4: Crystal structure of CmlIΔ33. A, structure of one monomer of the homodimer CmlI showing the diiron center surrounded by 10 α-helices. The dotted line indicates a disordered set of residues between K52 and F62. Protein ligands are located on helices α2, α3, α5, and α6. B, the CmlI dimer with iron atoms shown in orange. C, Overlay of the active sites of CmlI (grey) and AurF (green). The solvent-derived bridge observed in the AurF structure is shown as a red sphere. The iron atoms are shown as orange spheres (CmlI) or green spheres (AurF). Adapted from ref. [48] PDB: 5HYH.

Mechanisms of N-oxygenation Mediated by Nonheme Iron Oxygenases

General Mechanism for Enzymatic N-oxygenation

Synthetic work on the conversion of an amine substituent into a nitro species has focused on the reverse reduction reaction carried out by electrochemistry. Early work defined the six electron reduction reaction as three successive two-electron transfers to form first a nitroso or dihydroxylamine intermediate, followed by a hydroxylamine and finally the amine.[80-82] The proposal for the oxidation mechanism is simply the reduction mechanism in reverse (Figure 1-5).

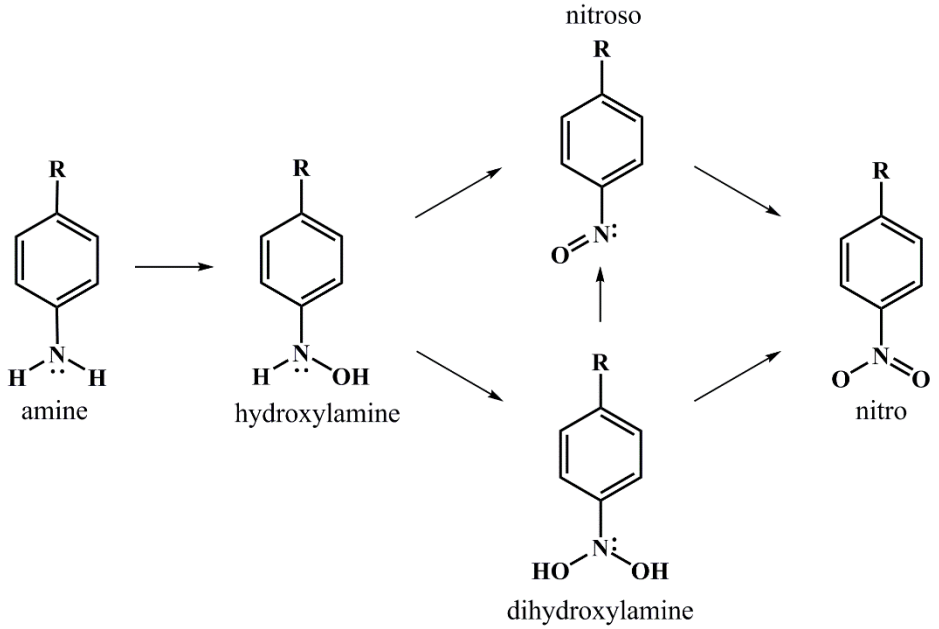

Figure 1-5: Basic scheme for the six electron oxidation of an aryl-amine to an aryl-nitro species. The four electron oxidized species may be either a nitroso or a dihydroxylamine species, and the two may be interconvertible depending on the reaction conditions.

Product Analysis-Based Investigations into Biological N-oxygenation

Investigation into the mechanism of N-oxygenase enzymes began in the mid-2000s by natural product chemists who were interested in the unusual properties and structures of aryl-nitro molecules. As such, the characterization of the cycle began with the identification of the small molecule intermediates between the aryl-amine and aryl-nitro species. The first intermediate on the cycle, aryl-hydroxylamine, is the logical two electron oxidized postcursor of an aryl-amine. Hydroxylamine has been identified as the first intermediate in the cycles of AurF,[75, 83] CmlI,[19] and PrnD,[84] both by isolation of the compound from the native reaction and by direct reaction of aryl-hydroxylamine with the purified enzyme.

A second two electron oxidation would yield either an aryl-nitroso or aryl-dihydroxylamine species, both of which have been proposed as the second intermediate.[75, 84-85] Analysis of this step is complicated by the reactivity of both candidates. Dihydroxylamines are unstable in aqueous solution and have yet to be isolated in any N-oxygenase reaction. This species is proposed based on process of elimination and failure to observe an aryl-nitroso species in a particular reaction. Aryl-nitroso species are more stable, but are prone to dimerize to form

azoxy species, and are the decay product of aryl-hydroxylamines under acidic conditions.[83, 86] Thus, care must be taken with the reaction workup to identify the correct intermediate. Failing to isolate the aryl-nitroso intermediate as part of the reaction, as some research groups report, only indicates that the intermediate does not accumulate under their specific reaction conditions, not that it does not form.

Analysis of only the small molecules would not eliminate the possibility that both proposals are correct, i.e. that aryl-dihydroxylamine is formed first, by oxygenation, followed by a dehydration to form the nitroso. A clever study by Zhao and co-workers sought to differentiate between these possibilities (Figure 1-6). They added unlabeled $NH^{16}OH$-benzoate to a vial of *E. coli* over-expressing AurF under an $^{18}O_2$ atmosphere.[75] If the reaction proceeded through a dihydroxylamine followed by a dehydration, the resulting product should be a mix of $N^{18}O_2$-benzoate and $N^{18}O^{16}O$-benzoate. However, only the latter was observed, indicating the absence of a dehydration step to remove the original ^{16}O. Thus, simple product analysis supports the hypothesis that diiron enzymes convert aryl-amines to aryl-nitros via aryl-hydroxylamine and aryl-nitroso intermediates, with no interceding aryl-dihydroxylamine. However, other researchers maintained that aryl-nitrosos are not part of the pathway and so the scientific debate as to the correct pathway for N-oxygenation continued.[85]

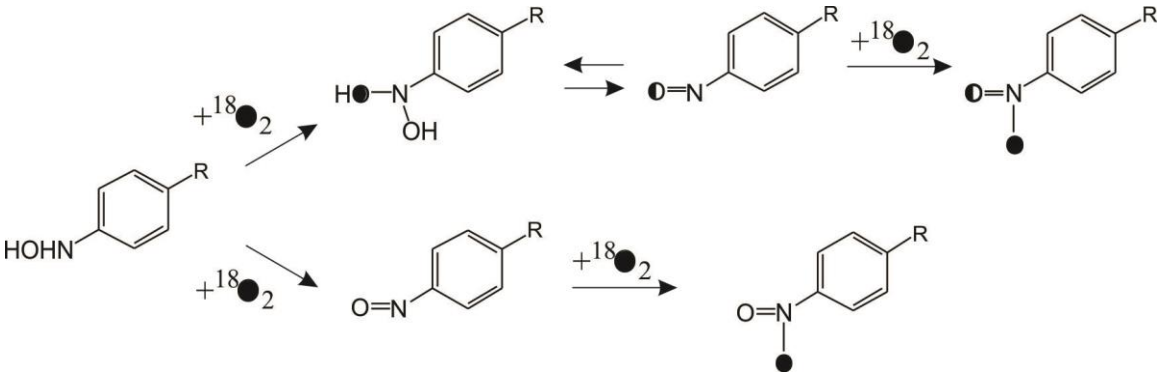

Figure 1-6: Experimental determination of the four electron oxidized intermediate on the pathway to the nitrobenzoate product as catalyzed by AurF. The reaction begins by adding hydroxylamine benzoate to a degassed vial of AurF-expressing *E. coli*, followed by the addition of $^{18}O_2$. If dihydroxylamine benzoate is on the pathway, then the final products should be a mixture of $N^{18}O_2$-benzoate and $N^{18}O^{16}O$-benzoate (top pathway). If no aryl-dihydroxylamine is present, then the product should be only and $N^{18}O^{16}O$-benzoate (bottom pathway). The latter case was observed experimentally.

Role of the Diiron Cluster in Biological N-oxygenation

Studying the N-oxygenation mechanism purely from the organic substrate point of view is restrictive due to the instability of the intermediates and the limited number of analytical methods available. Being able to follow the concurrent changes in the diiron cluster as the reaction progresses provides a whole new view into the cycle. In particular, isolating the active species in the diiron N-oxygenation reactions opens up many experimental possibilities.

The explicit role of the diiron center in N-oxygenation was not thoroughly investigated until the active oxidant was isolated in the diiron reaction, reported in 2009 for AurF[53] and in 2015 for CmlI.[52] In both cases the active oxidant appears to be a diferric peroxo species for which the spectroscopic features differ from the canonical diferric peroxos of MMO, RNR, and hDOHH. These unusual intermediates have a broad Fe(III) – O MLCT band extending from the UV out to 600 nm, and an orange color when concentrated to the mM regime. The unique electronic features translate to a new type of structure for diferric peroxos. In addition, both peroxo intermediates have long half-lives, CmlI$^{\mathbf{P}}$ particularly so. At 4 °C the half-life of CmlI$^{\mathbf{P}}$ is ~3 hours (pH 9, 50 mM Bicine) while the half-life of AurF$^{\mathbf{P}}$ is 7 min, reported at room temperature (20 °C, pH 7.5, 50 mM HEPES). It is presumed the two species might have similar half-lives if generated under the same conditions, given the structural similarity of the protein and the nearly identical spectroscopic features of the **P** species.

A diferric peroxo species is a two electron oxidant, so initial hypotheses proposed a three sequential oxidation mechanism, where three consecutive **P** species facilitate the six-electron transfer required for the aryl-amine to aryl-nitro conversion (Figure 1-7, I). In 2011 Bollinger and co-workers endeavored to track the diiron cluster by Mössbauer as it proceeded through the N-oxygenation cycle.[85] AurF^{P} is relatively long lived and accumulates to detectable concentrations, and so at least three states of the diiron cluster can be distinguished by Mössbauer: diferric, diferric peroxo, and diferrous. As a result of this study, a new type of mechanism for N-oxygenation was proposed that invoked an organic substrate-based reductant mid cycle. In summary, the reaction proceeds as follows (Figure 1-7, II): the first two steps are identical two electron oxidations by AurF$^{\mathbf{P}}$ to yield the aryl-hydroxylamine and aryl-dihydroxylamine in succession. In the last step, the aryl-dihydroxylamine acts as a reducing agent to reduce the AurF diferric cluster to diferrous, while itself being oxidized to the final aryl-nitro product. Thus, the cycle ends with the enzyme already primed to accept O_2 to form AurF$^{\mathbf{P}}$ for the next turnover.

This new mechanism provided new insight into the role of the diiron cluster in multi-electron oxidation reactions, but many questions remained. Does the substrate stay in the active site for the entire reaction, or does it leave after the first $AurF^{P}$ is "spent" to find another $AurF^{P}$ for the second oxidation? Is dihydroxylamine really the four electron oxidized organic intermediate, or is nitroso just not accumulating to detectable levels? Are all of the O_2 atoms derived from the $AurF^{P}$ species (and therefore from O_2) or do one or both come from water? And, is this a consensus mechanism for diiron N-oxygenation, or an anomaly specific to AurF?

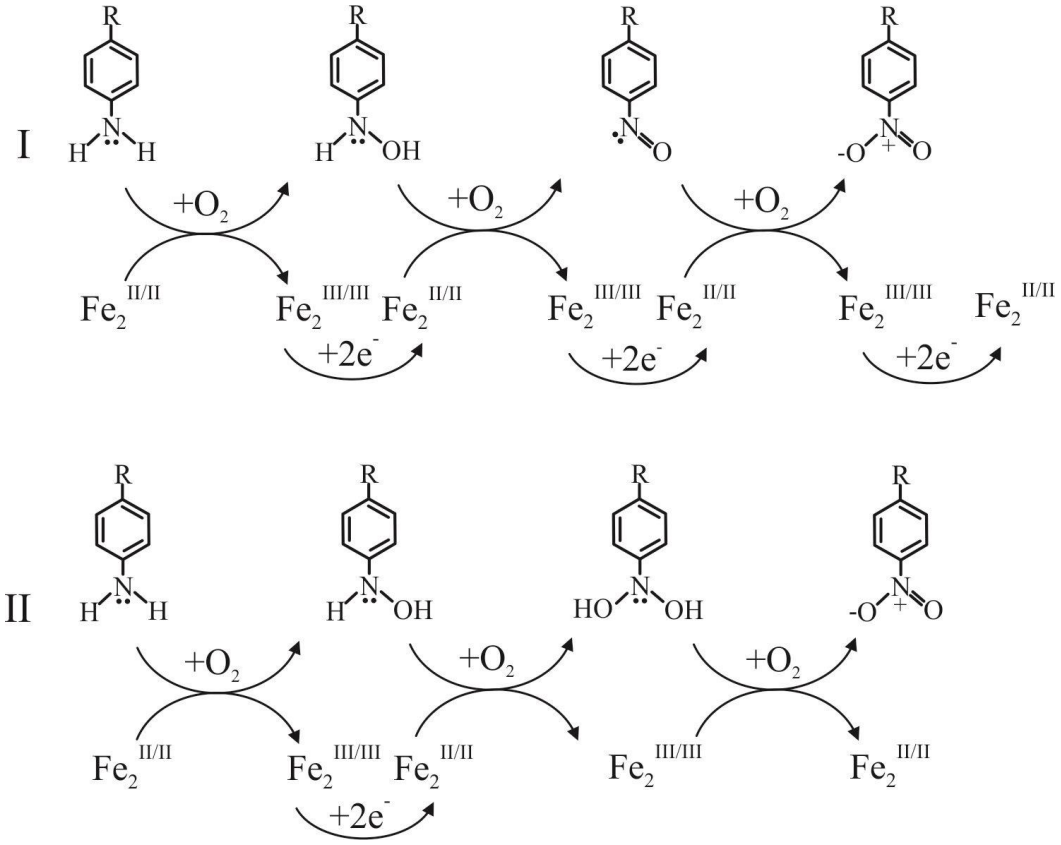

Figure 1-7: Two proposed mechanisms for the six-electron oxidation of an aryl-amine substrate to an aryl-nitro product, mediated by a diiron-cluster-containing oxygenase. Adapted from ref.[85]

Elucidating the mechanism of N-oxygenation by CmlI provides the opportunity to answers all of these questions, and in additional insight into the complex regulatory mechanisms utilized by this enzyme. On a surface level, CmlI is an additional data point that allows us to determine if substrate-based reduction is anomalous or a characteristic of the class. In addition, the long half-life of $CmlI^{P}$ makes possible many experimental procedures and investigations that would not be available with a shorter lived intermediate, such as that in AurF, and provide deep

mechanistic insight. For example, it has allowed the first steps of the cycle to be performed under one isotope of O_2, followed by an exchange of the atmosphere to complete the cycle with a different type of O_2. In this way, the source of each O_2 atom incorporated into the product can be tracked separately. These results are reported in Chapter 3. It has allowed spectroscopic investigation of this species in solution, as seen in the resonance Raman characterization in Chapter 2. It has also allowed extensive stopped flow experiments in which the order of addition of the various substrates can be varied, as seen in Chapter 4.

Aim and Scope of the Thesis

CmlI is a new entry into the diiron cluster-containing oxygenase canon in both the transformation it performs and in the type of oxidant it uses to carry out its chemistry. Furthermore, the presence of a diiron oxygenase in a natural product biosynthesis pathway represents a new role in biology for this class of enzymes. The discovery and isolation of the enzyme CmlI has allowed for several avenues of research that can enhance our understanding of the chemistry and the biological role of diiron cluster-containing oxygenases.

The aim of this thesis is to take advantage of the unique oxidant $CmlI^{P}$ to study various aspects of N-oxygenase and diiron oxygenase chemistry, and to broaden the understanding of O_2 activation by iron containing enzymes. One aim was to answer the specific mechanistic questions left by the work on AurF, detailed in the previous section, with the goals of understanding biological N-oxygenation and multi-step oxidations performed by diiron enzymes. A second goal was to characterize the structure and reactivity of $CmlI^{P}$ with an eye towards expanding the understanding of the role of diiron peroxo intermediates in diiron oxygenase chemistry.

This thesis begins in Chapter 2 by characterization of the active oxidant $CmlI^{P}$ as well as the diferric and diferrous forms of the enzyme, and of the reactivity of the CmlI enzyme towards native and non-native aryl-amine substrates. Chapter 3 undertakes a detailed mechanistic study built on spectroscopic characterization of enzyme and substrate based intermediates along the six electron oxidation pathway, and proposes a new and highly efficient mechanism for this six electron transformation. Chapter 4 expands the mechanistic study with kinetic analysis of each section of the CmlI single turn-over cycle, demonstrates the importance of substrate binding order on the enzyme function, and proposes a kinetic model that supports and expands on the mechanism proposed in Chapter 3. Chapter 5 provides detailed methods for all of the experiments performed in the previous chapters, including biological, analytical, and spectroscopic methods.

Chapter 2

Reactivity and Characterization of CmlI Peroxo Intermediate, the Active Oxidant in the Catalytic Cycle of CmlI

Portions of this chapter are reprinted and adapted with permission from: Thomas M. Makris, Van V. Vu, Katlyn K. Meier, Anna J. Komor, Brent S. Rivard, Eckard Münck, Lawrence Que, Jr., and John D. Lipscomb. "An Unusual Peroxo Intermediate of the Arylamine Oxygenase of the Chloramphenicol Biosynthetic Pathway" *J. Am. Chem. Soc.*, **2015**, *137*, 1608-1617.

Introduction

Carboxylate-bridged diiron cluster-containing monooxygenases catalyze an extraordinary array of chemical reactions, including the oxidation of aliphatic C–H bonds for carbon utilization,[87] antibiotic biosynthesis,[78, 88] the maturation of proteins involved in cell proliferation,[89] and the post-translational modification of tRNA,[17] among many others. Studies of oxygen activation in diiron hydroxylase enzymes and functional mimics have revealed that the most common mechanism for dioxygen activation in this class of enzymes involves the initial binding of O_2 to the reduced diferrous cluster, resulting in the formation of a peroxodiferric metal-oxygen adduct.[90-92] Subsequent to formation of this initial complex, the reactivities of diiron oxygenases diverge. In some cases, the peroxo intermediate is thought to directly participate in the oxidation of weak C–H bonds; [93] in others, it is known to undergo O–O bond cleavage to form a high-valent metal-oxo adduct that can transfer oxygen to inert hydrocarbons.[94-96] The peroxo intermediate is also the precursor of species involved in radical formation in ribonucleotide reductase (RNR),[97-98] and thought to be involved in desaturation reactions by fatty acid desaturases.[99] Therefore, studies of the electronic structures and reactivities of diiron peroxo intermediates are of central importance in understanding catalysis by a large number of diverse biological systems.

The reactive nature of diferric-peroxo intermediates often prohibits accumulation to concentration levels that permit structural interrogation. As a result, a thorough spectroscopic and structural study that can successfully address the O_2 coordination mode has been limited to a handful of diiron enzymes in which the Fe_2O_2 unit is unusually long-lived. In each of these cases, including the D84E/W48F mutant of RNR,[40, 92, 100] fatty acid Δ^9 desaturase (Δ^9D),[99, 101] and deoxyhypusine hydroxylase (hDOHH), [89] dioxygen has been shown to bridge the two iron atoms in a μ-η^1:η^1 coordination mode. Accordingly, the optical spectrum of the peroxodiferric intermediate in these enzymes has been shown to exhibit an intense ($\varepsilon > 1000$ $M^{-1}cm^{-1}$) charge transfer band with λ_{max} between 600 and 700 nm, similar to intermediates observed in transient kinetic studies of methane monooxygenase[102] and biomimetic model complexes. [54, 56-57, 103-104]

Despite the uniformity of the dioxygen binding mode observed for the spectroscopically characterized peroxodiferric intermediates, the possibility of alternative coordination geometries has been raised based on the distinct spectroscopic properties, primarily optical and Mössbauer, observed in transient intermediates of toluene/o-xylene monooxygenase (ToMO),[38, 105] para-aminobenzoate N-oxygenase (AurF), [53, 85] aldehyde deformylating oxygenase (ADO)[46] and the ribonucleotide reductase variant W48A/Y122F.[106] In contrast to the canonical μ-η^1:η^1 peroxo

intermediates, these diferric intermediates do not exhibit the optical signature band at ~700 nm, and instead show either no apparent optical absorption (e. g. ToMO), or a weaker ($\varepsilon \leq 500$ M^{-1} cm^{-1}) feature at shorter wavelength (450-500 nm; e.g. ADO, AurF, and RNR W48A/Y122F). Mössbauer spectroscopy similarly suggests that the O_2 binding mode of these species may indeed deviate from μ-η^1:η^1 coordination, as suggested by a significant decrease in quadrupole splitting ($\Delta E_Q \leq 0.7$ mm/sec) when compared to corresponding values ($\Delta E_Q > 1$ mm/sec) in peroxo intermediates that display the 700 nm band. Despite the marked discrepancy of the spectroscopic features of these peroxo intermediates versus those of the structurally characterized μ-η^1:η^1 peroxodiferric complexes, the direct demonstration of an alternative peroxo ligand geometry has not been obtained in any dinuclear iron enzyme. In contrast, a variety of alternative binding modes, including the μ-η^2:η^2 or μ-η^1:η^2, have been observed in dicopper cluster-containing enzymes and heteronuclear heme iron:copper model complexes, suggesting that they may also be found in diiron cluster-containing systems.[89, 92, 99, 107-116]

Arylamine oxygenases are a recently characterized class of diiron oxygenases involved in the biosynthesis of a nitroaryl moiety in a number of antibiotic pathways, including aureothin [18, 75] and chloramphenicol. [19, 117] This enzyme family, exemplified by AurF from the aureothin biosynthetic pathway, has been shown to catalyze nitro group formation through the six-electron oxidation of an amine precursor. This process may involve intermediary hydroxylamino-, dihydroxylamino-, and nitroso-oxidation products, although only the hydroxylamino derivative has been shown to be metabolized when used as an initial substrate in the case of AurF.[75, 85] Studies have now firmly established that AurF utilizes a diferrous cofactor to activate O_2 in a manner reminiscent of the bacterial multicomponent monooxygenase (BMM) superfamily. [53, 78] The diiron active-site of AurF is structurally similar to those of the BMMs, including that of methane monooxygenase (MMO). [118-119] The most notable deviation in the primary ligation environment is the presence of an additional histidine ligand in AurF, which substitutes for a water ligand in MMO and other members of the superfamily.

Recent studies of AurF by Bollinger, Krebs and colleagues have shown that the O_2 activation mechanism of arylamine oxygenases may permit an unprecedented opportunity to structurally characterize a diiron-peroxo intermediate with a unique O_2 coordination geometry. [53, 85] Exposure of reduced AurF to dioxygen resulted in the accumulation of a diferric intermediate with substantial kinetic stability, enabling its spectroscopic characterization by stopped-flow and rapid-freeze-quench techniques. While these approaches did not allow the structural details of the

AurF peroxo unit to be fully elucidated, the observed optical and Mössbauer spectroscopic properties of the presumptive oxygen-bound intermediate suggest that the coordination geometry may significantly differ from the commonly observed μ-η^1:η^1 mode.

CmlI is an arylamine oxygenase from the nonribosomal peptide synthetase (NRPS)-based chloramphenicol biosynthetic pathway of *Streptomyces venezuelae*.[19, 120] It has a high sequence identity (37%) to AurF, and thus it was proposed to contain a diiron cluster. Accordingly, sequence alignments suggest that the diiron clusters of CmlI and AurF have conserved ligand structures. CmlI and a β-hydroxylase, CmlA, from the same pathway were recently recognized as the first diiron cluster-containing oxygenases to function in an NRPS pathway.[88] CmlI and CmlA serve to tailor the developing antibiotic by adding or converting functional groups. Conversion of the arylamine to the nitroaryl group by CmlI is essential for the biocidal activity of chloramphenicol.[121] The similar amino acid sequences and catalyzed reactions of CmlI and AurF suggest that they may be able to form similar reactive intermediates. [19] Here, we show definitively that CmlI contains a diiron cluster and forms a hyperstable peroxo intermediate that can be spectroscopically characterized in solution as well as in frozen media. Using a combination of UV/Vis, Mössbauer, and resonance Raman spectroscopies, we demonstrate that the diiron arylamine oxygenase generates a peroxodiferric intermediate with a geometry that has not been previously described in the nonheme iron family. Moreover, transient kinetic absorption studies and product identification studies suggest that the unique peroxo intermediate is the reactive species in the oxygenation of arylamine substrates. These studies directly demonstrate the role of CmlI in chloramphenicol biosynthesis.

Results

Cloning, Overexpression, and Metal Center of CmlI. The arylamine oxygenase, CmlI, catalyzes the reaction shown in the inset of Figure 2-1 to yield chloramphenicol. The enzyme was cloned from *S. venezuelae* genomic DNA of the chloramphenicol biosynthesis cluster, overexpressed in *E. coli*, and purified to homogeneity. The enzyme as isolated from M9 minimal media with exogenously added iron contained 2.1 ± 0.1 irons per monomer. The optical spectrum showed an intense chromophore at 375 nm (ε = 2700 M^{-1} cm^{-1}) (Figure 2-1, black trace). Anaerobic reduction of the metal center with sodium dithionite required two reducing equivalents and resulted in a weak, featureless spectrum in the visible (Figure 2-1, blue trace). The resting

and fully reduced forms of the enzyme are EPR silent at X band. However, the partially reduced enzyme exhibits a pH-dependent EPR spectrum (Figure 2-2), with the principal *g*-values below *g* = 2, a characteristic feature of an *S* = ½ ground state species from an antiferromagnetically coupled $Fe^{III}Fe^{II}$ cluster. The metal quantification and the spectral characteristics of the oxidized enzyme are consistent with a dinuclear iron cluster in which the irons are bridged by an oxo ligand (see for example [88]).

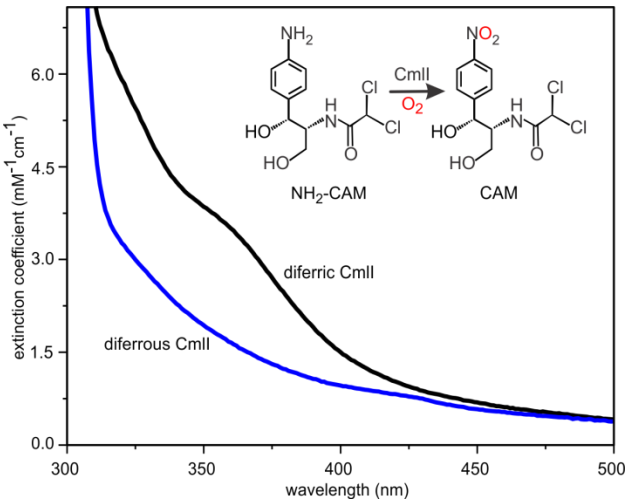

Figure 2-1: Optical absorption spectrum of resting CmlI (black trace), and dithionite reduced CmlI (blue trace). Buffer: 50 mM Bicine at pH 9.0, 25 °C. *Inset*: Reaction catalyzed by CmlI. At least one and probably both oxygens in the nitro group derive from O_2. The reaction is a net 6 electron oxidation of the amine function, but the stoichiometries of O_2 utilization and electrons required during the reaction to activate O_2 are controversial.

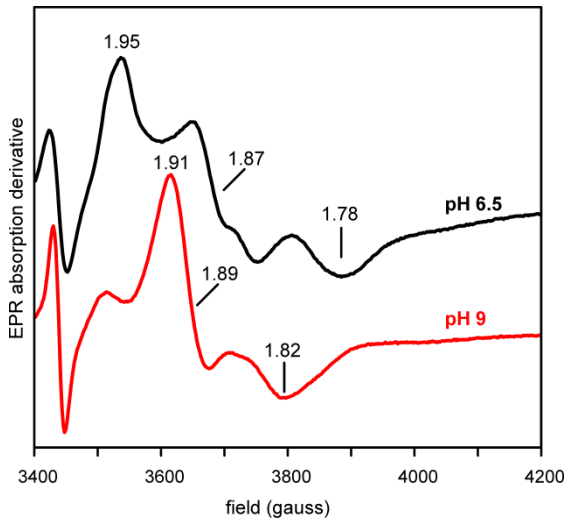

Figure 2-2: EPR spectra of mixed valent CmlI. Mixed valent CmlI produced by photoreduction at pH 6.5 (top, black) and pH 9.0 (bottom, red), recorded at 15 K (black) and 45 K, respectively, at a microwave power of 10 mW.

Mössbauer Characterization of CmlI. Mössbauer spectra of CmlI at pH 6.5, 7.5 and 9.0 (Figure 2-3 and Figure 2-4) indicate that the protein contains a diiron center, in accord with the expectations based on the sequence similarities between CmlI and AurF. The spectra of diferric CmlI ($CmlI^{ox}$) depend sensitively on the pH in ways we do not yet understand; the pH dependence is more complicated than that of a simple interconversion between two forms of the diiron cluster. The studies reported here focus on reduced CmlI ($CmlI^{red}$) and a reaction cycle intermediate at pH 9.0 in Bicine buffer, and so the following spectral analysis pertains to the enzyme under those conditions.

The 4.2 K Mössbauer spectra of as-isolated and dithionite reduced CmlI are shown in Figure 2-3, Figure 2-4, and Figure 2-5. A summary of all fitting parameters is given in Table 2-1. The spectrum of as-isolated $CmlI^{ox}$ at pH 9.0 (Figure 2-3A) is best described as a superposition of four quadrupole doublets, each having an isomer shift of $\delta \sim 0.50$ - 0.55 mm/sec that is characteristic of high-spin Fe^{III}. The observation of quadrupole doublets at 4.2 K (rather than spectra exhibiting paramagnetic hyperfine structure as typically observed for *mononuclear* Fe^{III} complexes) suggests exchange coupled pairs of iron atoms, in accord with the observations reported for numerous diiron proteins. The black line in Figure 2-3A represents the sum of the four doublets. The red line shows the sum of the nested doublets 1 and 4, while the blue line represents the sum of the (unresolved) doublets 2 and 3. The decomposition of the spectrum into

four doublets is supported by the Fourier transform treated spectrum shown in Figure 2-4. Such treatments [122-124] increase the resolution of the spectrum by removing the line width contribution of the ^{57}Co radiation source, a procedure that sharpens the absorption lines by roughly a factor two. In Figure 2-4 the presence of three doublets is quite apparent, and it is also apparent that one of the three doublets is broader and more intense and thus must be composed of two similar subspecies. The observation of four doublets shows that the oxidized enzyme can stabilize at least two cluster forms in which the two irons of each cluster type reside in different environments. The 4.2 K Mössbauer spectra obtained at pH 6.5 and 7.5 are not related to that of the pH 9.0 form by a simple redistribution of the intensities of doublet pairs. Following the doublet pattern to lower pH did not yield the desired pairings, as ΔE_Q changes were observed that affect a single site in a cluster (as might be expected for a carboxylate changing from monodentate to bidentate coordination, or protonation of a monodentate carboxylate) as well as changes affecting both iron sites of a cluster (such as a change involving a bridging ligand).

In Table 2-1 the doublets are enumerated in order of descending quadrupole splittings, ΔE_Q. There is no ambiguity in the assignment of the lines of doublets 1 and 4, as combining lines assigned to these doublets with those of doublets 2 and 3 would yield unreasonable pairs of δ values. Observation of iron clusters with similar isomer shifts but different quadrupole splitting suggests that while the two irons belong to the same cluster, they experience different local environments. In contrast to the pairing of doublets 1 and 4, combining the four lines of the similar doublets 2 and 3 into a non-nested pair would yield two doublets with parameters similar to doublets 2 and 3. Presently, we do not see an obvious way of combining the four doublets uniquely into two cluster types. Cluster form 1, comprising doublets 1 and 4, represents ca. 44% of the Fe in the sample, whereas cluster form 2 accounts for 56%. Interestingly, the pH 7.5 spectrum of CmlI resembles the pH 7.5 spectrum of AurF reported by Krebs and coworkers (overlay shown in Figure 2-5). [53]

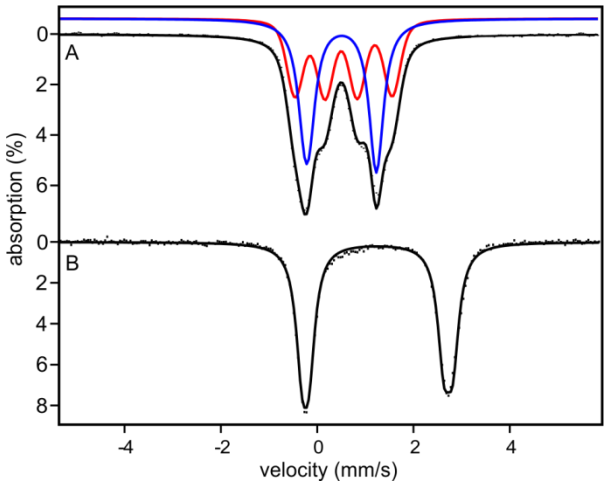

Figure 2-3: 4.2K Mössbauer spectra of (A) as-isolated CmlI and (B) dithionite reduced CmlI. Spectra were obtained in the absence of an applied magnetic field (B = 0). Samples were prepared in Bicine buffer at pH 9.0. Solid black line in (A) is a spectral simulation assuming four quadrupole doublets of essentially equal intensity; parameters are listed in Table 1. The red line shows subspectra of nested doublets 1 and 4, while the blue line represents the superposition of the (similar) doublets 2 and 3. The sum of the red and blue lines yields the black curve. (B) The solid black line drawn through the experimental data of diferrous CmlI is a spectral simulation for two similar doublets using the parameters listed in Table 2-1.

Figure 2-3B shows a zero-field Mössbauer spectrum of dithionite-reduced CmlI. The spectrum consists of a doublet with parameters typical of high-spin Fe^{II}. Spectral simulations indicate that the spectrum is a superposition of two overlapping doublets with $\Delta E_Q(1) = 3.13$ mm/s, $\delta(1) = 1.25$ mm/s and $\Delta E_Q(2) = 2.80$ mm/s, $\delta(2) = 1.23$ mm/s, parameters quite similar to the $\Delta E_Q = 3.06$ mm/s, $\delta(2) = 1.24$ mm/s reported for diferrous AurF.[53] Our simulations require a Lorentzian line width of 0.30 mm/s full width at half maximum (attempts to simulate the spectrum with one doublet while using different widths for the high-and low-energy features did not produce good matches in the wings of the high-energy line). The above choice of parameters results when the nested combination of the two doublets is chosen; the non-nested combination would yield the less plausible parameter set with $\delta(1) = 1.16$ mm/s $\delta(2) = 1.33$ mm/s. In contrast to the diferric state, only one cluster form, with two slightly inequivalent sites, seems to be present in the diferrous state. The presence of only one cluster form in the reduced state of the protein, rather than two as observed in the oxidized state, would not be surprising as diiron clusters generally experience considerable ligand changes and rearrangements upon reduction, such as loss of an oxo bridge and carboxylate shifts.[125-128]

Table 2-1. Quadrupole Splittings and Isomer Shifts for as-Purified (CmlI^{ox}), Dithionite-Reduced (CmlI^{red}), and Oxygenated Forms of CmlI.

			δ (mm/sec)	ΔE_Q (mm/sec)	Area (%)
CmlI^{ox}	Cluster Form 1[a]	Doublet 1	0.55	2.02	~44
		Doublet 4	0.50	0.64	
	Cluster Form 2[a]	Doublet 2	0.50	1.48	~56
		Doublet 3	0.52	1.40	
CmlI^{red}		Site 1	1.25	3.13	50
		Site 2	1.23	2.80	50
Oxygenated		Site a	0.62	-0.23[b]	50[c]
		Site b	0.54	-0.68[b]	50[c]

[a] We have assigned doublets 1 and 4, somewhat arbitrarily, to one cluster form and doublets 2 and 3 to a second cluster form. Given the uncertainties in line shapes, which affect the percentages, other pair combinations are possible.
[b] Signs of ΔE_Q were determined from 4.2 K spectrum taken at B = 75 kG.
[c] Represents spectral contribution after removing 22% of oxidized pH 9 CmlI from the spectrum.

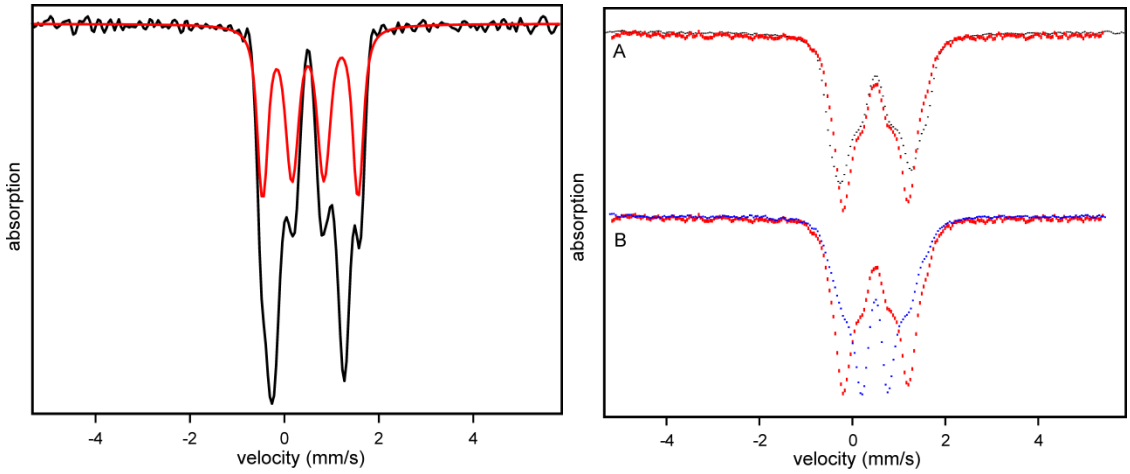

Figure 2-4: Mössbauer spectra of CmlI. Left: Fourier Transform treated Mössbauer spectrum of diferric CmlI at pH 9.0. A Mössbauer spectrum is the convolution of the spectrum of the absorber with the spectrum emitted by the 57Co Mössbauer source. In the Fourier transform treatment, the experimental spectrum is transformed into the time-domain. The known source contribution to the linewidth is then removed in the time domain. The figure shows the back-transformed spectrum. The red line indicates the nested doublets 1 and 4. Doublets 2 and 3 contribute to the most intense peaks. Figure S3: Comparison of the 4.2 K Mössbauer spectra of diferric CmlI prepared at different pH values. (A): Spectra recorded at pH 9 (black) and pH 7.5 (red). (B): pH 7.5 spectrum (red) is shown together with the pH 6.5 spectrum (blue).

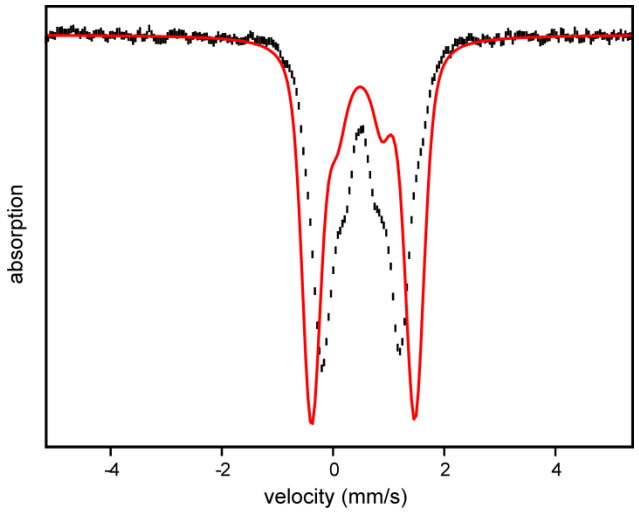

Figure 2-5: Comparison of the pH 7.5 Mössbauer spectra of CmlI (black) and AurF (red). The AurF spectrum is our simulation based on inspection of Figure S1 of Li et al.[85]

A Long-Lived Intermediate is Formed Upon Exposure of Reduced CmlI to Dioxygen. The addition of excess dioxygen to the dithionite-reduced, anaerobic enzyme results in the appearance of a broad new optical absorption band at approximately 500 nm ($\varepsilon \approx 500\ M^{-1}\ cm^{-1}$ per diiron cluster) (Figure 2-6, red trace). The spectrum of this species is similar to that reported for the proposed peroxo intermediate of AurF.[53] Extended incubation of this likely CmlI-peroxo species (this assignment is made directly below) leads to the slow restoration of a spectrum indistinguishable from that of the resting diferric enzyme. The stability of the 500 nm absorbing species was determined in transient kinetic experiments over a range of temperatures. The time course for its decay could be fit by a single exponential expression at all temperatures examined (Figure 2-8A). The oxygenated form of CmlI demonstrates extraordinary stability, with measured half-lives of 20 minutes and 3 hours at 25 °C and 4 °C, respectively. The stability of this intermediate in CmlI is substantially greater than that of the similar intermediate observed for AurF, ($t_{1/2} \approx 7$ min at 20 °C),[53] which facilitates studies of its reactivity and structure.

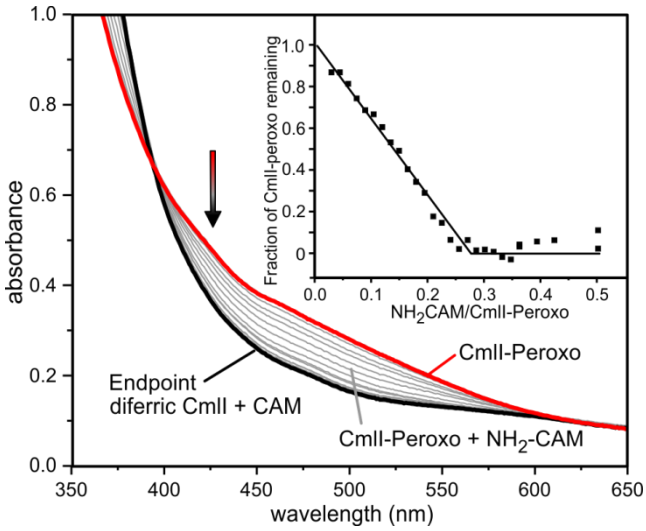

Figure 2-6: Reaction of CmlI-Peroxo with NH_2-CAM. CmlI-Peroxo (red trace) was formed by exposure of stoichiometrically reduced diferrous CmlI to O_2. Aliquots of NH_2-CAM (~0.05 equivalents) were added and the spectrum scanned (gray traces, only selected traces are shown for clarity). At the end of the titration, the spectrum of the resting diferric enzyme is restored (black trace). Buffer: 50 mM Bicine, pH 9, 4 °C. Inset: Fraction of CmlI-Peroxo remaining at each point during the titration plotted as a function of NH2-CAM equivalents added.

Reactivity of the CmlI-Peroxo Intermediate. Addition of the chloramphenicol precursor D-threo-1-(4-aminophenyl)-2-dichloroacetylamino-1,3-propanediol (NH_2-CAM) to the CmlI-peroxo (**P**) species resulted in a rapid loss of the optical features of the intermediate (Figure 2-8B). The acceleration of the decay of the intermediate, at 4 °C, is approximately 100,000-fold when using 1 mM NH_2-CAM. Titration of **P** species with aliquots of NH_2-CAM resulted in the restoration of the spectrum of the resting enzyme (Figure 2-6, gray traces leading to the black trace). Extraction of the reaction solution and analysis by HPLC and extracted ion mass spec showed that the product of the reaction is chloramphenicol (Figure 2-7). Chloramphenicol was also shown to be the product from this substrate in previous continuous turnover reactions of CmlI. [19] A plot of the disappearance of P vs. the NH_2-CAM equivalents added (Figure 2-6, *inset*) shows that approximately 3 **P** complexes are consumed for each NH_2-CAM consumed, although titrations show a range of stoichiometries from 2-5 **P** species per NH_2-CAM consumed. A similar stoichiometry was reported for the conversion *para*-aminobenzoate (pABA) to p-nitrobenzoate (pNB) by AurF, although a later study cast doubt on this stoichiometry.[53, 85]

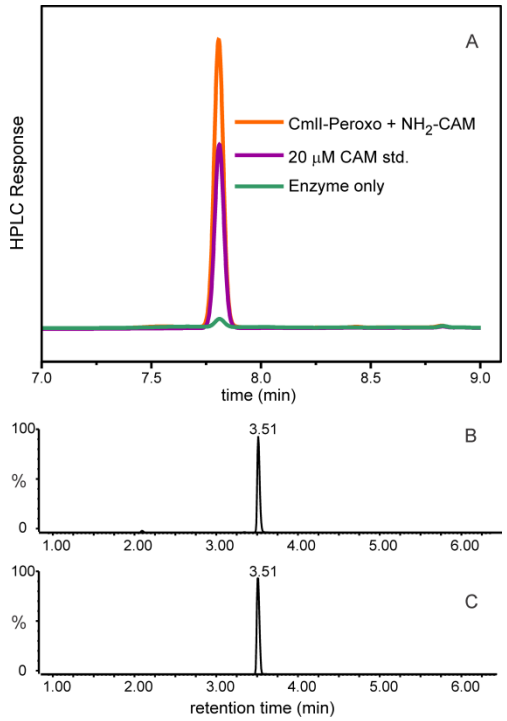

Figure 2-7: Product from the reaction of 1 mM CmlI-peroxo with 10 mM NH_2-CAM. Top: (A) HPLC traces of the extracted reaction mixture at the end of the titration in comparison to an authentic chloramphenicol standard. Bottom: Extracted ion chromatograms at m/z = 321 for the reaction product (B) and a chloramphenicol standard (C). Buffer: 50 mM Bicine, pH 9.0.

CmlI-Peroxo Appears to React Directly with Substrates. The exceptionally long lifetime of the **P** allows the formation of the intermediate before transfer to a stopped-flow syringe, so that the reaction with NH_2-CAM and a variety of adventitious substrates can be easily observed (Figure 2-8B, C). The decay time course is fit well by a single exponential for each substrate, consistent with a single-step reaction or a rate-limiting reaction followed by much more rapid reactions to form product. The reciprocal relaxation time (RRT) for the decay of the CmlI-peroxo depends on both the concentration and type of substrate provided as shown in Figure 2-8C. It is interesting that the plot of the RRT versus the substrate concentration is linear extrapolating to zero for each substrate when the substrates are supplied in large excess. This suggests that the reaction is irreversible, and thus, the observed RRT is the pseudo first-order rate constant for the reaction. The linear dependence of the pseudo first-order rate constant is surprising, as it implies that the reaction of **P** with amine substrates occurs as a second order process without formation of a kinetically significant enzyme-substrate complex. To our knowledge, the only diiron enzyme intermediate that behaves kinetically in this way is the MMO bis-μ-oxo $Fe^{IV}Fe^{IV}$ intermediate Compound Q.[94] However, slow, soluble alternative substrates for Compound Q reactions showed

hyperbolic substrate concentration dependence, suggesting that a high K_m complex is, in fact, formed.[129] In the case of CmlI, no deviation from linearity was observed at concentrations up to 50 mM for the most soluble substrates tested (Figure 2-9). Apparent second order rate constants for **P** reaction with arylamine substrates are shown in Figure 2-8C, *inset*. Interestingly, the chloramphenicol precursor L-para amino phenylalanine (L-pAPA), is not a substrate when bound to the NRPS for the system, CmlP, truncated to the adenylation and thiolation domains.

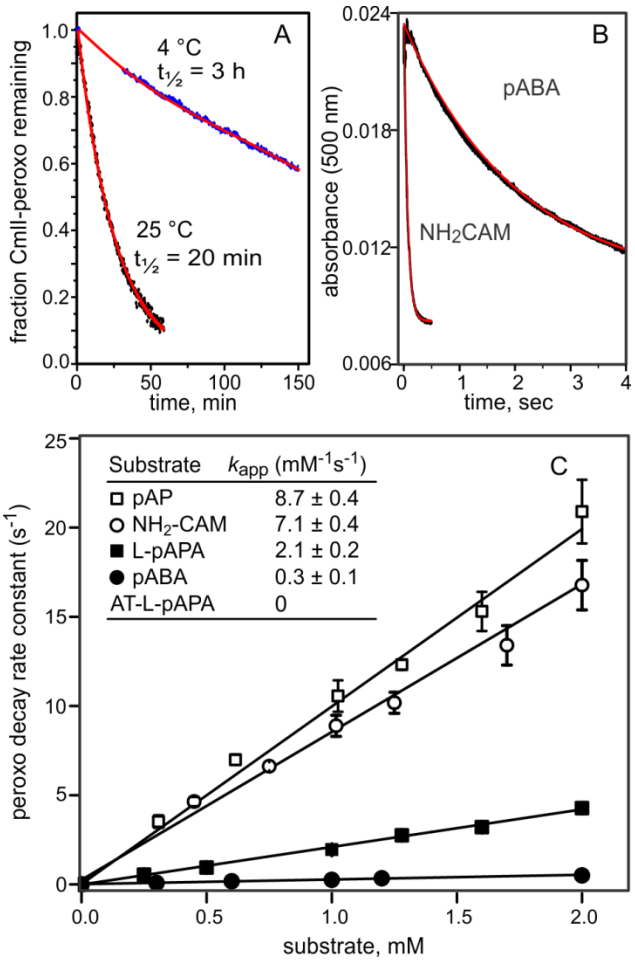

Figure 2-8: Single turnover reaction of CmlI-Peroxo with aryl-amine substrates. A: Autodecay time course (filled ovals) for reaction of 600 μM pre-formed CmlI-peroxo at 4 or 25 °C. A single exponential fit (red) is shown superimposed on the data. B: Single turnover time course for reaction of 50 μM pre-formed CmlI-peroxo with 1 mM of the substrate shown (black). A single-exponential fit (red) is shown superimposed on the data. C: Plot of the apparent first order CmlI-peroxo decay rate constant for the reaction of 50 μM diferrous CmlI with 850 μM O_2 and the concentration of the substrate shown (all concentrations after mixing). Inset: Apparent second order rate constants calculated from the slopes of the plots in the main figure. Buffer: 50 mM Bicine at pH 9.0, 4 °C except where noted.

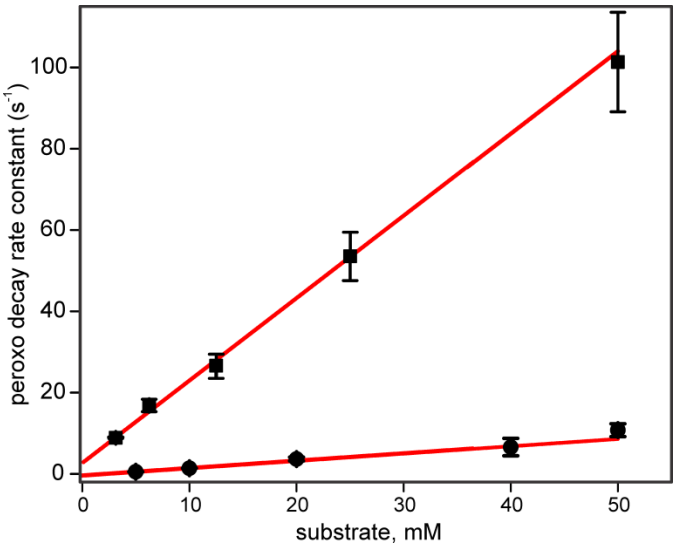

Figure 2-9: Linear dependence of CmlI-Peroxo decay rate. Reaction with L-pAPA (squares) and pABA (circles). In these experiments, the CmlI-Peroxo was pre-formed and loaded into a stopped flow syringe. The substrates were mixed in large excess over the enzyme from the second syringe. This method results in a single observed exponential kinetic phase which can be fit with nonlinear regression to give the observed rate constants.

Only Reaction with Native Substrate NH_2-CAM Yields the Complete Six-Electron Oxidation Product. P is shown to react with a variety of para-amino moiety containing substrates, including the native substrate NH_2-CAM, *p*-aminophenol, *p*-aminobenzoate, *p*-aminophenylalanine, and *p*-nitroaniline (Figure 2-8). However, analysis of reaction products by HPLC revealed that only the reaction with NH_2-CAM results in a significant amount of the full six-electron oxidized product with a nitro moiety (Table 2-2). The reaction with *p*-aminophenylalanine yields a small amount of *p*-nitrophenylalanine. The other substrates results in the two- or four-electron oxidized species, the hydroxylamine and nitroso derivatives, respectively. This finding suggests that the chloroacetyl, the hydroxyl, and/or the methyl hydroxyl groups play an essential protein binding role to ensure full oxidation.

Table 2-2: Products of the reaction of CmlI-P with aryl-amino substrates.

Substrate	Product(s)
NH_2-CAM 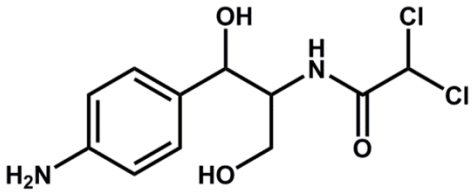	- NO_2 - NO
pAP 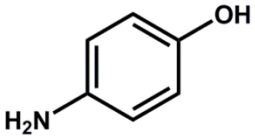	- NO
pABA 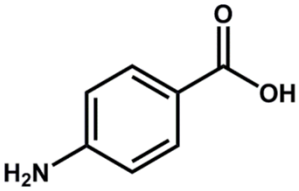	- NO - NHOH
L-pAPA 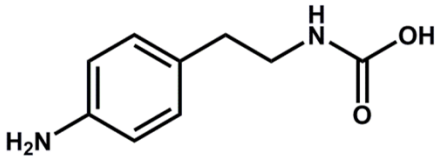	- NO_2 - NO
pNA 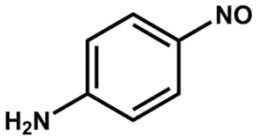	- NO

Characterization of the Oxygenated Intermediate by Mössbauer Spectroscopy. The exceptional stability of the oxygenated CmlI intermediate enables its spectroscopic interrogation at enzyme and O_2 concentrations that surpass those normally obtained in rapid mixing experiments, as the intermediate can be prepared quite simply through the gradual addition of gaseous O_2 to the reduced enzyme at 4 °C. A 2 mM solution of dithionite-reduced CmlI, at pH 9.0, was gently oxygenated with a stream of O_2 gas at 4 °C for 10 minutes and subsequently frozen in liquid nitrogen.

As shown in Figure 2-10A, the 4.2 K zero-field Mössbauer spectrum of this sample is quite different from those of the resting and dithionite-reduced enzyme. The majority component, assigned to **P**, comprises two nested doublets of equal intensity that account ca. 80% of the iron in the sample. Doublet *a* (simulated blue curve) has ΔE_Q (*a*) = -0.23(1) mm/s, δ (a) = 0.62(1) mm/s, while doublet *b* (green line) has ΔE_Q (*b*) = -0.68(2) mm/s, δ (*b*) = 0.54(1) mm/s. The two doublets are superimposed on a minority species that contributes the shoulders at + 1.5 mm/s and -0.5 mm/s Doppler velocity. This spectral component seems to comprise the four doublets observed for the diferric pH 9.0 CmlI, and it accounts for ≈20% of the iron in the sample. Given the observed rate constant of ≈0.005 min^{-1} for the decay of the **P**, at 4 °C, about 10% diferric CmlI is expected at the time the sample was frozen. The remainder, if any, probably derives from incomplete reduction. Subtracting the diferric species (indicated by the red line) results in the removal of the shoulders and yields two doublets *a* and *b*.

The ΔE_Q and δ parameters listed in Table 2-3 were obtained by assigning the four lines to two *nested* doublets; the non-nested choice would yield ΔE_Q(*a*') = -0.37 mm/s, δ (a') = 0.69 mm/s and ΔE_Q (*b'*) = -0.54 mm/s, δ (*b'*) = 0.46 mm/s, a combination with less plausible δ values in our opinion. Krebs and coworkers have observed a very similar species for AurF-peroxo (see Table 2-3, Figure 2-2, and caption of [85]). It is worth noting that the two doublets of $Fe^{III}Fe^{III}$ CmlI-peroxo (and AurF-peroxo) have quite different δ values, a situation similar to that reported by Chavez et al. for the intermediate obtained by exposing the diiron(II) "paddlewheel" complexes of sterically hindered $ArCO_2^-$ ligands to O_2. [130] We address this observation below.

The $Fe^{III}Fe^{III}$ CmlI-peroxo complex exhibits quadrupole doublets at 4.2 K, which suggests an exchange coupled, high-spin diferric system for which the local spins $S_1 = S_2 = 5/2$ are antiferromagnetically aligned. The 7.5 T spectrum of Figure 2-10B can be simulated under the assumption that the ^{57}Fe nuclei experience only the applied field, i.e. the ground state of $Fe^{III}Fe^{III}$ **P** has a cluster spin $S = 0$. By recording applied field Mössbauer spectra between 20 K and 100 K one can often measure the exchange coupling constant *J*. This technique works well for $J \leq 120$ cm^{-1} provided the electronic spin relaxes either fast or slow compared to the nuclear precession frequencies. At intermediate relaxation rates, however, the spectra are broad, and an analysis of such spectra, to our knowledge, has not yet been reported for a diferric system. Unfortunately, this situation applies to the $Fe^{III}Fe^{III}$ peroxo species of CmlI. The exchange Hamiltonian $\mathcal{H} = J S_1 \bullet S_2$ produces a spin ladder $S = 0, 1 ... 5$ for which the first excited state, the $S = 1$ multiplet, has energy *J*. For $J \leq 20$ cm^{-1} a field of 7.5 T would mix the $M_S = \pm 1$ sublevels of the $S = 1$ multiplet

into the ground state, and this mixing would readily be detected in the 4.2 K spectrum. As there is no evidence for such mixing in the spectrum of Figure 5B, we conclude that $J_{peroxo} > 20$ cm^{-1}.

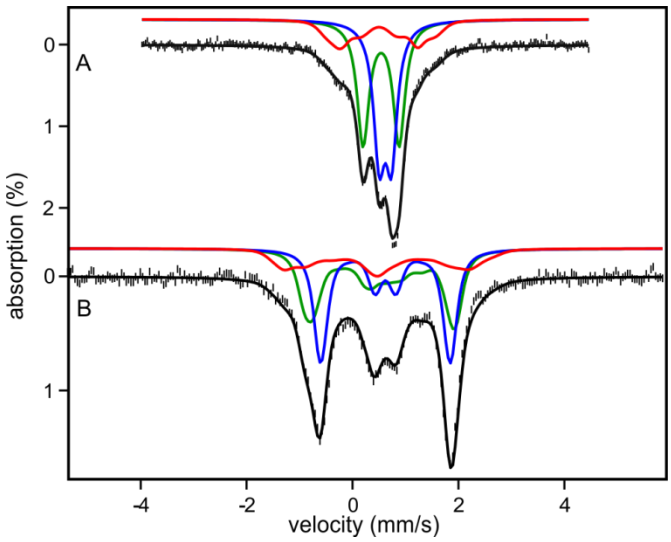

Figure 2-10: 4.2K Mössbauer spectra of oxygenated CmlI. (A) Zero field spectrum. The green and blue curves are spectral simulations for sites a and b of the major (>80%) peroxo species). The red curves outline the 20% contribution of a diferric contaminant, assumed to be the pH 9 species of Figure 2A. (B) Spectrum of the same sample recorded in a parallel applied field of 7.5 T. The blue and green lines are spectral simulations of the diiron(III) peroxo components. The remaining (red) simulated spectrum, accounting for roughly 20% of the experimental spectrum, was well approximated with δ and ΔEQ parameters of pH 9 as-isolated diferric CmlI.

Table 2-3: Spectroscopic parameters of peroxodiiron(III) intermediates observed in dinuclear iron enzymes.

O_2 Adducts of diiron(II) enzymes	λ_{max} (nm) ε (M^{-1} cm^{-1})	δ (mm/s)	ΔE_Q (mm/s)	J (cm^{-1})	ν(O-O) (cm^{-1}) $\Delta(^{16}O\text{-}^{18}O)$	Peroxo binding mode	Refs.
hDOHH	630 (1500)	0.55, 0.58[a]	1.16, 0.88	50-70	855 (44)	μ-OH-μ-η^1:η^1	89
MMOH	725 (1800)	0.69	1.55			μ-η^1:η^1	96, 124, 131
D84E R2	700 (1500)	0.63	1.58	50	868 (46)	μ-η^1:η^1	40, 92, 98, 100, 132
Frog M Ferritin	650 (1000)	0.62	1.08	70	851 (-51)	μ-η^1:η^1	109, 132-133
Stearoyl-ACP Δ^9 Desaturase	700 (1100)	0.68,0.64	1.90, 1.06		898 (-54)	μ-η^1:η^1	99, 101
ToMO	no visible band	0.55	0.67				38
W48A/Y122F R2	500 (1500)	0.52, 0.45	0.55, 1.53			-	106
ADO	450 (1200)	0.48, 0.49	0.55, 1.23			-	46
AurF	500 (500)	0.61, 0.55	0.35, 0.74[b]			-	53
CmlI	500 (500)	0.62, 0.54	-0.23, -0.68[b]	≥ 20	791 (43)	μ-η^1:η^2	This work

[a] Alternatively, the Mössbauer data can be assigned, less plausibly, as a non-nested pair of doublets with parameters δ = 0.49, 0.63 mm/s and ΔE_Q = 1.05, 0.99 mm/s

[b] Values for assumption of nested doublets; signs of ΔE_Q unknown.

Resonance Raman Spectroscopy of the CmlI Oxygenated Intermediate. Resonance Raman spectroscopy can be used to demonstrate the presence of a peroxo ligand bound to the diiron(III) site and provides a means to evaluate the cluster structure of the intermediate absorbing at 500 nm. Figure 2-11 shows the resonance Raman spectra obtained by 488 nm excitation of **P** samples prepared with different oxygen isotopes, as well as the spectrum of a sample in which the intermediate was allowed to decay. The spectrum of the $^{16}O_2$ adduct (trace A) exhibits a peak at 791 cm^{-1} that slowly decays over 7 hours at 0 °C (trace D), matching the observed kinetics at 500 nm described above. The spectrum of the $^{18}O_2$ adduct (97 % enrichment) (trace B) shows a downshift of the 791 cm^{-1} peak to 747 cm^{-1}. The observed 44 cm^{-1} downshift of the 791 cm^{-1} peak almost matches the value calculated by Hooke's law for a diatomic O-O oscillator (-45 cm^{-1}). A mixed-isotope labeling experiment (trace C) shows the appearance of a peak at 768 cm^{-1}, halfway between those of the $^{16}O_2$- and the $^{18}O_2$-derived samples, demonstrating a vibrational mode that must involve both atoms of the added O_2 and cannot arise from other possible band assignments such as ν(Fe=O) or ν_{asym}(Fe–O–Fe) modes, which involve only one oxygen atom. Taken together, these observations confirm that this ~800-cm^{-1} feature arises from a peroxo moiety. (No $^{18}O_2$-sensitive vibration was observed in the 500 cm^{-1} region where the ν(Fe-O) mode would typically be found.) A perusal of Table 2-3 shows that CmlI-peroxo exhibits a ν(O-O) feature that is at least 60 cm^{-1} lower in frequency than observed for any other enzyme peroxodiiron(III) intermediate reported to date. Taken together, the Mössbauer and resonance Raman results point to an as yet unobserved structure for a peroxo intermediate of a nonheme diiron enzyme.

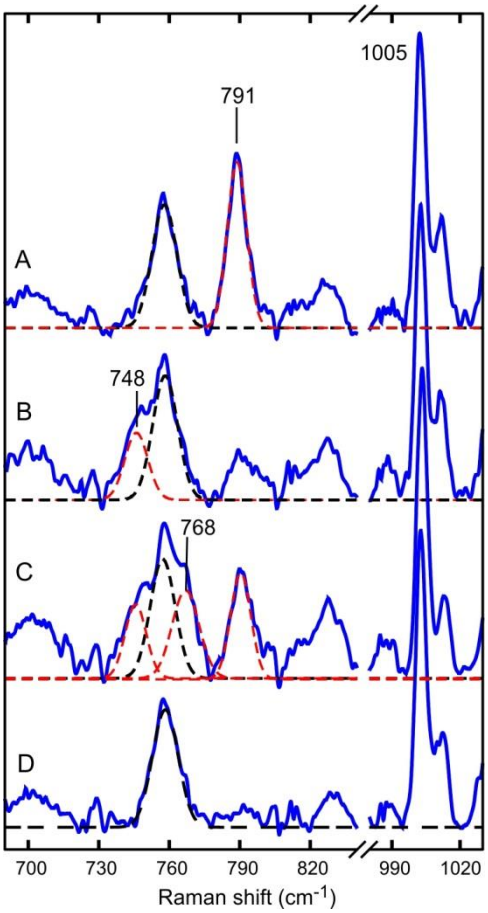

Figure 2-11: Resonance Raman spectra of oxygenated CmlI, pH 9.0. Prepared with: (A) $^{16}O_2$, (B) $^{18}O_2$, (C) mixed-labeled O_2, and (D) a sample after prolonged incubation. Spectra were obtained with 200 – 300 mW laser power and subjected to two-point baseline subtraction. No smoothing was required. Spectra were aligned and normalized using the sharp peak at 1005 cm^{-1} that arises from phenylalanine residues of the protein. Dashed lines represent Gaussian fits to the peaks of interest.

Discussion

Summary of Findings. It is shown here that **P** converts the arylamine precursor to chloramphenicol to the nitroaryl group of the active antibiotic. The metal center of CmlI is characterized as a diiron cluster that stabilizes an exceptionally long-lived peroxo intermediate. This intermediate appears to react directly with its substrate at physiologically relevant concentrations, suggesting that it is the reactive intermediate in the CmlI reaction cycle. It is noteworthy that **P** does not carry out the aliphatic or aromatic hydroxylations reactions reported for other diiron enzymes, and the latter enzymes do not carry out arylamine oxygenation. [21, 38, 53, 85, 91, 93-94] The factors affecting stability of the diiron-peroxo intermediates and their substrate

reactivity are largely unknown. Our kinetic and spectroscopic studies of **P** suggest that the unusual stability and substrate reactivity may result from formation of a previously uncharacterized peroxo structure. The bases for this conclusion are discussed here.

Nature of the CmlI-Peroxo Intermediate. The Mössbauer spectra of the diferric states of CmlI show that at least two cluster forms are present at each pH studied, and that each cluster form has inequivalent Fe^{III} sites to yield four quadrupole doublets. These various forms occur in different ratios depending on conditions such as pH; at pH 9 two cluster forms in an approximate 1:1 ratio are present. The pH 9 Mössbauer spectrum of *diferrous* CmlI exhibits two similar, but unresolved, quadrupole doublets with ΔE_Q = 3.13 and 2.80 mm/s. For the closely related diferrous form of AurF (measured at pH 7.5) one broad quadrupole doublet was observed, with a ΔE_Q (= 3.06 mm/s) that is in between the ΔE_Q values determined here. These observations seem to suggest that the reduced enzymes contain just one cluster form, with indistinguishable sites in AurF and slightly different sites in CmlI, although what is known about the diiron cluster structure (two His ligands bound to one iron and one to the other, see Figure 2-13) suggests that strict equivalence is ruled out.

In contrast, the peroxo adducts of both CmlI and AurF exhibit a Mössbauer spectrum containing two equally intense quadrupole doublets, suggesting the presence of one cluster type with inequivalent Fe^{III} sites. An interpretation that the two doublets represent two cluster forms, each with equivalent sites, seems contrived as each cluster would be required to have equivalent ferric sites that differ in isomer shift from those in the other cluster. As pointed out above, the CmlI-peroxo cluster contains two antiferromagnetically coupled Fe^{III} sites; analysis of the 7.5 T spectrum of Figure 2-10 shows that $J > 20$ cm^{-1} (in the $\mathcal{H}_{exch} = J\,\mathbf{S}_1 \bullet \mathbf{S}_2$ convention).

The unusually low ν(O-O) frequency associated with the **P** intermediate suggests a peroxo binding mode not yet recognized within the family of dioxygen activating diiron enzymes. The four other peroxo intermediates of diiron enzymes characterized thus far by resonance Raman spectroscopy (Table 2-3) exhibit ν(O-O) frequencies in the range of 851 – 898 cm^{-1} and have been assigned to have μ-η^1:η^1 binding modes. The ν(O-O) frequencies of these complexes are at least 60 cm^{-1} higher than the 791 cm^{-1} value for CmlI-peroxo. Indeed, most synthetic diiron(III)-peroxo complexes described to date have μ-η^1:η^1 binding modes and exhibit the higher frequencies as well (Table 2-4).[54, 56-57, 103-104, 110] The only potential exception to this generalization among diiron(III)-peroxo complexes is the O_2 adduct reported by Chavez et al.,[130]

which has a ν(O-O) frequency at 822 cm^{-1}. This synthetic adduct also has a diferric cluster with relatively weak antiferromagnetic coupling (J ~ 30 cm^{-1}) and exhibits two doublets with distinct isomer shift values that are similar to those found for CmlI-peroxo. Unfortunately, there is no structural information available for this adduct.

Lower ν(O-O) frequencies are more typically observed for mononuclear (η^2-peroxo)iron(III) complexes (812-827 cm^{-1}; see Table 3). Even lower ν(O-O) frequencies (746 - 813 cm^{-1}) are found for a small subset of heterodinuclear complexes that consist of an (η^2-peroxo)iron(III) center having a second metal ion bound to the peroxo ligand to give rise to either a μ-η^2:η^2- or a μ-η^1:η^2-peroxo bridge. The first examples of such complexes featured a Cu^{II} as the second metal ion,[134-135] so the decrease in ν(O-O) could be attributed to an effect of the redox-active Cu^{II}, as previously observed in Cu^{II}_2(μ-η^2:η^2-peroxo) complexes.[136] However, more recently reported examples with redox-inactive Sc^{III} or Y^{III} as the second metal ion[137-138] also have lower ν(O-O) frequencies (but not as low as the dicopper complexes), so electron transfer from the second metal ion to the bound peroxo ligand is not required to lower the frequency of the side-on bound peroxo ligand. The fact that the ν(O-O) of CmlI-peroxo is observed at 791 cm^{-1} raises the strong possibility that its peroxo ligand may be bound in either the μ-η^2:η^2 or μ-η^1:η^2 bridging mode. Of these two modes, we favor the μ-η^1:η^2 bridging for the following reason: Site *a* has a substantially larger isomer shift (δ = 0.62(1) mm/s) than site *b* (δ = 0.54(1) mm/s), the latter value being associated with a more typical of high-spin ferric center. Mononuclear complexes with side-on bound peroxo groups generally have δ values between 0.58 and 0.67 mm/s (see Table 2-4), which suggests that site *a* of CmlI-peroxo could have a side-on peroxo ligand.

Table 2-4: Spectroscopic parameters of synthetic nonheme high-spin iron-peroxo complexes.

Complex[a]	λ_{max} (nm)	ε ($M^{-1}cm^{-1}$)	ν (O–O) (cm^{-1})	J (cm^{-1})	δ (ΔE_Q) (mm s^{-1})	ref
$[(TMC)Fe^{III}(\eta^1\text{-}OOH)]^2$	500 (sh)	450	870		0.51 (0.2)	113
$[Fe_2(Tp^{iPr2})_2(O_2CR)_2(\mu\text{-}\eta^1\text{:}\eta^1\text{-}O_2)]$	694	2650	888	66	0.66 (1.40)	103
$Fe^{III}(\mu\text{-}O)(\mu\text{-}\eta^1\text{:}\eta^1\text{-}O_2^{=})Fe^{III}$	577-650	1200-1500	830-853	≥110	0.53-0.55 (1.43-1.68)	104, 110, 139-141
$Fe^{III}(\mu\text{-}OR)(\mu\text{-}\eta^1\text{:}\eta^1\text{-}O_2^{=})Fe^{III}$	588-730	1500-3000	884-908	60-80	0.50-0.57 (0.96-1.35)	104, 111, 141
$[(py)_2Fe^{II}{}_2(dxlCO_2)_4(O_2)]$	500-550	1100	822	≈30(5)	0.65 (1.27) 0.52 (0.71)	130
nonheme $Fe^{III}(\eta^2\text{-}O_2^{=})$	520-835	500-650	816–827		0.58-0.67 (0.6-1.4)	113, 137-138, 142-143
$(TMC)Fe^{III}(\mu\text{-}\eta^2\text{:}\eta^2\text{-}O_2^{=})(Sc^{III})$	525	780	807/799		0.47 (0.50)	137-138
$(heme)Fe^{III}(\mu\text{-}\eta^2\text{:}\eta^1\text{-}O_2)Cu^{II}$			788–808			134, 144
$(heme)Fe^{III}(\mu\text{-}\eta^2\text{:}\eta^2\text{-}O_2)Cu^{II}$			747–767			134, 144

[a] Abbreviations used: $dxlCO_2$ = 2,6-bis(2',6'-dimethylbenzyl)-4-*tert*-butylbenzoate anion; py = pyridine; TMC, 1,4,8,11-tetramethylcyclam; Tp^{iPr2} = hydridotris(3,5-diisopropylpyrazolyl)borate anion.

Figure 2-13 illustrates the proposed μ-η^1:η^2-peroxo binding mode for the CmlI active site, which was modeled by introducing an O-atom to the oxo bridge between the iron atoms in the crystal structure of AurF-product complex (3CHT). It is not clear what factors cause this diiron active site to form an O_2-adduct distinct from the other four diiron enzyme O_2-adducts that have been characterized by resonance Raman spectroscopy. Perhaps the presumed third His ligand, deduced by comparison with the sequence of the structurally characterized AurF, promotes the shift in peroxo binding geometry from μ-η^1:η^1 to μ-η^1:η^2.

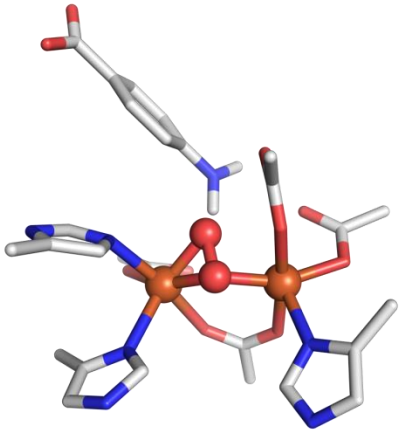

Figure 2-13: Proposed structure of CmlI-Peroxo built from the active site coordinates of oxidized AurF–*para*-nitrobenzoate complex (3CHT). An oxygen atom was introduced to convert the oxo bridge into a μ-η^1:η^2-peroxo bridge. Fe, O, C, N, and H atoms are shown in orange, red, dark grey, blue, and light grey, respectively.

What advantage might this difference in peroxo binding mode provide CmlI, and by inference, AurF? Reactivity data suggest that the decay of both peroxo intermediates is affected by the nature of the amine substrate, with more electron-rich substrates affording faster rates of decay (Figure 2-8C, *inset*).[145] It is thus plausible for CmlI and AurF to initiate the oxidation of their arylamine substrates by simple electron transfer to the peroxo intermediate (Scheme 2-1), thereby avoiding having to form oxidants more powerful than required for the reaction and affording the active site better control of the reaction coordinate. Accordingly, this mechanism may account for the inability of CmlI to catalyze either aliphatic or aromatic hydroxylation reactions despite the fact that its active site can accommodate a wide range of substrates.

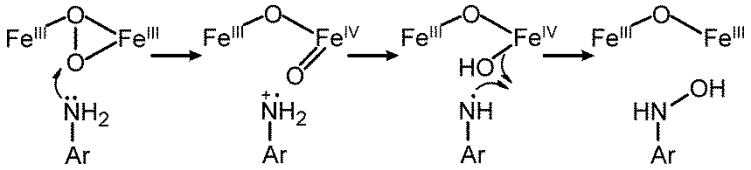

Scheme 2-1: Proposed mechanism for the first step in aryl-amine oxygenation by CmlI.

The mechanism shown in Scheme 2-1 would be a logical first step in the oxygenation of the arylamine substrate to the nitroaryl product. However, we have not detected the potential intermediate products, namely, the hydroxylamino- or nitroso-adducts of the NH_2-CAM substrate, during the reaction. Minor amounts of these intermediates were reported for reactions of both AurF and CmlI with their respective substrates in multiple turnover studies by Zhou and coworkers.[19, 78] The single exponential time course for the reaction of NH_2-CAM with CmlI-peroxo suggests that, if these discrete intermediates are formed, their subsequent conversion to chloramphenicol is very fast. Recently, Krebs, Bollinger and coworkers proposed that the AurF-peroxo adduct can react with the hydroxylamino-derivative of pAB by an interesting mechanism in which hydroxylation to form a dihydroxylamino-adduct is followed by 2-electron, 2-proton transfer to yield pNB and regenerate the AurF diferrous cluster.[85] Oxygen binding to the diferrous cluster would re-form the AurF-peroxo adduct so that the hydroxylamino adduct is catalytically converted to the nitro adduct without net utilization of the peroxo adduct. While it is possible that CmlI follows this same mechanism, our results (Figure 3, *inset*) show that approximately three CmlI-peroxo complexes are required for each chloramphenicol produced from NH_2-CAM, favoring the stepwise oxidation mechanism.

A proposal for an unsymmetrically bound peroxo intermediate absorbing at 450 nm reminiscent of CmlI-peroxo was recently advanced for the enzyme aldehyde deformylating oxygenase (ADO) based on dissimilar Mössbauer parameters for the two ferric ions in the complex. [46] As we propose here for CmlI, the authors postulated that ADO-peroxo is the reactive species that directly attacks its long chain fatty aldehyde substrate. However, it was also proposed that the O-O bond cleavage reaction following formation of the initial hemiacetal species is promoted by transfer of one electron from an external donor.[146-147] No similar role for an external donor is evident in the efficient single turnover reaction of CmlI (Figure 4). Instead, electron transfer from the amine function of the substrate may serve this role of promoting O-O bond cleavage as illustrated in Scheme 2-1. An alternative mechanism for ADO was suggested by our recent study in which it was observed that the enzyme can hydroxylate the terminal

methyl of the long-chain hydrocarbon formed as a product of long-chain aldehyde deformylation.[21] This implies that a high-valent species at the $Fe^{IV}Fe^{IV}$ oxidation state of MMO-Q is formed as a consequence of the O-O bond breaking reaction during deformylation. If this is the case, then an extra electron cannot be transferred to the peroxo intermediate in the ADO case. Similarly, electron transfer is not involved in the formation of MMO-Q prior to its reaction with methane.[94] This observation is in accord with the proposal made above in Scheme 2-1 that the difference in the type of substrate bond that can be oxygenated is a consequence of the availability of electrons to the peroxo intermediate.

Role of CmlI in Chloramphenicol Biosynthesis. Oxygenases in NRPS pathways have been shown to oxidize amino acid substrates in several modes, including: (a) prior to loading onto the peptidyl carrier protein (PCP) domain, (b) while the amino acid is tethered onto the PCP domain as a thioester, or (c) as a late-stage modification following release from the PCP.[148] We have shown in previous studies that L-pAPA beta-hydroxylation during chloramphenicol biosynthesis catalyzed by the diiron monooxygenase CmlA proceeds exclusively by the second route.[88] The reactivity of CmlI-peroxo was interrogated in the current study using the free precursor substrate L-pAPA, L-pAPA appended onto the chloramphenicol NRPS CmlP PCP domain, NH_2-CAM, and other benzylamine substrates (Figure 2-8C, *inset*). The L-pAPA-loaded NRPS T-domain did not result in an appreciable enhancement of the peroxo decay rate, indicating that, unlike CmlA, CmlI does not perform oxidation chemistry on the S-acylated amino acid. The ability of CmlI-peroxo to fully convert NH_2-CAM to chloramphenicol was demonstrated by LC-MS studies (Figure 2-7) and is consistent with steady state and whole cell turnover studies.[19] Thus, this reaction shows efficient six-electron oxidation of amine to a corresponding nitro derivative. The rate constant for CmlI-peroxo decay was significantly larger (~3x) for NH_2-CAM when compared to that of free L-pAPA, indicating that the installation of a nitro-group is enhanced by reduction of the L-pAPA carboxylate (which occurs during reductive cleavage from the NRPS) or installation of the dichloroacetyl group, or both. However, the efficient metabolism of NH_2-CAM observed here, considered together with earlier isotope feeding experiments used to order the modifications of CAM biosynthesis, [149-150] strongly suggest that CmlI functions as the last stage of CAM maturation as illustrated in Figure 2-13.

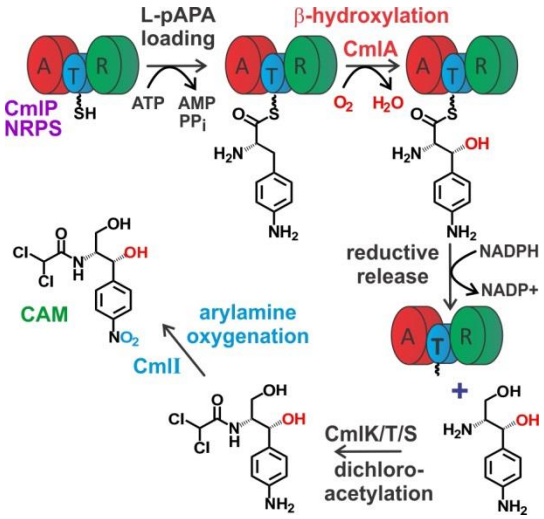

Figure 2-13: Role of CmlI in chloramphenicol biosynthesis.

Acknowledgements

Dr. Thomas Makris discovered CmlI, performed the initial molecular biology and biochemistry work required to isolate the gene and produce significant amounts of pure enzyme, and optimized the conditions required to stabilize the CmlI-P species. Dr. Makris also performed initial substrate assays. Dr. Van V. Vu performed the resonance Raman experiments described and analyzed the data. Dr. Katlyn Meier and Prof. Eckard Münck analyzed the Mössbauer samples. Dr. Brent Rivard assisted in protein expression and purification, as well as HPLC optimization for substrate assays. All the above provided insight and background research regarding this work. Dr. Joseph Dalluge assisted in mass spectral analysis.

Chapter 3

Spectroscopic Characterization of Intermediates in the Six-Electron Conversion of an Aryl-amine to an Aryl-nitro Product by CmlI

Portions of this chapter are reprinted (adapted) with permission from: Anna J. Komor, Brent S. Rivard, Ruixi Fan, Yisong Guo, Lawrence Que, Jr., and John D. Lipscomb. "Mechanism for Six-Electron Aryl-N-Oxygenation by the Non-Heme Diiron Enzyme CmlI" *J. Am. Chem. Soc.*, **2016**, *138*, 7411-7421.

Introduction

The enzyme-catalyzed six-electron oxidation of aryl-amines to aryl-nitro moieties is a process for which mechanistic consensus has not been reached. There are only three characterized enzymes known to perform this conversion: CmlI and AurF, both of which are non-heme dinuclear iron-cluster-containing enzymes, and PrnD, a Rieske-type non-heme iron oxygenase.[19, 66-67, 69, 75, 84] The cofactors of both of these enzyme classes are only capable of at most 2-electron redox chemistry. Thus, the observed 6-electron aryl-amine (NH_2-Ar) oxidation reaction of these enzymes presents a mechanistic puzzle.

The proposals for the mechanism of NH_2-Ar to aryl-nitro (NO_2-Ar) oxidation by diiron enzymes can be grouped into two general hypotheses. In the sequential three-oxidation hypothesis, (Scheme 3-1, pathway I), the diiron cluster utilizes external electrons to activate O_2 in three separate events. Each activated oxygen species, likely a diiron peroxo intermediate (see below), effects a 2-electron oxidation of the substrate or an intermediate. A single turnover thus requires six exogenous electrons. The NH_2-Ar substrate is converted to an aryl-hydroxylamine (NH(OH)-Ar) by the first oxidation, to aryl-nitroso (NO-Ar) or aryl-dihydroxylamine ($N(OH)_2$-Ar) by the second oxidation and to the NO_2-AR product by the final oxidation. The diiron cluster returns to the diferric resting state at the end of the cycle. This mechanism was originally proposed by Hertweck and Winkler, based on work done on whole cells over-expressing AurF,[83] and expanded by Zhao and coworkers based on work on purified AurF and CmlI.[66, 75] This type of mechanism requires either release of intermediates with subsequent rebinding at another activated metal center or a system to internally transfer the remaining required oxidizing equivalents between active sites in different subunits. The latter possibility seems unlikely given that structural studies show that AurF is only a homodimer, and three sets of oxidizing equivalents, or a homotrimer, would be required to complete the reaction in this case.[78]

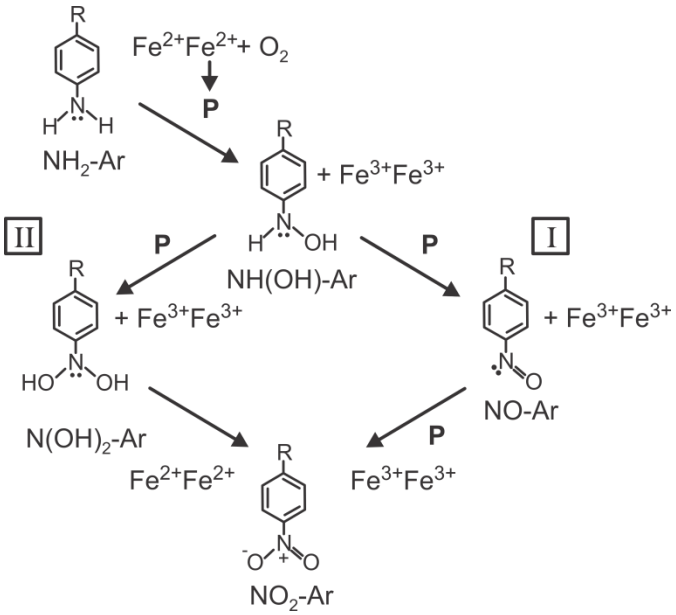

Scheme 3-1: Two mechanistic hypotheses for aryl-amine oxygenation mediated by diiron cluster enzymes. (I) Sequential three-oxidation mechanism requiring six external electrons (2 for each peroxo-intermediate) per turnover and (II) substrate-mediated reduction mechanism requiring a net of two external electrons per turnover because the diferrous cluster is regenerated at the end of the turnover cycle.

The second mechanistic hypothesis, introduced by Bollinger, Krebs and colleagues, invokes a substrate-based reduction step (Scheme 3-1, pathway II).[85] Like the three-step oxidation mechanism, the substrate-based reduction mechanism begins with two 2-electron oxidations to form first NH(OH)-Ar, and then $N(OH)_2$-Ar, intermediates. Using stopped-flow UV-Vis absorbance and Mössbauer spectroscopies, it was reported that $N(OH)_2$-Ar intermediate can act as a reductant, reducing the diferric diiron cluster to diferrous while itself being oxidized to the final NO_2-Ar product. The overall reaction utilizes only two diiron-peroxo species and results in a diferrous cluster at the end of the reaction cycle. As a result, only four exogenous electrons are required for O_2 activation in a single turnover, and the final diferrous diiron cluster can be used to activate O_2 for the next cycle. Consequently, when considered over multiple cycles, only two external electrons are required per cycle to sustain turnover.

CmlI is an ideal enzyme with which to evaluate these two mechanistic hypotheses for aryl-amine oxidation. We have shown previously that the chemically competent intermediate of the reaction cycle, a diferric peroxo species, CmlI-peroxo (**P**), can be formed in high yield and has a distinguishable chromophore that can be followed by UV-Vis absorption spectroscopy at 500 nm. **P** is remarkably stable ($t_{1/2}$ = 3 h at pH 9 and 4 °C)[52] in contrast to the peroxo

intermediates of AurF and other diiron oxygenases.[33, 49, 53] This stability allows the key intermediate to be formed, degassed, transferred to and from an anaerobic chamber, transferred to stopped-flow or freeze-quench instruments, and reacted with the NH_2-CAM substrate or one of the other pathway intermediates. Here it is shown that aryl-amine oxygenation proceeds by a third mechanism in which the reaction cycle ends with the diiron cluster in the diferric state. An $N(OH)_2$-Ar derivative is not a required intermediate. However, diiron cluster reduction by another pathway intermediate serves to increase efficiency and reduce the need for external reducing equivalents in a single turnover. This new mechanism requires only two exogenous electrons, supplied at the beginning of the reaction cycle.

Results

Tracking Oxygen Atom Incorporation into Chloramphenicol Product. To determine the source of the oxygen atoms in the nitro-function of CAM, P was formed under either an $^{16}O_2$ or $^{18}O_2$ atmosphere and then reacted with NH_2-CAM. Reactions were carried out at 4 °C with 0.3 equivalent of substrate, allowed to run for 10 min and then acid quenched as described in Chapter 5. Equivalents of substrate here and in future experiments are calculated vs. concentration of P unless otherwise stated. When $^{18}O_2$-P was reacted with NH_2-CAM in an $^{18}O_2$ environment, the resulting CAM product was 93 ± 2% doubly labeled with ^{18}O (Table 3-1). NO-CAM, observed as a minor product, was >95% singly labeled with ^{18}O. Based on the isotopic purity of the $^{18}O_2$ source, we could expect a maximum of 98% incorporation. Additional ^{16}O incorporated during the reaction is likely to be due to contamination from atmospheric O_2 during experimental manipulations. Thus, it appears that both of the O atoms of the CAM product derive from P (and therefore from O_2), and not from H_2O. To confirm this, reduced CmlI ($CmlI^{red}$) was exchanged into $H_2{}^{18}O$ buffer and then supplied with $^{16}O_2$ to form $^{16}O_2$-P. Reaction with NH_2-CAM yielded only ^{16}O-containing product (Table 1).

When the reaction of $^{18}O_2$-**P** with NH_2-CAM was carried out in an $^{16}O_2$ atmosphere, approximately 50% of the CAM produced was doubly labeled, while the remainder was either singly labeled (~40%) or had no ^{18}O incorporation (10%) (Table 3-1). NO-CAM product labeling fell slightly, but remained >90%. No significant difference in oxygen incorporation was observed when 1.0 equivalent of substrate was used instead of 0.3.

Three possible explanations were considered for why the aerobic reactions of $^{18}O_2$-**P** with NH_2-CAM incorporate a significant amount of ^{16}O: (1) **P** exchanges with water, converting $^{18}O_2$-

P to $^{18}O/^{16}O$-**P** and/or $^{16}O_2$-**P**, (2) **P** exchanges with the atmospheric O_2, converting $^{18}O_2$-**P** to $^{16}O_2$-**P**, (3) **P** re-forms with $^{16}O_2$ from the aerobic atmosphere after the **P**-decay species, diferric CmlI (CmlI^{ox}), is re-reduced by a pathway intermediate.

Table 3-1: Oxygen incorporation into CAM products in the reaction of **P** with NH_2-CAM.[a]

product	oxygen incorporation	**oxygen isotope**: atmosphere / **P** / solvent		
		$^{18}O_2/^{18}O_2/H_2{}^{16}O$	$^{16}O_2/^{18}O_2/H_2{}^{16}O$	$^{16}O_2/^{16}O_2/H_2{}^{18}O$
		%	%	%
CAM	^{16}O, ^{16}O	0.4 ± 0.2	10 ± 1	100
	^{16}O, ^{18}O	7 ± 2	44 ± 1	0
	^{18}O, ^{18}O	93 ± 2	47 ± 2	0
NO-CAM	^{16}O	4 ± 1	8 ± 6	98 ± 2
	^{18}O	96 ± 1	92 ± 6	3 ± 2

[a] $^{16}O_2$-**P** or $^{18}O_2$-**P** was reacted with 0.3 equivalents NH_2-CAM under different atmosphere and solvent conditions shown. Resultant products were analyzed by LCMS as described in the Experimental Procedures. All reactions done in buffer: 50 mM Bicine, pH 9, 4 °C.

It was shown above that the reaction of $^{16}O_2$-**P** in $H_2{}^{18}O$ yields only ^{16}O product, indicating that neither the peroxo species nor products exchange with water. This finding rules out the first possible explanation. To test the second possibility and determine whether **P** can exchange with atmospheric O_2, a stock of $^{18}O_2$-**P** was made and then placed under a steady stream of $^{16}O_2$. At time points between 1 and 100 min, an aliquot of **P** was removed and reacted with NH_2-CAM for 10 minutes. No time dependent change in the ^{18}O incorporation pattern was observed (Figure 3-1), showing that **P** does not exchange with ambient O_2. In the absence of alternative explanations, the reduction of the enzyme by a substrate-based intermediate to allow re-formation of **P** with atmospheric $^{16}O_2$ as part of the reactive cycle is strongly supported. The fact that >90% of the NO-CAM remained ^{18}O-labeled also supports the hypothesis that the first oxygen atom is added by an $^{18}O_2$-**P** and the second by a $^{16}O_2$-**P**. The reducing agent required to re-form **P** is identified below.

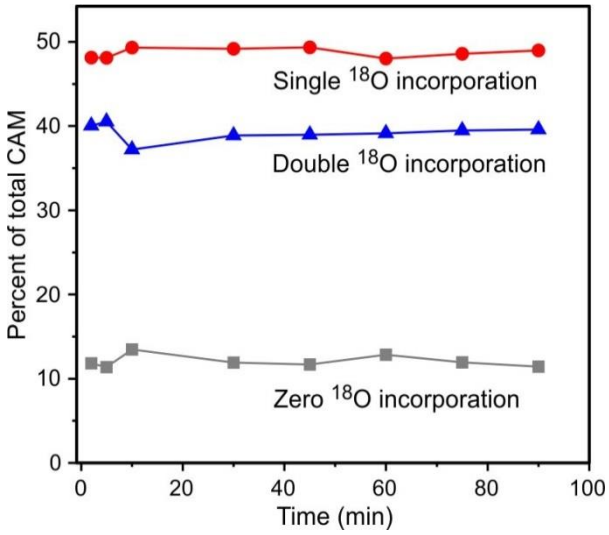

Figure 3-1: CmlI-Peroxo exchange test. Product isotope ratios when $^{18}O_2$-**P** was incubated under a steady stream of $^{16}O_2$. Time indicates the length of time $^{18}O_2$-**P** had been incubating when it was removed from the reaction vessel and reacted with NH_2-CAM. The reaction with substrate was allowed to proceed for 10 min before acid quench. Buffer: 50 mM Bicine, pH 9, 4 °C.

Although the fraction of CAM with a mixed oxygen-labeled nitro group clearly increases in an $^{16}O_2$ atmosphere, a significant portion of the product remains doubly labeled with ^{18}O. A possible explanation for this observation is that a pathway intermediate prior to CAM escapes the active site and subsequently reacts with unreacted $^{18}O_2$-**P**. This possibility is explored below.

Reaction of CmlI with NO-CAM and Determination of NO-CAM as a Substrate-Based Intermediate. The detection of NO-CAM by LCMS during turnover of NH_2-CAM suggests the possibility that NO-CAM is an intermediate in the reaction pathway. To test this possibility, NO-CAM was synthesized from CAM using a zinc reduction method previously reported.[151] An anaerobic solution containing 1 eq. of NO-CAM and diferrous CmlI ($CmlI^{red}$) was rapidly mixed with O_2-saturated buffer at 4 °C (Scheme 3-2 and Figure 3-2) to yield Sample A.

$$CmlI^{red} + \text{NO-CAM} \rightarrow CmlI^{red}\text{–[NO-CAM]}$$

$$CmlI^{red}\text{–[NO-CAM]} + O_2 \rightarrow \mathbf{P}\text{–[NO-CAM]}$$

$$\mathbf{P}\text{–[NO-CAM]} \rightarrow \text{Sample A}$$

Scheme 3-2: Production of sample A from the reaction of $CmlI^{red}$, O_2, and NO-CAM.

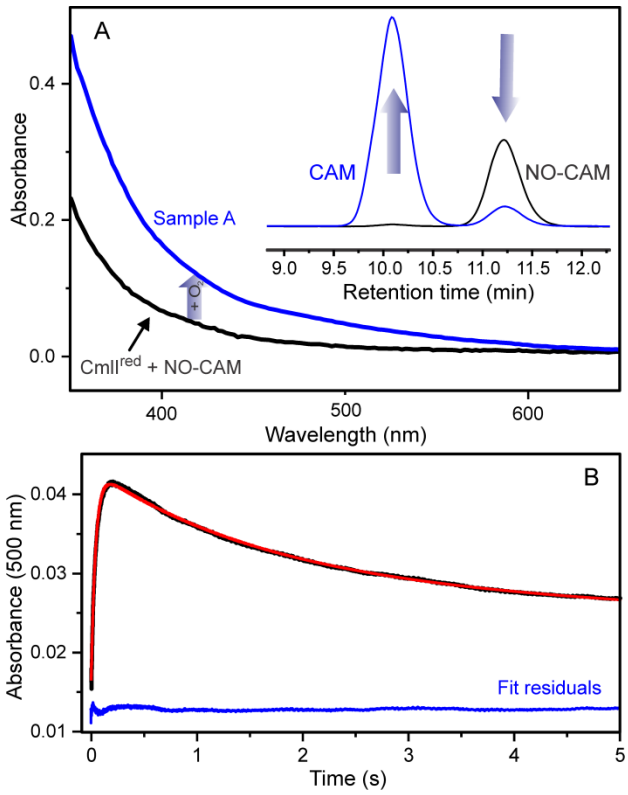

Figure 3-2: Reaction of CmlI^{red} with NO-CAM. (A) 100 μM NO-CAM added anaerobically to 100 μM CmlI^{red}, forming the nearly stoichiometric ES complex CmlI^{red}-[NO-CAM] (black trace) that was rapidly mixed with O_2 saturated buffer (~1.8 mM) to yield Sample A (blue trace). Inset: HPLC analysis of CmlI^{red}-[NO-CAM] yielded mostly NO-CAM (black HPLC trace) as expected, while analysis of Sample A shows that the NO-CAM was converted into CAM product (blue HPLC trace). (B) Stopped-flow time course of the reaction described in (A). The time course (black) fits to a triple summed exponential (red, residuals in blue). $1/\tau_1 = 24 \pm 1\ s^{-1}$, $1/\tau_2 = 0.6 \pm 0.1\ s^{-1}$ and $1/\tau_3 = 0.05 \pm 0.01\ s^{-1}$. Buffer: 50 mM Bicine, pH 9, 4 °C.

The time course of the reaction monitored at 500 nm by stopped-flow spectroscopy is fit well by the sum of three exponential expressions with reciprocal relaxation times of 24 ± 1, 0.6 ± 0.1 and 0.05 ± 0.01 s^{-1}, respectively (Figure 3-2B). Given the previously observed rapid, irreversible formation of **P**, and the direction and magnitude of the spectral change,[52] it is likely that the fastest of the values correlates with the rate constant for **P** formation. However, it remains unclear whether the slower two phases arise from a two-step reaction or two parallel pathways leading to loss of **P**. In either case, these reciprocal relaxation times imply that the reaction steps occur with rate constants 100-1000 fold faster than the rate constant for **P** autodecay (~0.0006 s^{-1}). It is evident that the increase in rate constant for **P** decay was caused by a reaction(s) that leads to formation of CAM because analysis of Sample A by HPLC showed only this product (Figure 3-2A, inset). The yield of CAM was ~50% in these experiments. Less

than stoichiometric yields were consistently observed for reactions utilizing NH_2-CAM and, to a lesser extent, NO-CAM as substrates. The low yields may result from uncoupling of the reaction at the high enzyme and substrate concentrations used in single turnover experiments (see discussion). A control reaction of diferric CmlI and NO-CAM yielded no CAM product or spectral changes either in the presence or absence of O_2, demonstrating that NO-CAM reacts exclusively with the **P** form of CmlI.

Reaction of NH(OH)-CAM with CmlI and Determination of NHOH-CAM as a Substrate-Based Intermediate and Catalytically Relevant Reducing Agent. NH(OH)-CAM was synthesized from NO-CAM by reaction with reduced glutathione.[151] NH(OH)-CAM was reacted separately with P and $CmlI^{ox}$, under aerobic conditions followed by acid quench. Remarkably, both reactions yielded CAM as the primary product, with a small amount of NO-CAM as either a product or a side product of acid-mediated decay of NH(OH)-CAM. NH(OH)-CAM is a relatively unstable compound which could potentially yield CAM in a non-specific reaction. To explore this possibility, it was acid quenched in buffer. This control yielded only NO-CAM product, likely resulting from the acid-mediated decay of NH(OH)-CAM in the quench procedure. These results indicate that the observed CAM production was mediated by CmlI (Figure 3-3).

When reacted aerobically with a 10-fold excess of NH(OH)-CAM, **P** and $CmlI^{ox}$ produced 5.9 ± 0.6 and 5.7 ± 0.1 equivalents of CAM product, respectively, under the conditions of Figure 3-3. The remaining NH(OH) -CAM was converted to NO-CAM in the acid quench. Thus, both reactions are catalytic with no requirement for external reducing equivalents. This result suggests that NH(OH)-CAM can provide the reducing equivalents required to reduce $CmlI^{ox}$ and prime it to produce **P** in the presence of O_2.

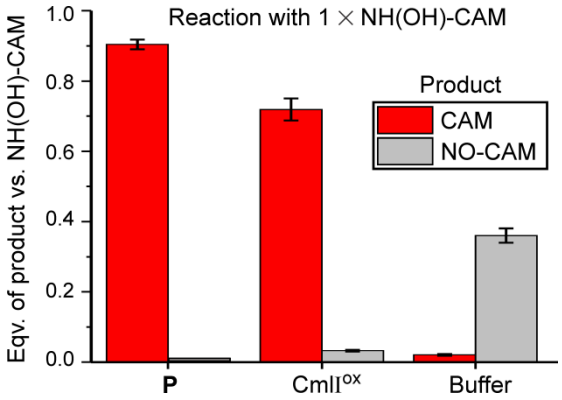

Figure 3-3: Reaction of **P** and CmlI^{ox} with NH(OH)-CAM. The aerobic reaction of 300 μM **P** or CmlI^{ox} with one equivalent NH(OH)-CAM yields primarily CAM product. Control incubation with buffer (50 mM Bicine, pH 9) yields primarily NO-CAM, formed during the acid quench of the reaction. The apparent yield of NO-CAM is decreased about 50% by dimerization of the NO-CAM species into azoxy-CAM.[83, 86, 152] Buffer: 50 mM Bicine, pH 9, 4 °C.

The reaction between CmlI^{ox} and NH(OH)-CAM was followed by UV-vis spectroscopy to characterize pathway intermediates. The addition of NH(OH)-CAM directly to CmlI^{ox} (Figure 3-4 and Scheme 3-3) in an anaerobic environment resulted in the formation of a diferrous CmlI Sample B. An aliquot of Sample B removed and quenched anaerobically yielded an HPLC peak with the same retention time as NO-CAM. Oxygen was then added to sample B, forming primarily CmlI^{ox}, Sample C. HPLC analysis of Sample C showed that the NO-CAM species had disappeared and CAM was formed in its place. Total CAM yield was ~70% versus initial **P** concentration.

$$\text{CmlI}^{ox} + \text{NH(OH)-CAM} \rightarrow \text{Sample B}$$
$$\text{Sample B} + O_2 \rightarrow \text{Sample C}$$

Scheme 3-3: Production of samples B and C from the reaction of CmlI^{ox} and NH(OH)-CAM.

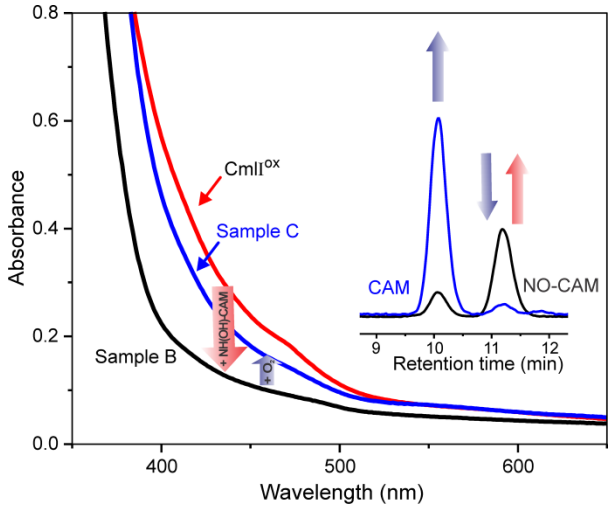

Figure 3-4: Stepwise characterization of the reaction of CmlI^{ox} with NH(OH)-CAM by UV-vis and HPLC. Optical absorbance spectra and product analysis in the reaction of 560 µM NH(OH)-CAM with 560 µM anaerobic CmlI^{ox} (red spectrum), which yields Sample B (black spectrum) which contains NO-CAM product (black HPLC trace). Addition of O_2 yields Sample C (blue spectrum) which contains primarily CmlI^{ox} and CAM product (blue HPLC trace). Buffer: 50 mM Bicine, pH 9, 4 °C.

The oxidation state of the diiron cluster at each stage of the reaction was directly determined in a parallel Mössbauer experiment as shown in Table 3-2 and Figure 3-5. The anaerobic addition of approximately one equivalent of NH(OH)-CAM to CmlI^{ox} generates Sample B, the major component, representing 65% of the total iron in the sample, was assigned to a diferrous cluster. The remaining species were assigned to diferric clusters (~30%) and a small amount of unassigned mononuclear ferric material (~7%). Addition of O_2 to this sample formed Sample C, which by UV-Vis appeared as primarily CmlI^{ox} and accordingly exhibited the Mössbauer parameters of the diferric enzyme, which represents ~ 90% of the total iron in the sample. The different Mössbauer parameters of the CmlI^{ox} before and after the reaction with NH(OH)-CAM could be due to the perturbation of the diiron centers by substrate/product binding or a change in the pH of the cluster environment; further studies are needed to resolve the detailed mechanisms resulting in such a difference.

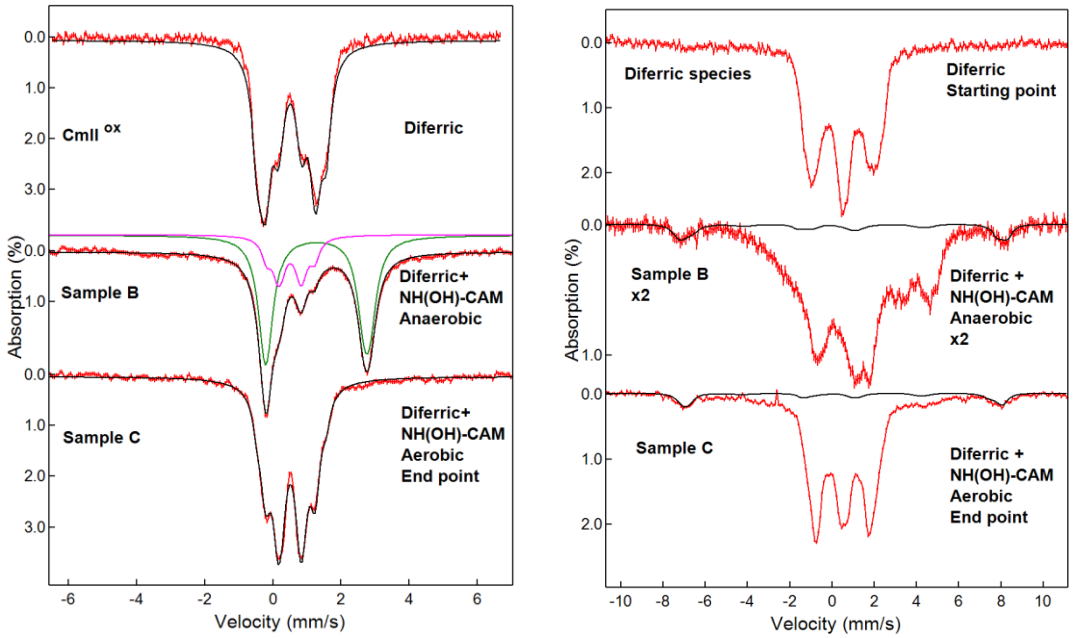

Figure 3-5: Stepwise characterization of the diiron center during NH(OH)-CAM oxidation by CmlI^{ox} by Mössbauer spectroscopy. Left: Mössbauer spectrum measured under 0.45 kG and 4.2 K of various samples indicated in the figure; Purple: the simulation for diferric species (CmlI^{ox}) in the sample; Green: the simulation for diferrous species (CmlI^{red}) in the sample Right: the corresponding Mössbauer spectra recorded under 7.0 T and 4.2 K. Red: experimental spectra; Black: spectral simulation curves; Purple: the simulation for diferric species (CmlI^{ox}) in the sample; Green: the simulation for diferrous species (CmlI^{red}) in the sample. For the spectra in the right panel, the mono-ferric species represents ~0%, ~7% and ~ 9% of the total iron in the sample from top to bottom.

Table 3-2: Mössbauer quantification of CmlI forms during single turnover reactions

	Sample[a]					
Species[b] (%)	B	C	D[c]	E	F[d]	G
CmlI^{ox}	30 ± 3	90 ± 3	17 ± 3	85 ± 3	35 ± 3	75 ± 5
CmlI^{red}	65 ± 3	0	68 ± 2	0	30 ± 3	0
Unassigned mononuclear ferric species	7 ± 3	9 ± 3	14 ± 3	14 ± 3	30 ± 5	23 ± 5

[a]Mössbauer spectra and parameters of the species found in each sample are presented in Supporting Information Figures S2-S5. [b]Species are identified by the oxidation state of the diiron cluster. They may also have intermediate products bound in some cases. An ~10% conversion to diferric is expected in the Mössbauer samples vs the optical time course experiments due to autodecay of **P** during addition time required to prepare these high concentration samples. The presented quantifications do not include **P**, see Supporting Information for details. [c]Starting sample of **P** prior to degassing contained 72% **P**, 24% CmlI^{ox}, and 4% unassigned ferric species. [d]Starting sample of **P** prior to degassing contained 60% **P**, 36% CmlI^{ox}, and 4% unassigned ferric species.

Addition of approximately one equivalent of NH(OH)-CAM to **P** resulted in Sample D (Scheme 3-4), which has a UV-Vis spectrum that reflects a mixture of diferric and diferrous species (Figure 3-6, black trace). Analysis of Sample D by HPLC shows generation of CAM product in ~45% yield vs. initial NH(OH)-CAM concentration (Figure 3-6, inset, black). Addition of O_2 to Sample D produced Sample E (Figure 3-6, red trace) and an increase in CAM product, presumably arising from unreacted NH(OH)-CAM (Figure 3-6, inset, red). The spectrum of Sample E is best fit by summing the spectra of approximately 80% $CmlI^{ox}$ and 20% **P**.

$$CmlI^{red} + O_2 \rightarrow \mathbf{P}$$
$$\mathbf{P} + \text{NH(OH)-CAM} \rightarrow \text{Sample D}$$
$$\text{Sample D} + O_2 \rightarrow \text{Sample E}$$

Scheme 3-4: Production of samples D and E from the reaction of $CmlI^{red}$, O_2, and NH(OH)-CAM.

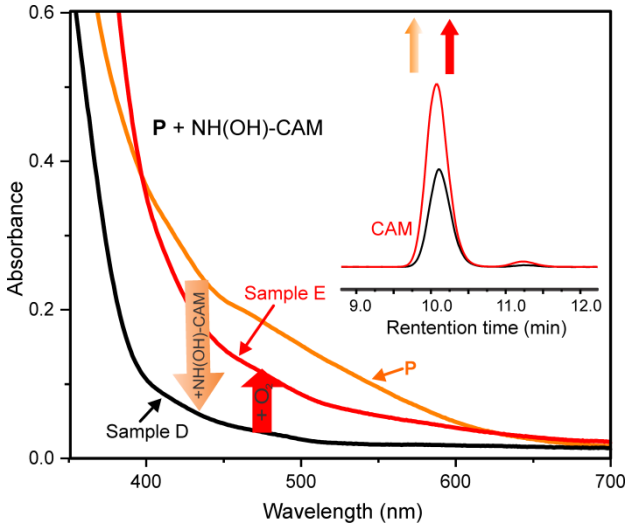

Figure 3-6: Stepwise characterization of the reaction of **P** with NH(OH)-CAM. Absorbance spectra and product analysis in the anaerobic reaction of 300 µM NH(OH)-CAM with 300 µM **P** (orange trace), which yields Sample D (black spectrum). Addition of O_2 forms Sample E (red trace). Inset: HPLC analysis of CAM and NO-CAM products from Sample D (black trace) and Sample E (red trace). Buffer: 50 mM Bicine, pH 9, 4 °C.

Mössbauer analysis of parallel samples (Figure 3-7) is generally consistent with the results observed by UV-Vis spectroscopy. In the Mössbauer experiment, **P** was formed in 72% yield and then degassed, leaving ~ 60% **P** and ~36% diferric CmlI (plus 4% mono-ferric

material). After anaerobic addition of one equivalent of NH(OH)-CAM versus total active site concentration and a 5 minute incubation, the resulting Sample D was ~68% CmlI^{red} and ~17% diferric clusters (Table 3-2). The observation of CmlI^{red} and CAM (Figure 5) suggests that this reaction proceeds at least in part by the route proposed by Bollinger, Krebs and coworkers for reaction of NH(OH)-Ar with the peroxo intermediate of AurF. The latter reaction yields NO_2-Ar and diferrous AurF (see Scheme 2, pathway II). [85] The generation of 68% CmlI^{red} was accompanied in this experiment by production of 62% CAM (product yield differences were observed between the optical and Mössbauer experiments, but the trends remained the same). These values support the reduction of CmlI^{ox} by N(OH)$_2$-CAM to yield roughly equal amounts of CAM and CmlI^{red}. A small amount of NO-CAM is also observed suggesting that the CmlI^{ox} fraction also reacts with NH(OH)-CAM to yield CmlI^{red} and NO-CAM. Consequently, only part of the observed CmlI^{red} derives from pathway II, thereby slightly decreasing the relative yield of CAM.

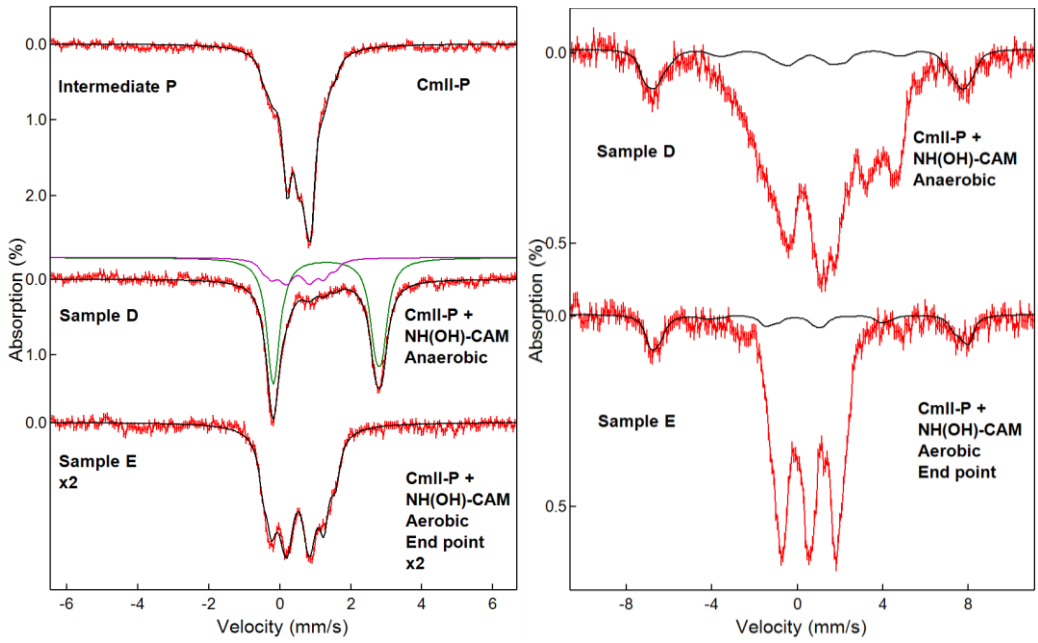

Figure 3-7: Stepwise characterization of diiron center during the NH(OH)-CAM oxidation by **P**. Left: Mössbauer spectrum measured under 0.45 kG and 4.2 K of various samples indicated in the figure; Right: the corresponding Mössbauer spectra recorded under 7.0 T and 4.2 K. Red: experimental spectra; Black: spectral simulation curves; Purple: the simulation for the diferric species (CmlI^{ox}) in the sample; Green: the simulation for the diferrous species (CmlI^{red}) in the sample. For the spectra in the right panel, the mono-ferric species represents ~14% of the total iron in the sample in both spectra. The detailed relative iron concentrations of different species in each spectrum are listed in Table 2 of the main text.

Addition of excess O_2 to Sample D formed Sample E, which Mössbauer spectra show to contain ~85% CmlI^{ox}. This value is similar to the approximately 80% CmlI^{ox} and 20% **P** observed by UV-Vis spectroscopy. The difference in the percentages derived from UV-Vis and Mössbauer data can be attributed to some **P** decay during the extended Mössbauer sample preparation process. Formation of Sample E is accompanied by formation of an additional 10% CAM product, which probably arises from the re-formation of **P** and its reaction with residual NH(OH)-CAM. It is unclear why the remaining unreacted CmlI^{red} is converted to CmlI^{ox} rather than **P** but we demonstrate above that the process of forming **P** is less than stoichiometric, resulting in a significant amount of adventitious CmlI^{ox} formation.

Reaction of CmlI^{red}, O_2, and NH_2-CAM Confirms NH(OH)-CAM and NO-CAM as Intermediates. It is shown above that **P** reacts individually with NH_2-CAM, NH(OH)-CAM and NO-CAM to produce chloramphenicol; however it is also important to demonstrate the reaction of NH_2-CAM beginning with CmlI^{red} also proceeds through the NH(OH)-CAM and NO-CAM intermediates. Accordingly, the reaction between NH_2-CAM, CmlI^{red}, and O_2 was monitored in a stepwise fashion using UV-Vis spectroscopy (Figure 3-8 and Scheme 3-5). The addition of O_2 to CmlI^{red} formed **P**, which was made anaerobic and then reacted with one equivalent of NH_2-CAM. The resulting species, Sample F, lacks the strong absorbance band at 375 nm that is characteristic of CmlI^{ox} and the band at 500 nm characteristic of **P**. Sample F looks similar to CmlI^{red} save for an additional shoulder at ~ 400 nm, which may be attributable to the presence of a substrate or product. NO-CAM has significant absorbance at 400 nm, and so a sample of CmlI^{red} combined with NO-CAM was prepared for comparison. Sample F exhibits a spectrum similar to that of the comparison sample, supporting its assignment as CmlI^{red} bound to one equivalent of NO-CAM. Differences between Sample F and authentic diferrous CmlI-NO-CAM can be attributed to an estimated 10% O_2 contamination introduced during handling of the **P** sample, leading to oxidation of the diferrous cluster after the CmlI^{red}-NO-CAM complex is formed. When oxygen was added to Sample F, a species which exhibits a spectrum that overlays with an independently prepared sample of decayed **P** (i.e. CmlI^{ox}) was observed (Sample G).

$$CmlI^{red} + O_2 \rightarrow \mathbf{P}$$

$$\mathbf{P} + NH_2\text{-CAM} \rightarrow \text{Sample F}$$

$$\text{Sample F} + O_2 \rightarrow \text{Sample G}$$

Scheme 3-5: Production of samples F and G via the reaction of $CmlI^{red}$, O_2, and NH_2-CAM.

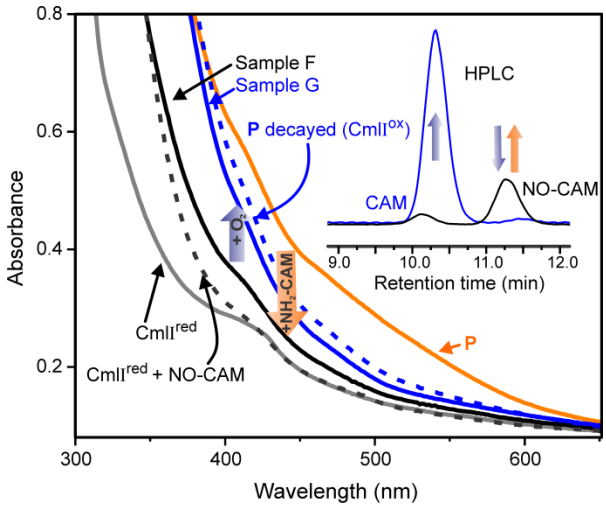

Figure 3-8: Spectroscopic snapshots of the CmlI catalytic cycle and HPLC analysis of associated products. The reaction began with 600 μM $CmlI^{red}$ (grey trace), to which O_2 was added to form **P** (orange trace). Anaerobic addition of 600 μM NH_2-CAM yields Sample F (solid black trace), proposed to be $CmlI^{red}$-NO-CAM by comparison to independently prepared 600 μM $CmlI^{red}$-NO-CAM (dotted black trace). The addition of O_2 to Sample F yields Sample G (solid blue trace), which nearly overlays with an independently prepared 600 μM decayed **P** sample (dotted blue trace). Inset: HPLC analysis of products in Sample F (black trace) and Sample G (blue trace). Sample F yields NO-CAM as the primary product and Sample G shows that NO-CAM has been consumed and CAM produced. Buffer: 50 mM Bicine, pH 9, 4 °C

Aliquots of Sample F and G were analyzed by HPLC. Sample F was found to contain primarily NO-CAM in an acid quench experiment. Repeating this experiment using a spin quench method gave the same results, eliminating the possibility that the sample contained NH(OH)-CAM which was then converted to NO-CAM under acidic conditions. A small amount of CAM was also present corroborating the 10% O_2 contamination during handling of **P** proposed above. An aliquot of the reaction end point Sample G contained no NO-CAM, presumably because it had been converted to CAM, which was detected as the sole product. These results suggest that CmlI is re-reduced concomitantly with the production of NO-CAM, and that the addition of O_2 converts the new $CmlI^{red}$ to $CmlI^{ox}$ (presumably with **P** as an intermediate) while NO-CAM is converted to CAM. The yield of CAM from a single turnover reaction using NH_2-

CAM as the substrate is ≤ 30%, in contrast to the nearly stoichiometric yields observed when using NH(OH)-CAM as the substrate in a single turnover experiment.

Corroborating evidence for the proposed oxidation states was provided by analyzing a parallel experiment by Mössbauer spectroscopy (Table 3-2 and Figure 3-9). **P** was formed in ~60% yield as CmlI^{red} reacted with O_2. The remaining iron was 36% unreacted CmlI^{ox} and 4% of a paramagnetic component that can be attributed to adventitious mononuclear iron sites in the enzyme. Formation of Sample F by addition of NH_2-CAM to **P** in the absence of excess O_2 causes the disappearance of >90% of **P** and the emergence of CmlI^{red}. Interestingly, only ~55% of **P** decays to CmlI^{red} in Sample F; the rest decays to one or more unidentified mononuclear ferric species, representing ~ 30% of the total iron in the sample. Addition of O_2 to yield sample G regenerates ~75% diferric enzyme in the sample, the rest of the sample is still the mononuclear ferric species (~ 23%). Therefore, the Mössbauer results suggest that **P** is prone to degradation by an unknown mechanism when reacting with NH_2-CAM under the experimental conditions we applied, causing significant uncoupling of the reaction. Based on the amount of CmlI^{red} generated (35%) in the anaerobic reaction, it is understandable that the yield of CAM from a single turnover reaction using NH_2-CAM as the substrate is sub-stoichiometric as observed in HPLC analysis.

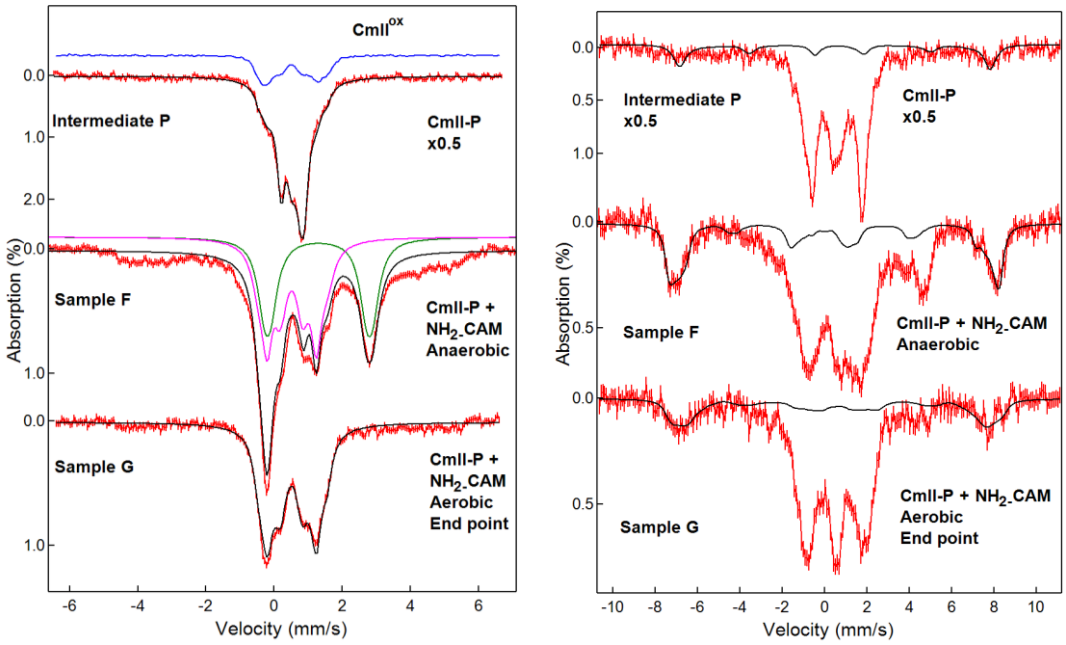

Figure 3-9: Stepwise characterization of diiron center during NH_2-CAM oxidation by **P** by : Mössbauer spectroscopy. Left: Mössbauer spectrum measured under 0.45 kG and 4.2 K of various samples indicated in the figure; Right: the corresponding Mössbauer spectra recorded under 7.0 T and 4.2 K. Red: experimental spectra; Black: spectral simulation curves; Blue: the 36% diferric ($CmlI^{ox}$) species in the sample containing **P**; Purple: the simulation for diferric species ($CmlI^{ox}$) in the sample; Green: the simulation for diferrous species ($CmlI^{red}$) in the sample. The spectra in the left panel were used for characterizing the different oxidation state of the diiron center; and the spectra in the right panel were used for quantifying the amount of mono-ferric species. For the spectra in the right panel, the mono-ferric species represents ~5%, ~30% and ~ 23% of the total iron in the sample from top to bottom. The detailed relative iron concentrations of different species in each spectrum are listed in Table 3-2.

CmlI is in the Oxidized State After a Single Turnover. It has been reported that the AurF single turnover ends with the enzyme in the diferrous state (Scheme 3-1, pathway II).[10] Under conditions of stoichiometric NH(OH)-Ar substrate and excess O_2, the AurF diferric peroxo species re-formed and was detected by its characteristic Mössbauer spectrum and absorbance at 500 nm.[10] It is shown here that the reactions of **P** with NH_2-CAM and NO-CAM end with CAM production and CmlI in the diferric state. In addition, the reaction of **P** with NH(OH)-CAM yields an intermediate diferrous state and CAM prior to O_2 addition. When assessed by its optical spectrum, a fraction of this sample is found as **P** at its completion. The $N(OH)_2$ reduction mechanism proposed by Bollinger and coworkers suggests that the reaction of **P** with a substoichiometric amount of NH_2-Ar substrate should result in the decay and partial reformation of **P**. The conclusion that CmlI does not end up in the reduced state after a single turnover of the native substrate is confirmed by the time course of a reaction of **P** with a substoichiometric

concentration of NH_2-CAM shown in Figure 3-10, red trace. Rapidly mixing **P** with 0.25 or 0.5 equivalents of NH_2-CAM in an oxygenated buffer at 4 °C led to only a rapid decay of **P** to $CmlI^{ox}$. In contrast, the reaction with 1.0 equivalent NH(OH)-CAM showed decay and then partial reformation of **P** within two seconds (Figure 3-10, blue trace). The observation of re-formed **P** suggests that the reaction of **P** with NH(OH)-CAM leads to substantial formation of the diferrous cluster, as reported for AurF-peroxo and NH(OH)-benzoate.[85] Rates of **P** decay and reformation are sufficiently similar such that only a small percentage of decay is observed before the reformation process begins. Thus, using equivalents of NH(OH)-CAM below or above the stoichiometric amount masks the reformation process.

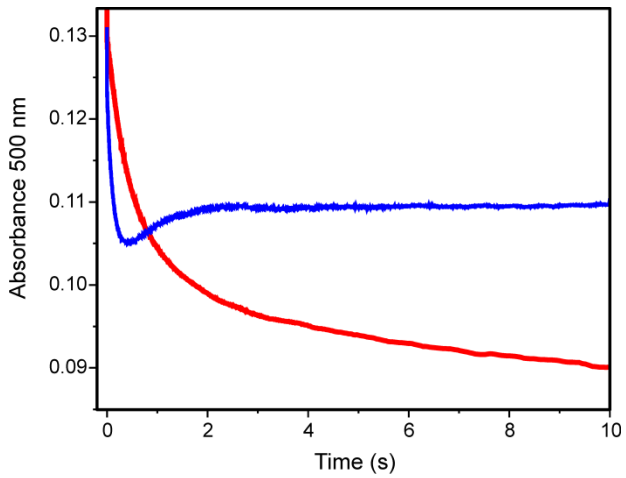

Figure 3-10: Single turnover reaction of **P** with 0.5 x NH_2-CAM (red trace) and 1.0 x NH(OH)-CAM (blue trace). Single wavelength (500 nm) stopped flow traces for the reaction of 260 μM **P** and 130 μM NH_2-CAM or 260 μM NH(OH)-CAM (post-mix concentrations) in the presence of excess O_2. No **P** reformation is observed in the reaction with the native substrate NH_2-CAM, suggesting that the in-vitro reaction ends in the diferric state. The reactions using the same concentrations of NH_2-CAM and NH(OH)-CAM give the same results but the reformation of **P** in the case of the latter substrate is masked due to the rates of the decay and re-formation reactions. Buffer: 50 mM Bicine, pH 9, 4 °C.

Exchange of NO-CAM from the CmlI Active Site. In order to test whether NO-CAM can leave and reenter the active site during the reaction cycle, $^{18}O_2$-**P** was degassed to remove excess O_2, and equilibrated in an anaerobic chamber before 1 equiv. NH_2-CAM was added. After a 20 s incubation, 1 equiv. $N^{16}O$-CAM was added. The sample was then quickly put under an $^{18}O_2$ headspace and allowed to react for 10 min. Samples were acid quenched and analyzed by LCMS. Control samples were made by adding buffer instead of NO-CAM. If the NO-CAM made during the reaction cannot leave the active site, then only CAM containing ^{18}O in the nitro group should

be made. If, however, NO-CAM can leave and subsequently re-bind in the active site after ^{16}O-P has formed, then there should be some CAM formed with both ^{18}O and ^{16}O in the nitro group. As shown in Figure 3-11 and Table 3-3, approximately 20% more ^{16}O,^{18}O CAM is formed compared to the control, suggesting that at least 20% of the NO-CAM dissociates during the course of the experiment. Unfortunately, the short lifetime of the NH(OH)-CAM intermediate prevented a similar evaluation of dissociation from the active site.

Table 3-3: Exchange of NO-CAM from the CmlI active site during single turnover[a]

isotopic composition in CAM nitro group	**$^{18}O_2$-P + NH_2-CAM %**	**$^{18}O_2$-P + NH_2-CAM followed by $N^{16}O$-CAM %**
^{16}O, ^{16}O	2 ± 1	5 ± 3
^{16}O, ^{18}O	13 ± 2	28 ± 3
^{18}O, ^{18}O	85 ± 4	66 ± 6

[a]Reaction performed with one equivalent of each substrate as described in the text.

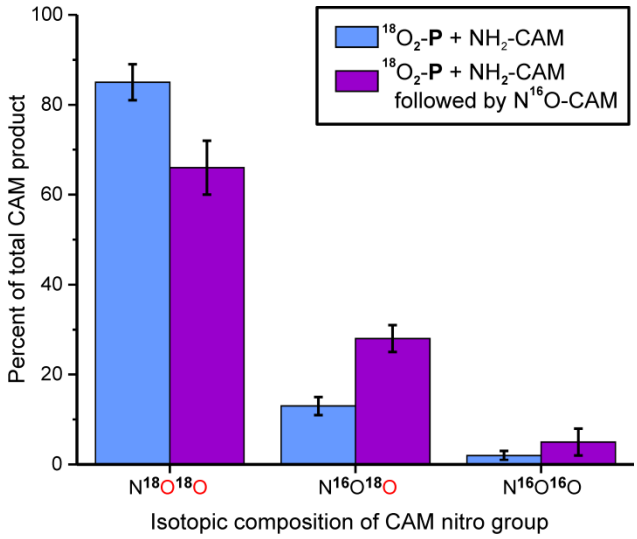

Figure 3-11: NO-CAM exchange test. Reaction of 200 μM of NH_2-CAM with 200 μM $^{18}O_2$-P, followed 20 s later by addition of buffer or NO-CAM under an $^{18}O_2$ atmosphere. Presence of mixed labeled CAM in the reaction in which NO-CAM was added shows that NO-CAM can exchange from the active site given a 20 s incubation period. Buffer: 50 mM Bicine, pH 9, 4 °C.

Discussion

Summary of Findings. It is shown here that the CmlI reaction cycle intermediate **P** reacts with the native substrate NH_2-CAM as well as the reaction pathway intermediates NH(OH)-CAM and NO-CAM to yield CAM. Moreover, NH(OH)-CAM is found to reduce $CmlI^{ox}$ to yield $CmlI^{red}$, which can subsequently form **P** in the presence of O_2. These observations provide the basis for the new single turnover mechanistic cycle shown in Scheme 3-6 in which re-reduction of $CmlI^{ox}$ by NH(OH)-CAM, formed during the reaction of **P** with NH_2-CAM, allows formation of CAM with the input of only two non-substrate-derived electrons (supplied *in vivo* by an as yet unidentified reductase). This cycle is conceptually similar to a recent model proposed for AurF.[85] However, it differs in both the pathway intermediate that serves as the reductant and the state of the enzyme diiron cluster at the conclusion of a single turnover cycle. The mechanistic significance of these observations will be discussed here.

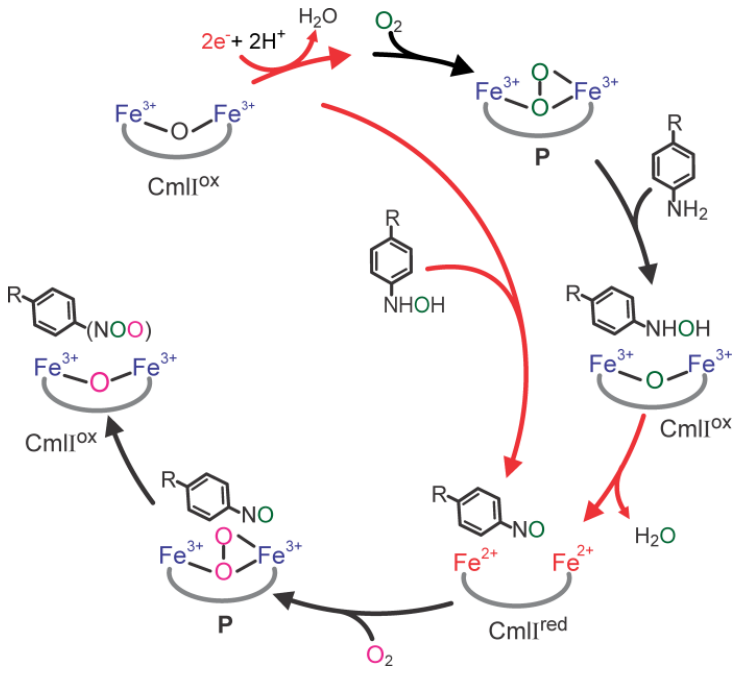

Scheme 3-6: Proposed single turnover reaction pathway of CmlI. Reduction steps are shown in red.

Comparison to a Model Requiring Three Successive Reactions with P. As shown in Scheme 2, pathway I, the original model for the 6-electron oxidation of NH_2-Ar substrates envisioned three similar successive oxidation reactions, each utilizing a **P**-like intermediate (or a

high valent species derived from it). This model was supported by the observation that a titration of **P** with NH_2-CAM, or the equivalent titration for the AurF system, had approximately a 3:1 stoichiometry.[52-53, 76, 83] The current results show that the reaction of NH(OH)-CAM with either $CmlI^{ox}$ or **P** approaches 1:1 stoichiometry and yields CAM as the major product. These results suggest that the original mechanistic proposal is not correct and that at least one step of the reaction involves oxidation of a pathway intermediate coupled to reduction of $CmlI^{ox}$.

Based on the stepwise study of the reaction shown in Figure 3-8, the reaction of NH_2-CAM with **P** (i.e. $CmlI^{red}$ + O_2) to produce CAM also proceeds by utilizing a pathway intermediate to re-reduce the diiron cluster. The reductive pathway intermediate is again NH(OH)-CAM. However, the overall yield of CAM from this reaction is typically 33% or less, due presumably to uncoupling. We believe that this fortuitous fractional loss of yield led to the observed roughly 3:1 **P** to NH_2-CAM ratio that supported the original mechanistic proposal.

Comparison of the Mechanistic Models Employing a Pathway Intermediate as an Electron Source. The observation by Bollinger, Krebs, and coworkers that the reaction of NH(OH)-Ar with the AurF-peroxo intermediate led to NO_2-Ar product plus diferrous AurF under anaerobic conditions initiated a new way to think about the amine oxygenase chemistry. [85] It was proposed that $N(OH)_2$-Ar is formed as an intermediate and then acts as the reducing agent for diferric AurF as it itself is oxidized to NO_2-Ar. However, despite the structural similarity and common reaction type of AurF and CmlI, we do not believe that CmlI follows this mechanistic pathway during its native cycle. Scheme 3-7, pathways II and III, respectively, compare an AurF-type mechanism to that proposed here for CmlI for CAM formation. We believe that pathway III better describes the native reaction for CmlI for five reasons: (1) NH(OH)-CAM is shown to act as an efficient reducing agent for $CmlI^{ox}$, and it is the consensus first intermediate in both pathways II and III. (2) In general, hydroxylamines are efficient reducing agents for iron. The reduction of ferric to ferrous ion is well documented in the organic synthetic literature, and it is an essential step of colorimetric assays to determine iron concentration. [151, 153-154] In contrast, $N(OH)_2$-Ar is more likely to hydrolyze quickly to the NO-CAM intermediate rather than act as a reducing agent. (3) The single turnover reaction of stoichiometric NH_2-CAM and **P** proceeds through NO-CAM, and NO-CAM is independently shown to react with **P** to form CAM. (4) After a single turnover of sub-stoichiometric NH_2-CAM and **P** under aerobic conditions, $CmlI^{ox}$ rather than $CmlI^{red}$ or **P** is observed. This requires that the pathway reducing agent not act in the

final step of the pathway because doing so would generate a reduced diiron cluster after the final step. (5) As shown in Scheme 3-7, a single turnover reaction of ^{18}O-**P** in an $^{16}O_2$ atmosphere and $H_2{}^{16}O$ would be expected to give mixed-labeled product by pathway III but not by pathway II. Mixed-labeled CAM product was, in fact, observed for the CmlI reaction (Table 1).

Although this data set strongly supports the reaction pictured in Scheme 3-6 and Scheme 3-7, pathway III as the best fit for the CmlI cycle, it also reveals the complexity of the reaction. For example, in the reaction of NH_2-CAM with ^{18}O-P in an $^{16}O_2$ atmosphere and $H_2{}^{16}O$, doubly ^{18}O-labled product was observed in addition to the mixed-labeled CAM product predicted by Scheme 3-7, pathway III. Two ways in which this might come about are: (1) partial dissociation of NO-CAM and subsequent reaction with unreacted ^{18}O-**P**, or (2) partial dissociation of NH(OH)-CAM and subsequent reaction with ^{18}O-**P** through pathway II. We view the latter possibility as unlikely because CmlI^{ox} and NH(OH)-CAM are formed simultaneously in the active site where the observed redox reaction to form Cml^{red} and NO-CAM would be expected to occur efficiently. Approximately 50% of the NH(OH)-CAM would have to dissociate and react through pathway II in order to account for the amount of mixed-label CAM observed. However, very little CAM and no NH(OH)-CAM are observed in the stepwise reaction of NH_2-CAM with **P** illustrated in Figure 3-8 prior to addition of O_2. In contrast, generation of mixed-label CAM via the partial dissociation of NO-CAM is possible based on the exchange experiment illustrated in Figure 8. It is possible that these alternative pathways as well as the lower that stoichiometric yields in some cases described above result from performing the reaction under single turnover conditions without the native reductant. Indeed, protein interactions are very important throughout the diiron oxygenase family but cannot be explored in the current case because the native reductase has not been identified for any amine oxygenase.[155-157]

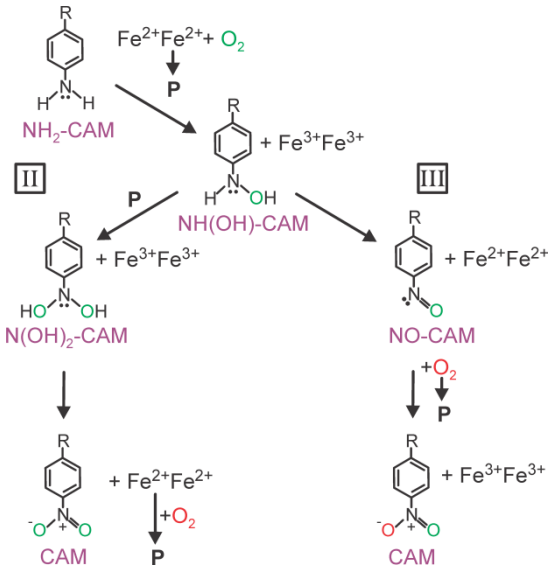

Scheme 3-7: Comparison of oxygen incorporation into CAM via different pathways.

Although pathway III better describes the native CmlI pathway, the off-cycle or artificial reaction of **P** with NH(OH)-CAM was carried out to make a direct comparison to the analogous reaction in the AurF cycle. In accord with the results reported for the anaerobic reaction of the AurF-peroxo intermediate reaction with NH(OH)-Ar,[85] we find that $CmlI^{red}$ and CAM are produced when **P** is reacted with NH(OH)-CAM. This reaction would not be on-pathway for Scheme 3-7, pathway III, as only $CmlI^{ox}$ and NH(OH)-CAM are found together in the active site, thereby allowing the redox reaction to occur. Consequently, the off-pathway reaction for CmlI might occur as proposed for AurF (Scheme 3-7, pathway II). However, the subsequent addition of O_2 was found to yield additional CAM and CmlI finishes in the mostly oxidized rather than reduced or **P** states expected based on the reported AurF reaction. [85] Additional kinetic and spectroscopic studies will be required to fully characterize the off-pathway reaction of **P** with NH(OH)-CAM.

Mechanistic Significance. The reactivity of the various activated forms of O_2 created by diiron clusters is of great current interest.[158-159] In the past, there has been significant focus on the high-valent species that can transfer oxygen into very stable C-H bonds, such as in the reaction of sMMOH compound **Q** with methane.[8, 31, 91] The potential reactivity of peroxo or superoxo intermediates has, by contrast, come to light only recently.[93, 159-160] The activity, novel structure, and long lifetime of the CmlI peroxo intermediate **P** offer an opportunity to explore new aspects

of the formation and reaction of peroxo species in diiron-cluster containing enzymes. Indeed, we find that **P**, proposed to have a μ-$\eta^1\eta^2$ peroxo core,[52] is quite reactive with both aromatic amine and aromatic nitroso substrates. The $^{18}O_2$ incorporation studies reported here show that both of the nitro oxygens in the final product derive from O_2, but it is clear that they are added in a stepwise fashion from different O_2 molecules (via two successively formed **P** intermediates), because a mixed-isotope product is obtained when ^{18}O-**P** is reacted with NH_2-CAM in an ^{16}O atmosphere. Thus, CmlI is a monooxygenase where the reactive oxygen species is formed prior to O-O bond cleavage, quite distinct from the high-valent strategy used by sMMOH-type diiron monooxygenases.[8] The use of a diferric peroxo species may allow the enzyme to catalyze a wide range of N-oxygenation reactions. Over the course of the amine to nitro conversion, the substrate becomes increasingly electron deficient. Thus **P** must be ambiphilic, able to shift from acting as an electrophilic species for the oxygenation of NH_2-CAM to a more nucleophilic oxidant for oxygenation of NO-CAM. It is significant that, despite the monooxygenase reactivity of CmlI, it cannot oxygenate C-H bonds of aromatic or aliphatic hydrocarbons.[52] While this may be attributed to several causes including the relative bond stability of these substrates, it may also reflect the unique structure of the CmlI **P** intermediate and its environment. For example, this environment may restrict access to the protons thought to play a role in the generation of the high-valent oxo or bis μ-oxo intermediates of hydrocarbon monooxygenases.[33, 91]

Conclusions

Aromatic amine oxygenation deviates from the paradigm of diiron oxygenation chemistry in several ways. While cluster reduction and formation of a peroxo intermediate is shared among oxygen-activating diiron oxygenases, the structure of the peroxo intermediate **P** of the CmlI aromatic amine oxygenase is unique.[52] This specialized peroxo intermediate is highly reactive with NH_2-CAM and the other amine oxidation pathway intermediates, while the peroxo intermediates of other oxygenases serve primarily as unreactive stepping stones to reactive high valent intermediates. Another remarkable aspect of the diiron cluster of the aromatic amine oxygenases CmlI and AurF is their ability to use intermediate products as mid-pathway diiron cluster reductants in place of the reductase used by all other diiron oxygenases. This means that a 6-electron oxidation of the NH_2-Ar substrate could occur without dissociation of the intermediate products, thereby avoiding release of hydroxylamino- and nitroso-intermediates that might be

damaging to the cell. While the results presented here show that dissociation is possible at the NO-Ar stage, the time scale for release versus the rate of normal catalysis appears to be slow. The versatility of the **P** intermediate allows it to react with intermediate products that it would not normally encounter in the native pathway to CAM formation. In particular, the **P** reaction with NH(OH)-CAM would not normally occur because they are not present at the same time in the cycle. Nevertheless, this reaction can occur with high efficiency when these reactants are separately prepared and mixed, and it leads to the same CAM product, albeit through an alternative reaction pathway.

Acknowledgements

I would like to thank Dr. Brent Rivard for his invaluable contributions to this project as a collaborator. Dr. Rivard spent innumerable hours helping design and run complex experiments, optimizing HPLC procedures, synthesizing CmlI substrates, and providing a soundboard. The Mossbauer samples were run and analyzed by Ruixi Fan and Dr. Yisong (Alex) Guo at the Carnegie Mellon University department of chemistry. Dr. Joseph Dalluge assisted with mass spectral analysis.

Chapter 4

Kinetic Characterization of P Formation and the CmlI Mechanism

Introduction

Diiron-cofactor-containing aryl-amine oxygenases are unusual in that they catalyze a six-electron substrate oxidation using an oxidant that can transfer, at most, two electrons at a time. Initial hypotheses suggested a logical mechanism in which the two-electron oxidant was formed thrice in an identical manner, requiring the injection of six external electrons in order to generate the activated form of oxygen that serves as the oxidant.[75, 83] Recent work has provided evidence for a second, more efficient, mechanism that requires the injection of only two exogenous electrons.[85, 161] One iteration of this mechanism has been described for the diiron cluster N-oxygenase CmlI, and proceeds as follows (Figure 4-1): the diiron cluster accepts two electrons and binds O_2 to form a diferric peroxo species (**P**) that oxygenates the aryl-amine substrate to an aryl-hydroxylamine substrate. **P** is converted to a diferric resting state after performing this oxygenation. The hydroxylamine substrate then reduces the diferric cluster to a diferrous state, priming it to re-form **P** upon the addition of O_2. The aryl-hydroxylamine substrate is itself oxidized to the nitroso intermediate. Finally, the second **P** species oxygenates the aryl-nitroso intermediate to the aryl-nitro final product. The only exogenous electrons required are those to convert the resting state diferric CmlI to diferrous, so that **P** can be formed to initiate the oxidation of another substrate molecule.

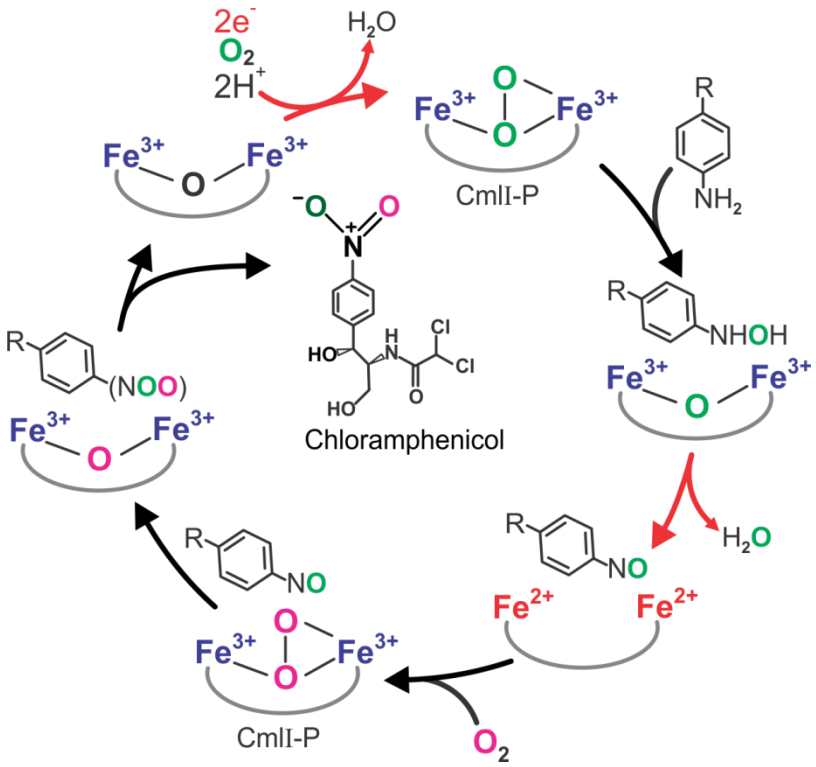

Figure 4-1: Proposed mechanistic cycle for N-oxygenation by CmlI. Reduction steps are shown with red arrows. Color coding of the oxygen atoms highlights the fact that oxygen atoms from two different O_2 molecules are incorporated into the final product.

The proposed intermediates on this cycle, both enzyme- and substrate-based, have been trapped and characterized by spectroscopic and analytical methods. Much of the previous work was done by analyzing intermediates with a freeze-frame approach, artificially pausing the reaction at different points, or by analyzing products at the end of the reaction cycle. We would like to verify the proposed reaction cycle in real time using transient kinetic analysis.

In this work, the kinetic constants describing various steps of the proposed CmlI single turnover reaction are described. The experimental approach was to isolate steps of the reaction cycle as much as possible in order to minimize the number of processes monitored at one time. Kinetic constants and trends were measured for individual steps of the cycle and compared to those of the overall cycle. An encompassing kinetic mechanism was constructed using rate constants derived from the experimental data and from simulations of the experimental data. This approach allowed assessment of the model proposed by the mechanism in which the aryl-hydroxylamine serves as the reducing agent, as well as reveals new aspects of the enzyme cycle and its regulation.

Results

Kinetic Parameters of P Formation. The diferric peroxo species of CmlI (**P**) forms within seconds when chemically reduced diferrous CmlI ($CmlI^{red}$) is combined with O_2. **P** is highly stable in the absence of substrate, exhibiting a $t_{1/2} \sim 3$ h at 4 °C and pH 9, and thus the formation reaction is expected to be irreversible. To determine the rate constant(s) for **P** formation, anaerobic $CmlI^{red}$ was mixed with 5-36 equivalents of O_2 on a stopped-flow UV-vis instrument. The formation of **P** was followed at 300 nm, the wavelength where optical changes due to **P** formation are maximized. The resulting traces are best fit by a three summed exponential expression (Figure 4-2 and Table 4-1) (complete description of analysis of transient kinetic data is found in Chapter 5, "Trace Fitting and Rate Constant Determination.") Plotting the reciprocal relaxations times (RRTs) versus O_2 concentration shows that all three phases have a linear dependence on O_2 concentration (Figure 4-3). The magnitude of the total amplitude change stays the same over the range of O_2 concentrations tested, and the three observed phases are approximately equal in amplitude. The contribution of phase three to the total change in amplitude increases from 30% to 50% over the range of O_2 concentrations, while the first and second phase decrease equally and accordingly. This may be due to the fact that the third phase makes an increasing contribution to the portion of the time course observed as the O_2 concentration increases, thereby increasing the accuracy of the RRT values obtained.

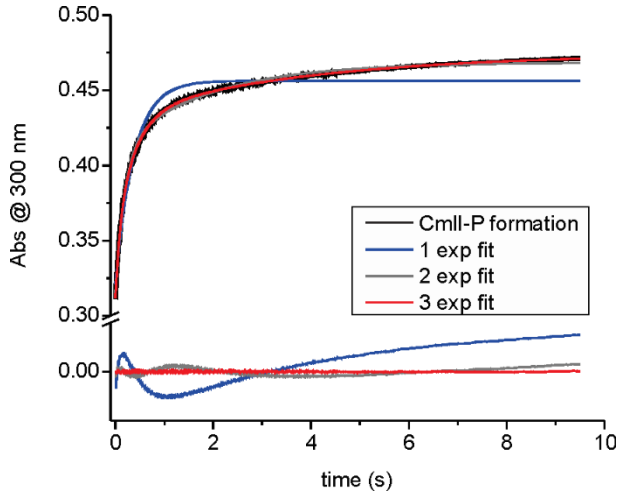

Figure 4-2: Optical changes correlated with the formation of species **P**. Single- (blue), double- (gray), and triple- (red) exponential fits of the **P** formation process shown by the black trace. Fit residuals are shown below the trace and highlight the need for a three exponential fit. 50 mM Bicine pH 9, 4 °C.

The presence of three phases linearly dependent on substrate is most easily accounted for by three parallel reactions to form **P**, rather than a single **P** formation process that employs three consecutive steps. Presently, we do not have evidence for more than one form of **P** and the Mössbauer spectrum of **P** shows only one type of cluster.[52] If there are more forms of **P** that are not distinguishable by Mössbauer, they all appear to react rapidly with substrates, exhibiting the same rate constant (see below). The multiple phase **P** formation behavior is likely to be the result of either or both of the following scenarios: (a) three different pathways for O_2 to bind that all lead to the same **P,** or (b) $CmlI^{red}$ exists in three different structural or protonation states that differentially affect **P** formation. Plots of all phases have a y-intercept close to zero, showing that the formation of **P** in the absence of substrate is nearly irreversible, as expected. This finding is also in accord with our previous demonstration that **P** does not exchange with head space O_2 over the course of hours.[161]

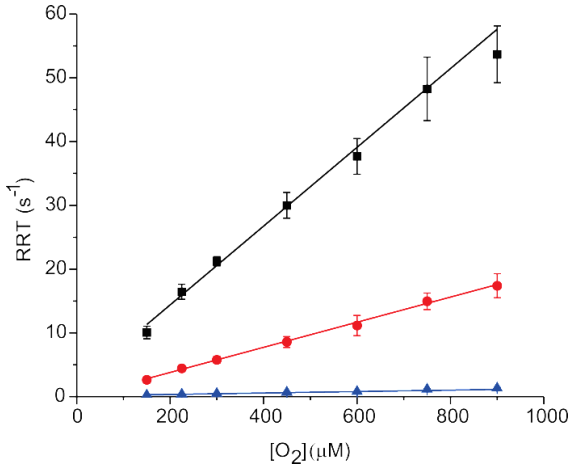

Figure 4-3: O_2 dependence of **P** formation. 40 μM $CmlI^{red}$ (final, post mix concentration) was mixed in a 1:1 ratio with varying concentrations of O_2 in buffer. RRT-1, -2, and -3 from multiexponential fitting of stopped-flow traces was plotted versus O_2 concentration, all showing linear relationships. The second order rate constant (k_1) for each process was determined from the slope of the linear fit to the data (solid line) and reported in Table 4-1. Reported error of each point is one standard deviation from the mean. 50 mM Bicine pH 9, 4 °C.

Table 4-1: Rate constants and amplitudes for P formation.

Phase	k_1 **(s^{-1} mM^{-1})**		**Amplitude (%)**			
		Eqv. O_2	7	14	18	28
1	58.1 ± 2.0		30	30	25	25
2	19. 6 ± 0.4		40	30	35	25
3	1.4 ± 0.1		30	40	40	50

Kinetic Parameters of P Formation with CAM Present. We hypothesized that the presence of a substrate might "streamline" the **P** formation to a single process by favoring one form of CmlI^{red}. To simulate this reaction without using substrate, and thereby avoid complicating the kinetic traces with substrate-mediated decay, **P** was formed in the presence of the product CAM. The reaction of CmlI^{red} with a ten-fold excess of CAM and 3-30 equivalents of O_2 results in the formation of a **P** species with comparable stability to that formed in the absence of CAM. This process was followed at 320 nm to avoid the significant absorbance of CAM at 300 nm.

The resultant kinetic traces for **P** formation are fit best by a two-summed, rather than a three-summed, exponential expression (Figure 4-4A). When the two RRTs are plotted versus O_2 concentration, the best fits are by linear equations, as in the case without CAM (Figure 4-4B, C). The observation of only two phases suggests that there are only two ways to make **P** when a substrate-like molecule is present. The second order rate constants for **P** formation in the presence of CAM are listed in Table 4-2. The non-zero y-intercepts may be a result of experimental error or may be an indication that O_2 binding is reversible in the presence of a substrate-like molecule. Because the concentration dependence of the kinetic parameters for O_2 binding to form **P** changes dramatically when pseudo-first-order concentrations of CAM are present, it is likely that CAM binds before O_2 under these conditions. These observations provide a clear indication that binding of product, and presumably substrate, has a significant effect on the **P** formation process.

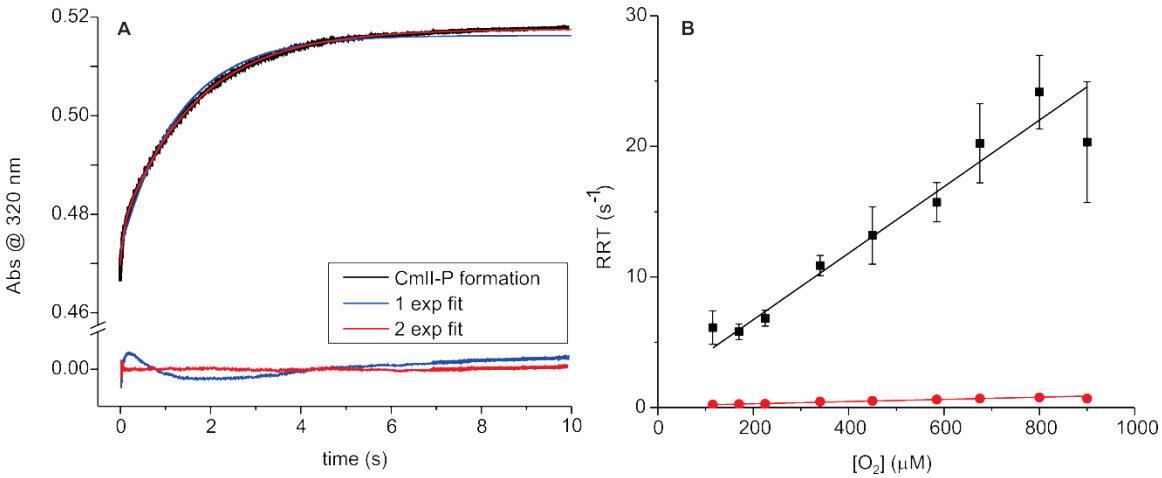

Figure 4-4: P formation in the presence of the product CAM. 40 μM CmlI^{red} (final, post mix concentration) was mixed in a 1:1 ratio with varying concentrations of O_2 in buffer containing 400 μM CAM. A: **P** formation time course fits best to a two exponential equation (red trace), as shown by the fit and residuals. B: RRT-1 (black) and -2 (red) from multiexponential fitting of stopped-flow traces were plotted versus O_2 concentration, both showing linear relationships. The extracted rate constants are found in Table 4-2. Reported error of each point is one standard deviation from the mean. 50 mM Bicine pH 9, 4 °C.

Table 4-2: Rate constants for P formation with CAM present.

Phase	k_f (s^{-1} mM^{-1})	k_r (s^{-1})
1	25.5 ± 2	1.6 ± 0.6
2	0.8 ± 0.06	0.1 ± 0.02

Kinetic Parameters of the Reaction of P with NH_2-CAM. After **P** formation, the next step of the CmlI cycle that can be isolated is the reaction of **P** with NH_2-CAM to form NH(OH)-CAM and $CmlI^{ox}$, followed by oxidation of NH(OH)-CAM to NO-CAM and reduction of the diferric cluster to form $CmlI^{red}$. **P** was formed with 0.9 equivalent of O_2 (to ensure no excess O_2 in the reaction) and then loaded immediately on the stopped-flow instrument for reaction with 5-40 equivalents of NH_2-CAM dissolved in anaerobic buffer. Since **P** formation in the absence of substrate is nearly irreversible (see Figure 4-2), the kinetics of the reaction with substrate are simplified. When monitored at 480 nm, both **P** decay and the subsequent reduction of the diiron cluster appear as a decrease in absorbance. Both processes are first order or pseudo-first order, and the reaction halts after the last step, so summed exponential fitting is appropriate.

The time courses are fit well by a two-summed exponential expression (Figure 4-6). Both exponentials have positive amplitudes (a positive amplitude sign correlates with decreasing absorbance), and the phase with larger RRTs contributes ~85% of the total absorbance change. Since the reactions involved are quasi-irreversible, and the phases differ substantially in RRT, it is possible to assign the two RRTs to rate constants for two steps of the reaction. It would be convenient to assign one phase and its RRT to the conversion of **P** to $CmlI^{ox}$, and the second to the reduction of $CmlI^{ox}$ to $CmlI^{red}$, but analysis of the absorbance changes invalidates this assignment.

The extinction coefficients for CmlI-P, $CmlI^{ox}$, and $CmlI^{red}$ at 480 nm (Table 4-3) were used to calculate the expected absorbance of those species in this reaction based on the known CmlI concentration. There is negligible absorption due to any of the organic CAM substrates at 480 nm. The starting species, 10% $CmlI^{red}$ and 90% **P**, has Abs = 0.11. A spectrum of 90% $CmlI^{ox}$/10% $CmlI^{red}$ would give Abs = 0.072 and a pure $CmlI^{red}$ spectrum would give Abs = 0.046. The extrapolated **P** decay ends at ~0.053, indicating that the final species is a mixture of 38% $CmlI^{ox}$ and 62% $CmlI^{red}$ (Figure 4-5). Accounting for a maximum of 10% **P** decay over the course of the experiment would shift those percentages by up to 10%, so the mixture in the absence of **P** auto decay is expected to be 28% $CmlI^{ox}$ and 72% $CmlI^{red}$. This amount of reduction is consistent with that seen by Mössbauer when the same reaction was done under similar

conditions.[161] The two steps (**P** to CmlI^{ox}, CmlI^{ox} to CmlI^{red}) should be approximately equal in the absorbance change they each contribute, thus the phase with 85% of the absorbance change must refer to more than one step.

Table 4-3: Extinction coefficients for CmlI-P, CmlI^{ox} and CmlI^{red} at four wavelengths.

CmlI Species	Extinction coefficient (cm^{-1} M^{-1})			
	300 nm	390 nm	480 nm	500 nm
CmlI^{red}	8000	520	230	190
CmlI^{ox}	11,000	1300	375	300
P	12,000	1350	580	500

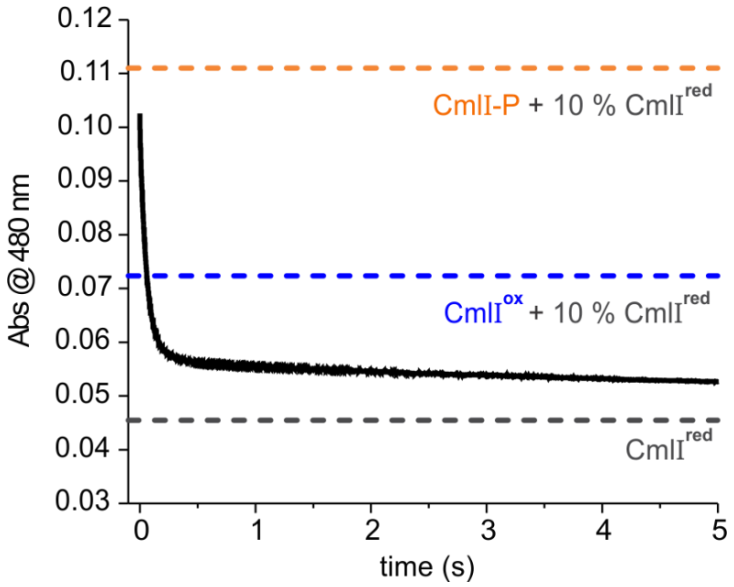

Figure 4-5: Reaction of a ten-fold excess of NH_2-CAM with 200 µM **P**, showing **P** decay. Dashed lines indicate the calculated absorbance of 180 µM **P** + 20 µM CmlI^{red}, 180 µM CmlI^{ox} + 20 µM CmlI^{red}, and 200 µM CmlI^{red}.

One interpretation is that there are two reduction processes starting from two different CmlI^{ox}. The first reduction is quite fast, and thus the rate constant is averaged into the rate constant observed for the **P** to CmlI^{ox}, and so the dominant phase is reflective of both **P** decay and the fast reduction. The second phase would then describe a slow reduction with k_f = 1 s^{-1} mM^{-1}. The observation of more than one form of CmlI^{ox} by Mössbauer supports the two reduction mechanism hypothesis, modeled in Scheme 4-1 **I**.[52] Another interpretation is that a portion of the

NH(OH)-CAM dissociates and rebinds relatively slowly before performing the reduction, giving the slow reduction rate (Scheme 4-1 **II**). The rate for NH(OH)-CAM dissociation from E^{ox} has not been independently determined but must be > 1 s^{-1} to account for the proposed flux from the active site. The assignment of the slower phase as a reduction reaction is consistent with the observed rate constants in the reaction of NH(OH)-CAM and $CmlI^{ox}$ described in the next section.

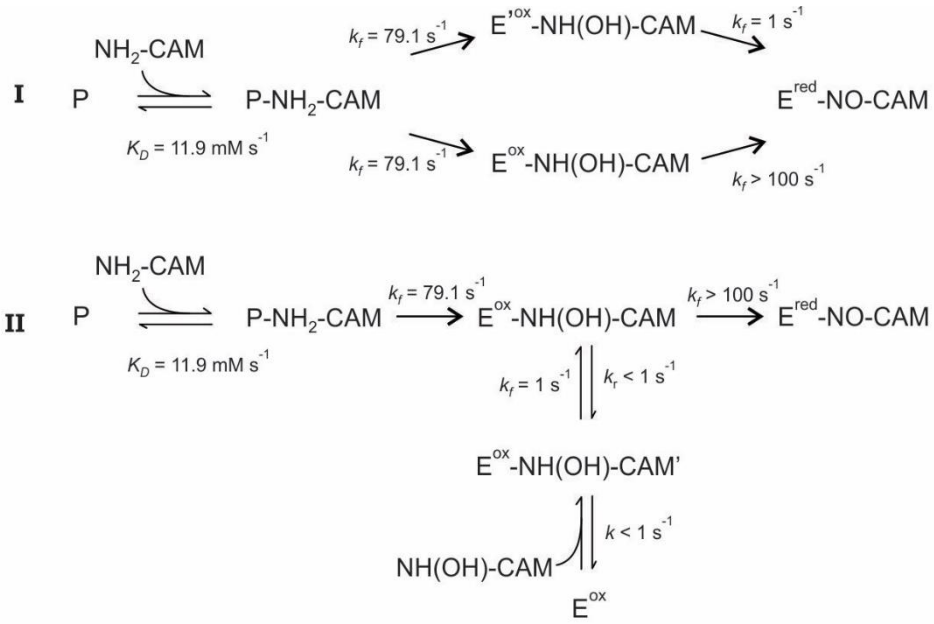

Scheme 4-1: Proposed schemes for the reaction of **P** with NH_2-CAM. Rate constants are derived from the plots in Figure 4-7. For simplicity $CmlI^{ox}$ and $CmlI^{red}$ are abbreviated as E^{ox} and E^{red}, respectively.

RRTs from each exponential were plotted versus [NH_2-CAM] to give hyperbolic fits (Figure 4-7). If, as argued above, the faster phase is correlated with the **P** to $CmlI^{ox}$ conversion followed by a comparably fast conversion of $CmlI^{ox}$ to $CmlI^{red}$, the hyperbolic curve suggests that a fast second-order process precedes **P** decay, presumably NH_2-CAM binding. Consequently, the observed concentration-dependent fast phase is closely correlated with the step in which **P** reacts with NH_2-CAM. It has rate constants of k_f = 79.1 ± 6 s^{-1} and k_r = 3.9 ± 0.2 s^{-1}. It is unlikely that this step is actually reversible, given that it involves the cleavage of an O-O bond and insertion of an O atom into a N-H bond. The apparent K_D of the hyperbolic curve gives K_D for the NH_2-CAM binding to **P**, K_D = 11.9 ± 1.7 mM. This third step has rate constants of k_f = 0.9 ± 0.1 s^{-1} and $k_r \approx$ 0, based on a hyperbolic fit of the RRT concentration dependence (Figure 4-9 B).

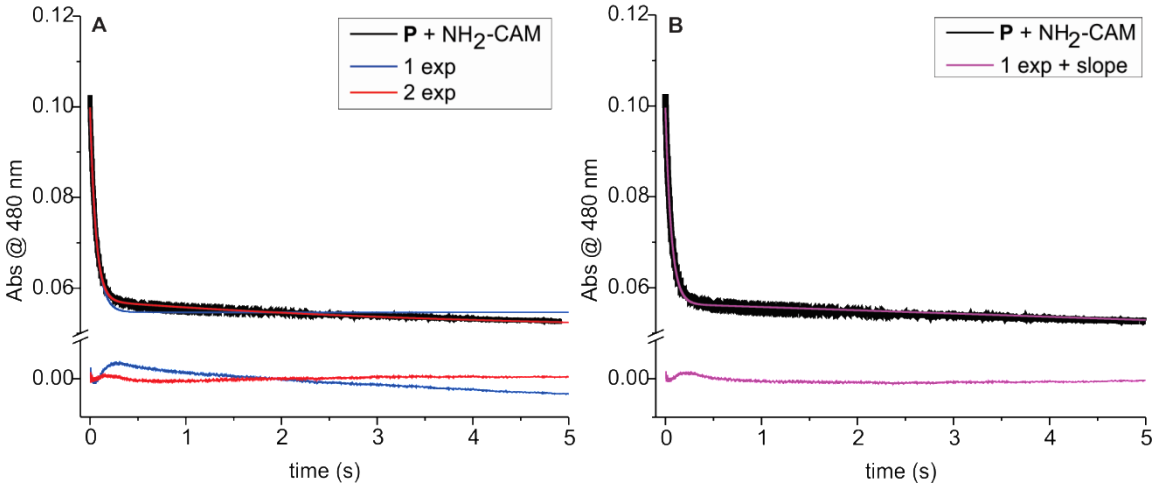

Figure 4-6: Optical changes at 480 nm correlated with the reaction of 200 µM **P** with 2 mM NH_2-CAM. A, single- (blue trace) and double- (red trace) exponential fits of the substrate-mediated **P** decay process are shown by the black trace. Fit residuals are shown below the trace and highlight the need for a two-exponential fit. B, fit with a single exponential plus slope. 50 mM Bicine pH 9, 4 °C.

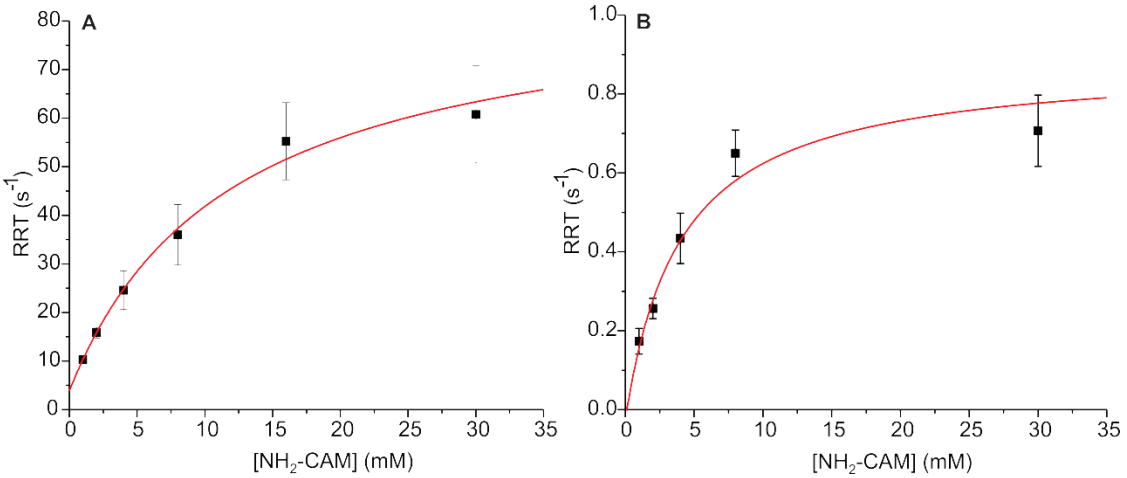

Figure 4-7: NH_2-CAM concentration dependence of the RRTs for the reaction of **P** with NH_2-CAM. Extracted RRTs plotted versus [NH_2-CAM] for the reaction of **P** (200 µM, final post-mix concentration) with varying concentrations of NH_2-CAM in anaerobic buffer. A: RRT-1, hyperbolic fit gives K_D = 11.9 ± 1.7 mM, k_f = 79.1 ± 6 s^{-1}, and k_r = 3.9 ± 0.2 s^{-1}. B: RRT-2, hyperbolic fit gives k_f = 0.9 ± 0.1 s^{-1}, k_r = -0.02 ± 0.12 (≈ 0) s^{-1}, K_D = 4.0 ± 2.7 mM^{-1}. 50 mM Bicine pH 9, 4 °C.

Kinetic Parameters of the Reaction of CmlI^{ox} with NH(OH)-CAM. The reaction of CmlI^{ox} by NH(OH)-CAM can also be monitored by simply mixing these two reactants anaerobically. Careful scrubbing of O_2 from the reaction buffers and the stopped-flow instrument ensures that the reaction stops after the reduction process and does not proceed to re-form **P** for the final oxidation step. In these reactions, CmlI^{ox} was made anaerobic and then mixed in a 1:1 ratio with anaerobic buffer containing varying concentrations of NH(OH)-CAM, all of which

were appropriate to establish pseudo first order conditions. The resulting optical change at 390 nm was a decrease in absorbance; the trace fit to a double exponential equation (Figure 4-8). The monitoring wavelength was chosen to maximize optical change while minimizing the contribution of the NH(OH)-CAM that occurs at lower wavelengths. The net absorbance change is ~0.03, which matches the expected absorbance change for the conversion of 40 µM $CmlI^{ox}$ to $CmlI^{red}$.

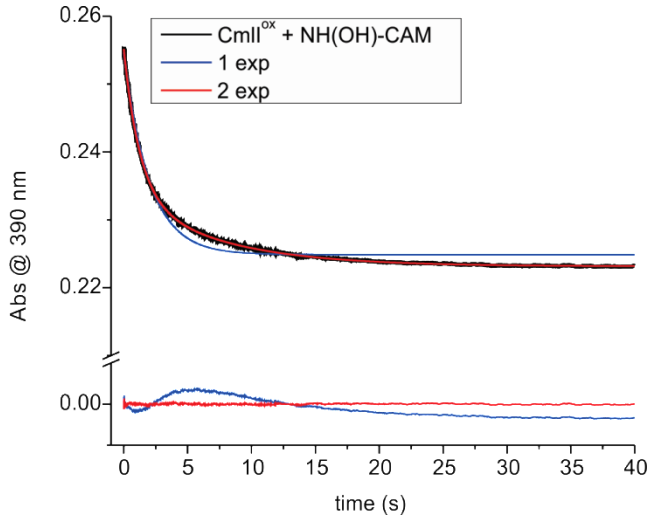

Figure 4-8: Optical change at 390 nm upon the anaerobic mix of 40 µM $CmlI^{ox}$ and 2 mM NH(OH)-CAM (final, post-mix concentrations). The trace fits best to a two exponential equation, as shown by the colored fit lines and the residuals for 1- (blue) and 2- (red) exponential fits shown below the trace. 50 mM Bicine pH 9, 4 °C.

The plots of RRT-1 and RRT-2 versus NH(OH)-CAM concentration are both hyperbolic (Figure 4-9 A and B), suggesting that a relatively fast step, possibly NH(OH)-CAM binding, precedes the CmlI reduction occurring in the observable steps. The rate constants extracted from these plots are all very slow compared with the rate of reduction of the diiron cluster observed when starting the reaction with NH_2-CAM as described above (RRT-1: $k_f = 1.3 \pm 0.1\ s^{-1}$ and $k_r = 0$ and RRT-2: $k_f = 0.2 \pm 0.03\ s^{-1}$, $k_r \approx 0$). The slower phase disappears at high concentration of NH(OH)-CAM (Figure 4-9 C). The K_D values for NH(OH)-CAM binding (RRT-1: 1.1 ± 0.05 mM, RRT-2: 1.2 ± 0.3 mM) for the plots are approximately equal and indicate higher affinity that **P** exhibits for NH_2-CAM. The similar K_D values suggests that the two phases describe parallel, not sequential, processes, which seems likely given that both result in reduction of $CmlI^{ox}$. The disappearance of one phase at high substrate concentrations indicates a more complex interaction

with NH(OH)-CAM than simple binding in the active site. For instance, binding at a secondary site might cause a conformational change that affects the reduction rate constant.

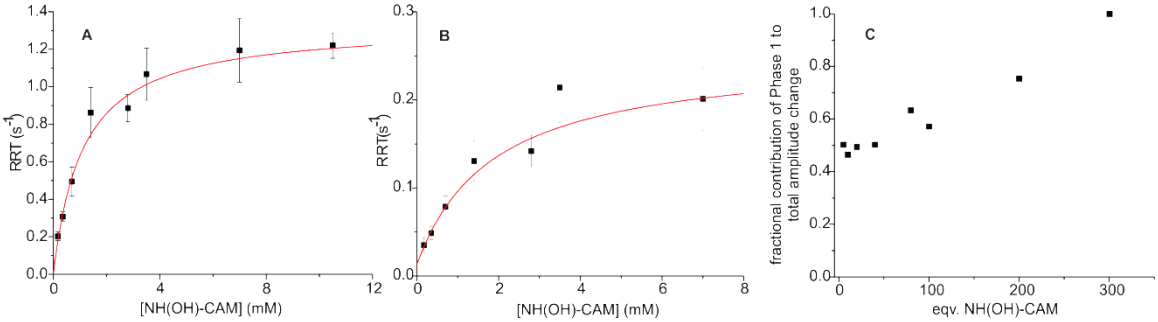

Figure 4-9: NH(OH)-CAM concentration dependence of the RRTs for the reaction of 40 µM CmlI^{ox} (final, post mix-concentration) and varying concentrations of NH(OH)-CAM in anaerobic buffer. A: Hyperbolic fits of RRT-1s extracted from the traces of the reaction, giving K_D = 1.1 ± 0.05 mM and k_f = 1.3 ± 0.1 s^{-1}. B: Hyperbolic fits of RRT-2s extracted from the traces of the reaction, giving K_D = 1.2 ± 0.3 mM and k_f = 0.23 ± 0.03 s^{-1}. C: Plot of the fractional contribution of RRT-1 to the total amplitude change, showing that at high [NH(OH)-CAM], RRT-1 becomes increasingly dominant until it is responsible for 100% of the amplitude change at 11 mM/ 300 equivalents of NH(OH)-CAM. 50 mM Bicine pH 9, 4 °C.

The rate constant extracted from the asymptotic maximum of the plot of the faster phase RRT (k_f ~ 1 s^{-1}) is similar to that of the difficult to assign slowest phase of the **P** reaction NH_2-CAM, as are the K_D values, within error (K_D = 1.2 ± 0.3 mM^{-1} vs. K_D = 4.0 ± 2.7 mM^{-1}), supporting the hypothesis that these are the same process and represent CmlI^{ox} reduction. However, the slow rate constant in each case is not consistent with the overall flux in the CAM biosynthetic pathway (see below), suggesting that there is a difference between the process of reduction when NH(OH)-CAM is generated adjacent to the diferrous cluster in the active site by **P** reaction with NH_2-CAM and when NH(OH)-CAM is added from solution. Indeed, the slowest rate constant in the reaction of **P** with CmlI^{ox} may represent the case in which NH(OH)-CAM escapes the active site before reduction can occur, forcing it to rebind to complete the process. Presumably, the rebinding and subsequent reduction would proceed with the kinetics observed here for the reaction of NH(OH)-CAM in solution with CmlI^{ox}.

Reaction of P with NO-CAM. Anaerobic **P** was formed as described above and mixed with NO-CAM dissolved in anaerobic buffer. Surprisingly, no reaction was observed when monitored at 480 nm. This is consistent with an earlier observation that the reaction of **P** and NO-CAM does not yield CAM product. Alternative ways to approach this reaction allow the kinetic time course to be monitored and yield product as described below.

Kinetic Parameters of the Reaction Pathway where NO-CAM and O_2 React with CmlI^{red}. The final steps in the reaction in which NO-CAM is converted to CAM can be examined by mixing CmlI^{red} with a buffer solution containing 5-150 fold excess of NO-CAM and a 5-fold excess O_2 (a saturated solution) (Figure 4-10 A). At 480 nm, one would expect to observe an increase in absorbance as **P** is formed and then a decrease as the NO-CAM is converted to CAM with the formation of CmlI^{ox}. Conducting the reaction in this way gave time courses that are fit reasonably well by a three-summed exponential equation. The resulting RRTs were plotted versus NO-CAM concentration as shown in Figure 4-10. The faster two phases show a hyperbolic dependence on NO-CAM concentration, while the slower phase shows no dependence. In this case, the amplitudes of the two faster phases have opposite sign, making it unlikely that they arise from parallel reactions. The hyperbolic dependences indicate that there is a fast reversible step that precedes the observable reaction, which must consist of at least 3 steps in accord with the three-exponential fit.

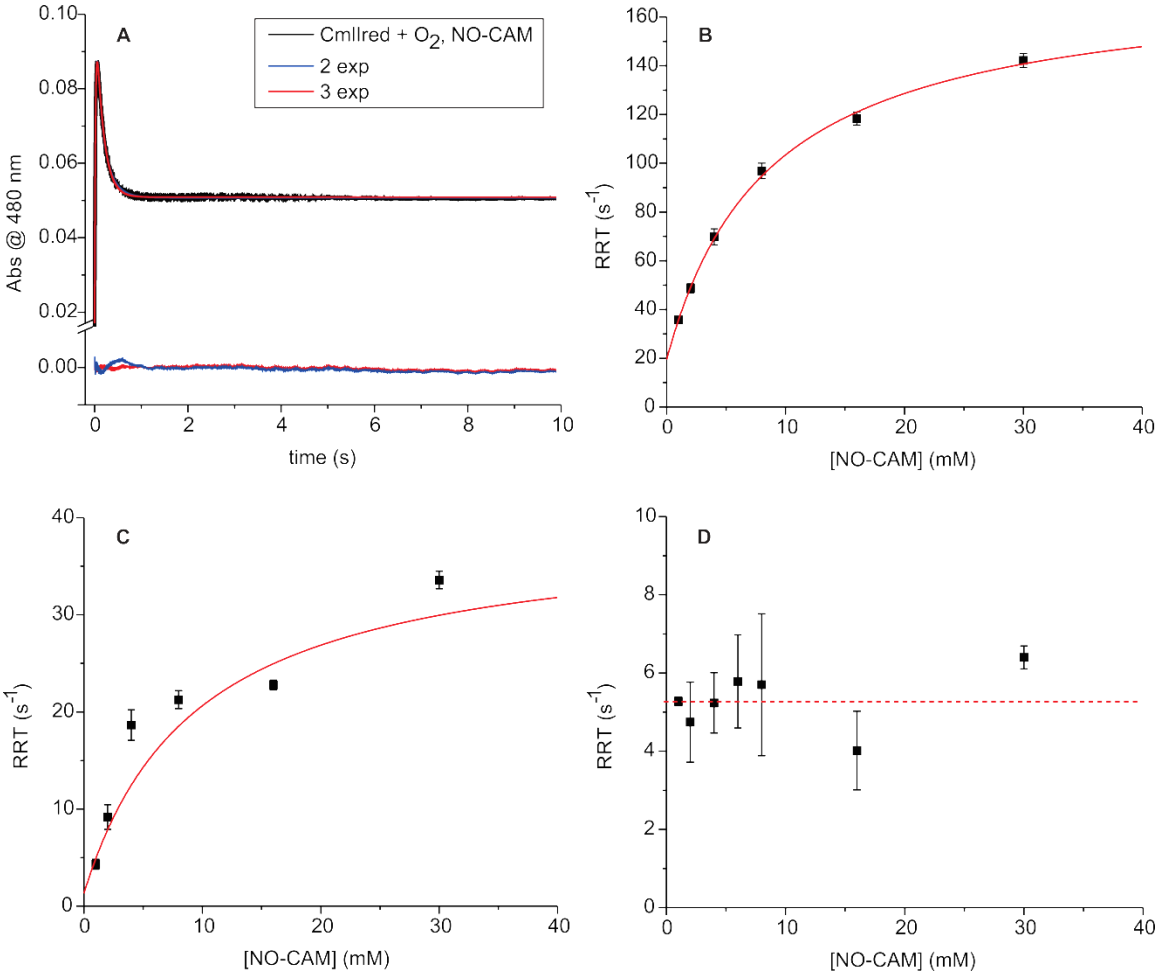

Figure 4-10: Reaction of $CmlI^{red}$ and NO-CAM in O_2-saturated buffer, 50 mM Bicine pH 9, 4 °C. A, Optical changes at 480 nm upon the mixture of 200 µM $CmlI^{red}$ and buffer containing 2 mM NO-CAM and 0.9 mM O_2 (all post mix, final concentrations), showing fit to two- (blue line) and three- (red line) exponential equations. B-D, Fits of the RRTs extracted from the optical absorption changes, showing NO-CAM concentration dependence of the RRTs for the reaction of NO-CAM-O_2 and $CmlI^{red}$. B, k_f = 136.4 ± 8.8 s^{-1}, k_r = 19.4 ± 2 s^{-1}, K_D = 8.6 ± 1 mM. C, k_f = 37.7 ± 10 s^{-1}, k_r ~ 0 s^{-1}. D, dotted line drawn in to estimate concentration-independent rate constant, k_f = 5.2 ± 0.01 s^{-1}.

Scheme 4-2 shows one interpretation of the reaction of $CmlI^{red}$ with O_2 and NO-CAM. In this model, NO-CAM binding is the fast reversible step that precedes the optically observable steps. O_2 binding in the following step to form **P** with k_f = 136.4 s^{-1} and k_r = 19.4 s^{-1} (calculated from the maximum and y-intercept the plot shown in Figure 4B). In the subsequent step, **P** reacts with NO-CAM irreversibly with k_f = 37.7 s^{-1} (maximum of the plot in Figure 4C). The irreversible nature of this step uncouples one of the RRTs from NO-CAM concentration, so the final concentration-independent step with k_f = 5.2 s^{-1} may be product release and represent the rate constant for substrate flux through the cycle. At high NO-CAM concentrations, the faster RRT

reaches values that far exceed the expected values based on the rate constant for **P** formation in the absence of NO-CAM (see above). This suggests that in the NO-CAM complex, O_2 binding is facilitated, allowing much faster **P** formation. A small amount of **P** may form prior to NO-CAM binding; this results in essentially a dead end complex as **P** cannot react with NO-CAM.

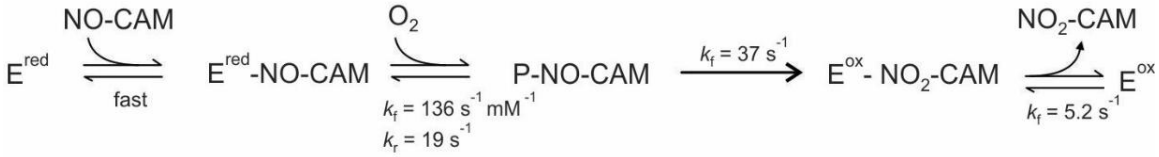

Scheme 4-2: Proposed scheme for the reaction of $CmlI^{red}$ with NO-CAM. Rate constants are derived from the plots in Figure 4-10. For simplicity $CmlI^{ox}$ and $CmlI^{red}$ are abbreviated as E^{ox} and E^{red}, respectively.

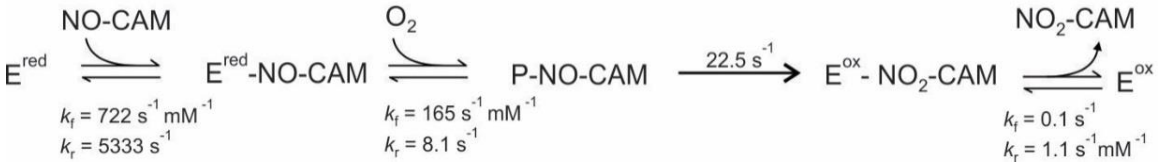

Scheme 4-3: Proposed scheme for the reaction of $CmlI^{red}$ with NO-CAM and O_2, with rate constants derived from numerical integration. For simplicity $CmlI^{ox}$ and $CmlI^{red}$ are abbreviated as E^{ox} and E^{red}, respectively.

The time course of the reaction shows that the maximum amount of **P** increases with NO-CAM concentration (Figure 4-11). Numerical integration fits to the Scheme 4-2 reaction adequately model the reaction time course as a function of NO-CAM concentration (Figure 4-12 A and Figure 4-13). Rate constants from the numerical integration are reported in the caption of Figure 4-13. The steps for which we know the rate constants by direct observation, which are the reaction of E^{red} or E^{red}-NO-CAM with O_2 to form P-NO-CAM, and the decay of that species to E^{ox}-NO_2-CAM, provide rate constants in the model with reasonably small margins of error. The rate constants for the first step, rapid binding of NO-CAM to E^{red}, have high variability because this step is not trackable at 480 nm, and may be too fast to monitor at any wavelength. The rate constants for product release, the proposed last step in this sequence, are also not adequately monitored at this wavelength.

Simulation revealed several important aspects of this reaction. One, the trends in the traces are reproduced by using the rate constants given by analysis of the RRTs and shown in Scheme 4-2. This is not to imply that Scheme 4-2 is the only solution, but it does represents a viable model of the reaction. Two, to obtain the correct shape of the traces, binding of NO-CAM

to CmlI^{red} is required to have fast k_f and k_r rates and the simulation predicts that NO-CAM release is 5-10 times faster than NO-CAM binding. This is consistent with our earlier observation that NO-CAM can exchange from the CmlI^{red} active site, although the rate of exchange predicted by the rate constants from the simulation is higher than the rate that would be predicted based on the observed flux of NO-CAM from the active site.[161] The previous experiment showed that about 15% of the NO-CAM was released from the active site over the course of five minutes, whereas the simulation-generated rate constants are sufficiently high to predict complete (100%) release. Thus, it is likely that the ratio of the exchange rates is accurate but not the absolute magnitudes. Third, accurate fits require a significantly higher rate constant for O_2 binding for the CmlI^{red}-NO-CAM complex than observed for **P** formation in the absence of substrate (165 s^{-1} vs. 1, 15, or 50 s^{-1} at 0.9 mM O_2). This increase in rate constant accounts for the observed increase in the maximum amount of **P** formed as a function of increased NO-CAM concentration. In this scheme, the increased maximum amount of **P** is due to the increased formation of the CmlI^{red}-NO-CAM complex, rapid O_2 binding to form **P**-NO-CAM, and relatively slow reaction of **P**-NO-CAM to yield CAM. Finally, O_2 binding is reversible when NO-CAM is present, which is surprising given that in the absence of substrate **P** formation is irreversible.

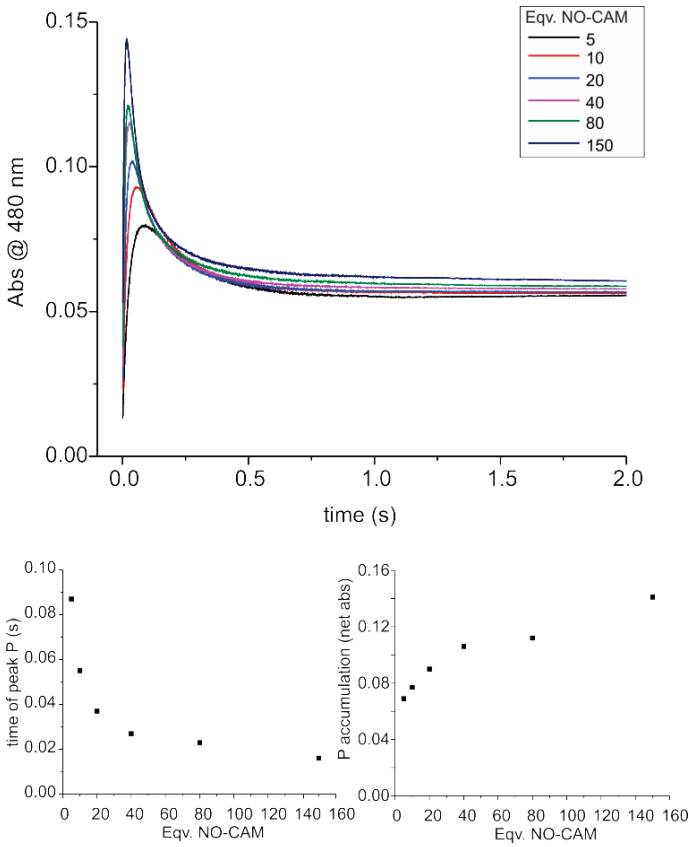

Figure 4-11: NO-CAM concentration dependence of trace shape, peak **P** time, and total **P** accumulation in the reaction of $CmlI^{red}$ with pseudo-first order concentrations of O_2 and NO-CAM. The traces follow the reaction of 200 µM $CmlI^{red}$ and 1-30 mM NO-CAM in O_2-saturated buffer, 50 mM Bicine pH 9, 4 °C.

A simulation in which O_2 could bind E^{red} before NO-CAM to form the dead end complex **P** was also tested, using the rate constant for **P** formation in the absence of substrate from Table 4-1 (Figure 4-12 B). At low concentrations of NO-CAM, a significant amount of **P** would form and persist, thus the endpoint absorbance would be expected to be quite high. The end point absorbance would also be expected to decrease as NO-CAM concentrations increased, as NO-CAM would become more likely to bind E^{red} first and thus less **P** (E^{red} + O_2) would form and persist. The simulation reflects these predictions and does not match the experimental data, suggesting that O_2 is in some way prevented from binding E^{red} before NO-CAM binds.

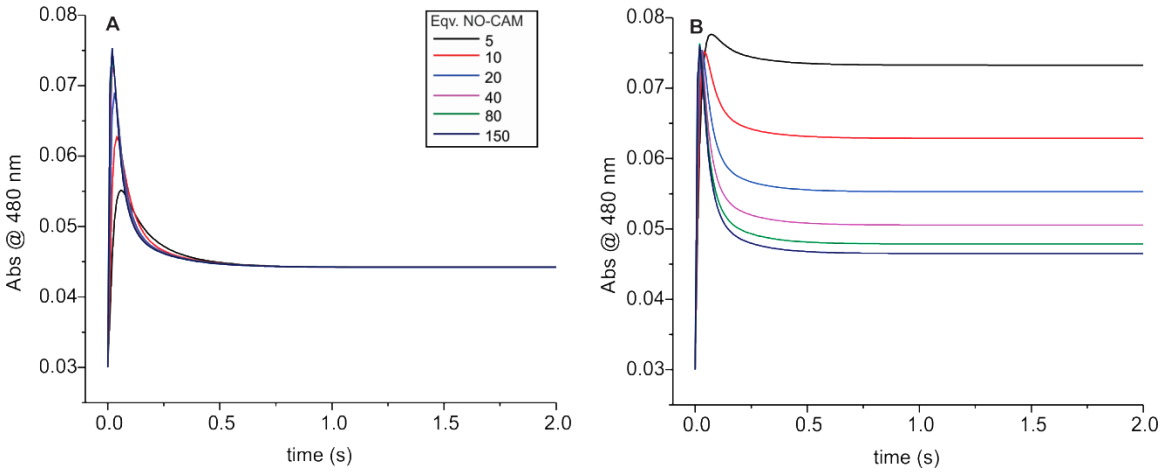

Figure 4-12: Comparison of two models for the reaction of E^{red} with NO-CAM and O_2. A, simulation of a model in which NO-CAM must bind first to E^{red}, as shown in Scheme 4-3 above. B, simulation of a model in which either O_2 or NO-CAM can bind first.

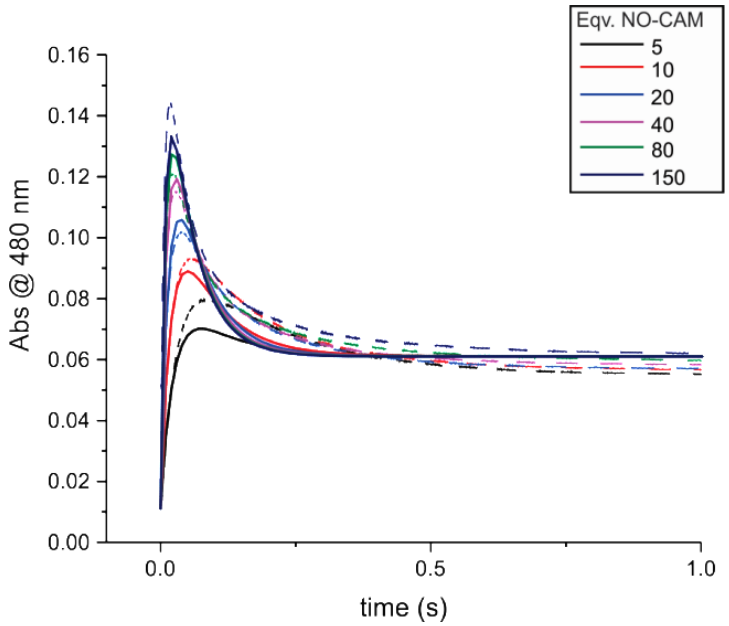

Figure 4-13: Optical changes in the reaction of $CmlI^{red}$ with varying NO-CAM concentrations and fivefold excess of O_2. Solid lines show the experimental data and dotted lines show the fit to the model shown in Scheme 4-3. Rate constants extracted from the fit are: k_1 = 722 ± 291 s^{-1} mM^{-1}, k_{-1} = 5333 ± 2220 s^{-1}, k_2 = 165 ± 1 s^{-1} mM^{-1}, k_{-2} = 8.1 ± 0.5 s^{-1}, k_3 = 22.5 ± 0.2 s^{-1}, k_{-3} = 0 s^{-1}, k_4 = 0.1 s^{-1}, k_{-4} = 1.1 ± 0.1 s^{-1} mM^{-1}

Verification of P as the Active Oxidant that Acts on NO-CAM. It was assumed, though never verified, that the active oxidant **P** that reacts directly with NH_2-CAM is the same active oxidant that reacts with NO-CAM to perform the final oxidation of the cycle. UV-vis spectroscopic data

showed that a species with absorbance at 480 nm formed and decayed when CmlI^{red} was reacted with NO-CAM and O_2 (Figure 4-14). To further verify the identity of the active oxidant in this step, short time point samples of the reaction of CmlI^{red} with an excess of NO-CAM and O_2 were prepared by a rapid-freeze quench procedure and analyzed by Mössbauer spectroscopy (Figure 4-15).

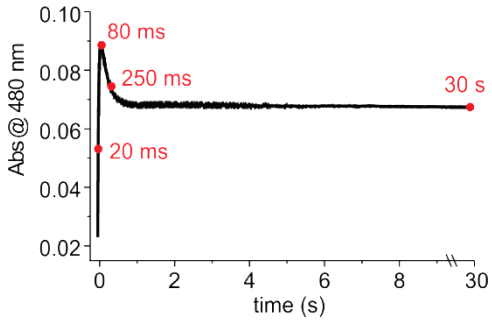

Figure 4-14: Time points chosen for Mössbauer analysis of the reaction of 200 µM CmlI^{red} with 0.9 mM O_2 and 2 mM NO-CAM (final, post mix concentrations). 50 mM Bicine pH 9, 4 °C.

Mössbauer analysis showed a decrease in CmlI^{red} over the course of the reaction, concomitant with an increase in **P**, for which the Mössbauer parameters have been previously determined (Table 4-4). At long time (30 s), < 5% **P** is present and the sample is predominantly diferric, suggesting that **P** has decayed via reaction with NO-CAM. The data supports the hypothesis that the same **P** is the active oxidant in the oxygenation of both NH_2-CAM and NO-CAM.

Table 4-4: Percentage of **P** and CmlI^{red} at various time points in the reaction of CmlI^{red} with NO-CAM and O_2, as determined by Mössbauer spectroscopy.

Quench time point	P	CmlI^{red}
20 ms	40%	30%
80 ms	59%	20%
250 ms	57%	10%
30 s	< 5%	< 1%

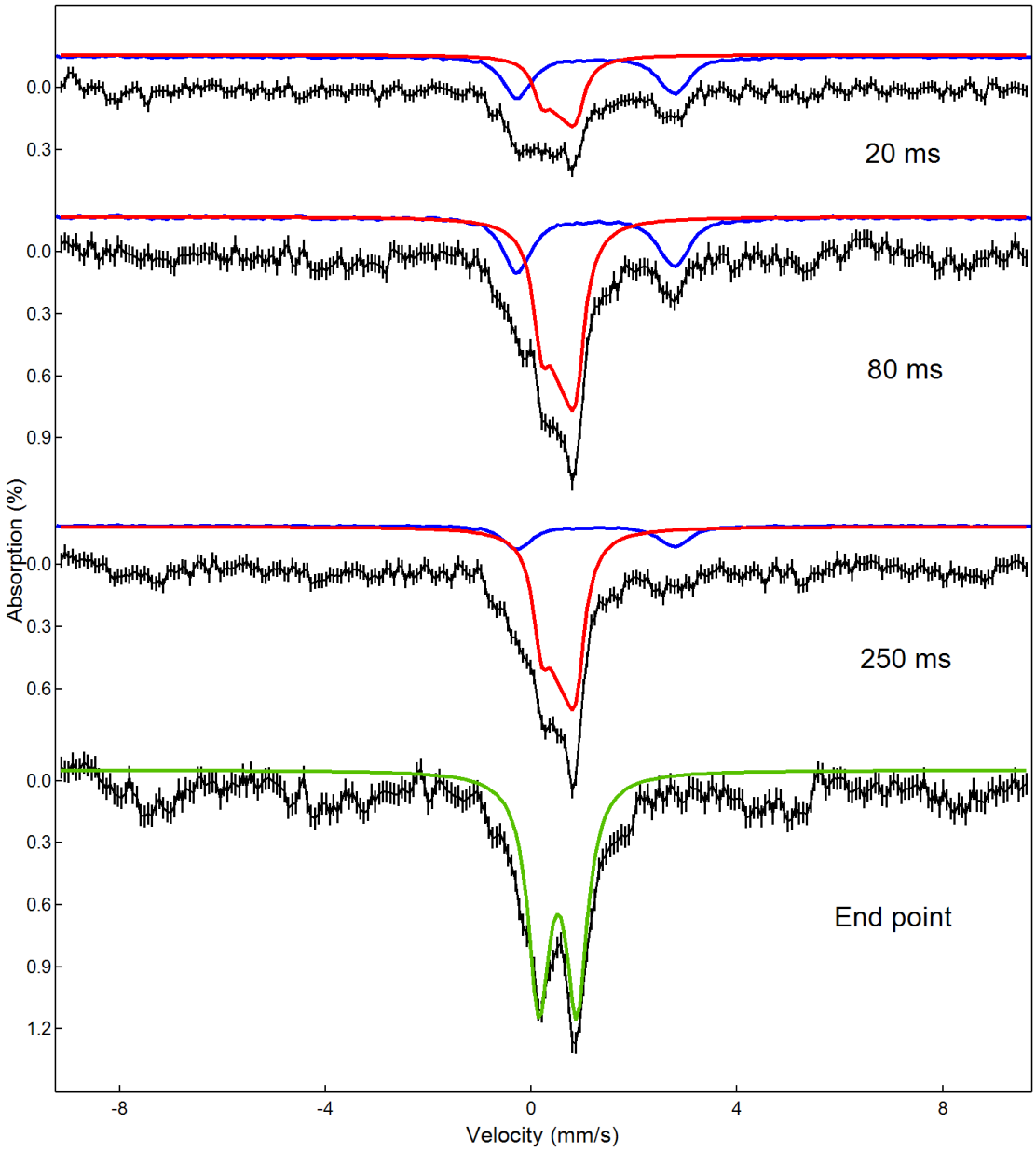

Figure 4-15: Mössbauer spectra of the 20 ms, 80 ms, 250 ms, and endpoint (30 s) time point samples of the reaction of 200 µM $CmlI^{red}$ with 0.9 mM O_2 and 2 mM NO-CAM. The black line is the experimental data and the colored lines are fits to various species: diferrous (blue), diferric peroxo (red) and resting state diferric (green). See Table 4-4 for percentages of each individual species.

Kinetic Parameters of the Complete Reaction Pathway. The complete biosynthetic pathway was examined by pre-equilibrating NH_2-CAM anaerobically with $CmlI^{red}$ to allow the complex to reach equilibrium and then initiating the reaction by mixing with O_2-saturated buffer. All optical changes were observed by stopped-flow UV-vis spectroscopy at 480 nm and 4 °C, pH 9. This

wavelength was chosen because it gives the maximum optical change for both the **P** formation and **P** decay processes. Using a shorter wavelength gives a greater optical change for **P** formation, but **P** decay is masked by reappearance of the Fe-O-Fe charge transfer band of diferric CmlI, which has a shoulder at ~375 nm. Initiating the reaction in this way allows both **P** formation and substrate-mediated **P** decay to be observed (Figure 4-16). The maximum amount of **P** formed is shown in Figure 4-16 to decrease and occur earlier in the time course as the concentration of NH_2-CAM increases.

After **P** forms and decays, the resulting $CmlI^{ox}$ is reduced by the NH(OH)-CAM product of the first reaction to give a further decrease in absorbance. This reduction is followed by binding of O_2 to re-form **P**, resulting in an increase in absorbance. Finally, **P** decays as CAM is formed to give a decrease in absorbance. Both NH_2-CAM and O_2 are supplied in high enough concentrations that all of the reactions can be considered first order or pseudo first order. Also, the reaction halts and becomes irreversible when CAM is ultimately formed, so summed exponential fitting of the time course is appropriate. The time course can be adequately fit using a three summed exponential equation in the time range monitored, and the resulting plots of RRT versus NH_2-CAM concentration are shown in Figure 4-17.

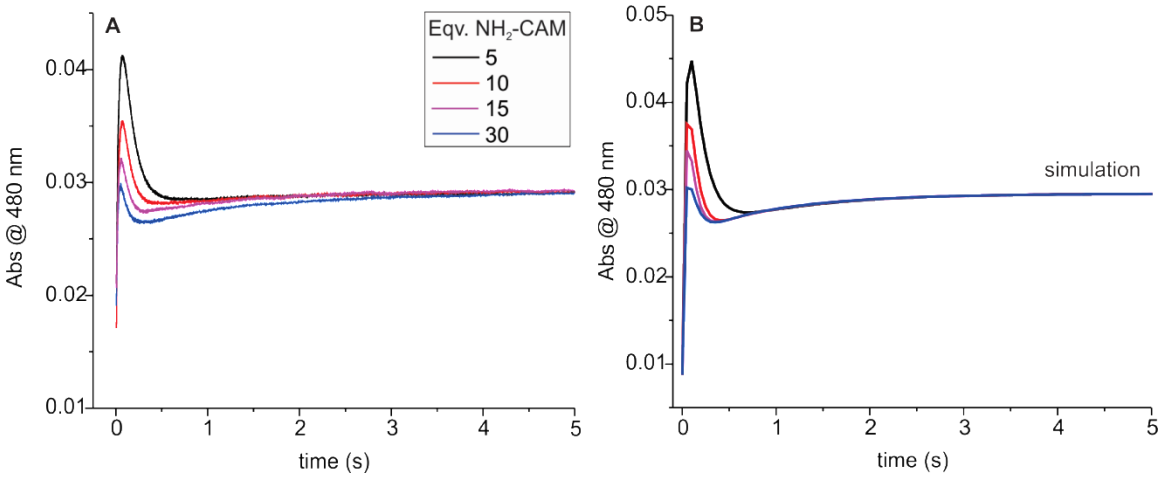

Figure 4-16: NH_2-CAM concentration dependence of **P** formation and decay. A: Optical changes at 480 nm from the reaction of $CmlI^{red}$ (200 µM) and 1-6 mM NH_2-CAM (final, post mix concentrations) with O_2-saturated buffer. Post-mix [O_2] ~ 0.9 mM at 4 °C. 50 mM Bicine pH 9, 4 °C. B: Simulation of experimental data in A.

One way to analyze these plots is to assume that the linear plot seen for the fastest RRT gives information about the k_f (slope), k_r (y-intercept) and K_D (y-intercept/slope) for NH_2-CAM binding to $CmlI^{red}$ (monitored by rapid subsequent binding of O_2 to form **P**), and the nearly

hyperbolic plot of the second fastest RRT gives information about the k_f (RRT observed approaches $k_f + k_r$) and k_r (y-intercept) reaction of **P** with bound NH_2-CAM. This type of analysis was used in the previous reaction iterations and is appropriate if the reverse rate constant for the first reaction (24.1 s^{-1}) is fast relative to the forward rate constant for the second reaction (21.6 s^{-1}), which is not the case for the fits shown in Figure 4-17. Another check is that the K_D computed from the linear plot (3.5 mM) should equal the K_D from the fit to the hyperbolic plot (1.34 mM), which is also not correct. A more precise method to analyze the data using the slopes and intercepts of the sums and products of the RRTs plotted versus NH_2-CAM concentration (Figure 4-18, Scheme 4-4). However, this approach yields a value of the K_D for NH_2-CAM binding which is ten-fold lower than the value estimated from the reaction of NH_2-CAM with **P** described above. Two additional problems with this simple approach to analysis are: (1) a reaction scenario that requires formation of the $CmlI^{red}$-NH_2-CAM complex prior to formation of **P** in a reactive state would be expected to show increasing maximum concentrations of **P** as the NH_2-CAM concentration increases, which is opposite of what is observed, and (2) if the rapid formation of **P** that follows NH_2-CAM binding is irreversible like the formation of **P** in the absence of substrate, then the concentration dependence of the slow phase would be lost.

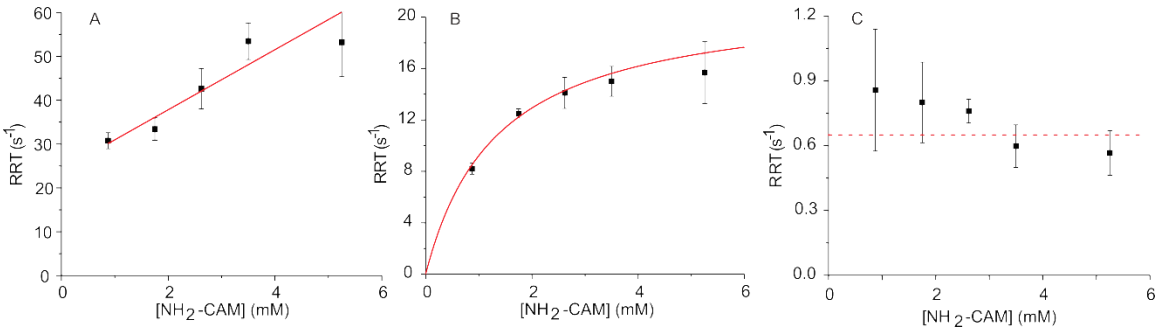

Figure 4-17: NH_2-CAM concentration dependence of RRTs for the reaction of $CmlI^{red}$-NH_2-CAM and O_2. Extracted RRTs plotted versus [NH_2-CAM] for the reaction of $CmlI^{red}$ (200 µM, final post-mix concentration) premixed with varying concentrations of NH_2-CAM and O_2-saturated buffer (~0.9 mM at 4°C). A, k_f = 6.9 ± 1.4 s^{-1} mM^{-1}, k_r= 24.1 ± 2.7 s^{-1}, K_D = 3.5 mM. B, k_f = 21.6 ± 1.7 s^{-1} mM^{-1}, k_r~ 0 s^{-1}. C, k_f = ~ 0.7 s^{-1}. 50 mM Bicine pH 9, 4 °C.

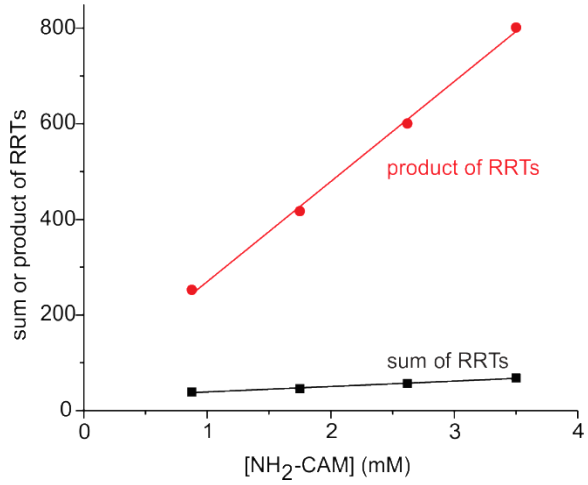

Figure 4-18: NH_2-CAM concentration dependence of RRTs for the reaction of $CmlI^{red}$-NH_2-CAM and O_2. Linear fit of sum of extracted RRTs (black line) and product of extracted RRTs (red line) plotted versus [NH_2-CAM] for the reaction of $CmlI^{red}$ (200 µM, final post mix concentration) premixed with varying concentrations of NH_2-CAM and O_2-saturated buffer (~0.9 mM at 4 °C). 50 mM Bicine pH 9, 4 °C.

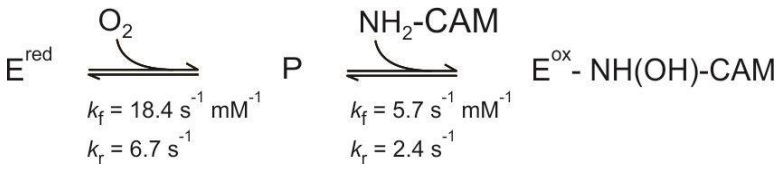

Scheme 4-4: Proposed scheme for the reaction of $CmlI^{red}$ with O_2 and NH_2-CAM to form NH(OH)-CAM with rates derived from Figure 4-18.

An alternative way to consider the reaction is suggested by the experiments described above in which **P** can form rapidly in the absence of substrate and then react with NH_2-CAM in a separate reaction. It is evident that the rate constant for oxidation of $CmlI^{red}$ is maximized as the complex of $CmlI^{red}$ with NH_2-CAM saturates (Figure 4-16), a reaction that involves the intermediate P and product formation. Shown in Scheme 4-5 is an alternative pathway in which the reaction can proceed through rapid initial reaction of either $CmlI^{red}$ or $CmlI^{red}$-NH_2-CAM with O_2 to form **P** or **P**-NH_2-CAM, respectively. The reaction ends with all of the CmlI in the diferric state, independent of the concentration of NH_2-CAM used, so both forms of **P** must be reactive. Allowing **P**-NH_2-CAM to form by either of the pathways shown would account for: (1) the failure of the less complex analytical approaches, (2) a possible route to the observed decrease in the maximum amount of **P** formed during the time course, and (3) the hyperbolic concentration dependence of the slow phase since reversible substrate binding occurs after the irreversible **P** formation step in one branch of the pathway.

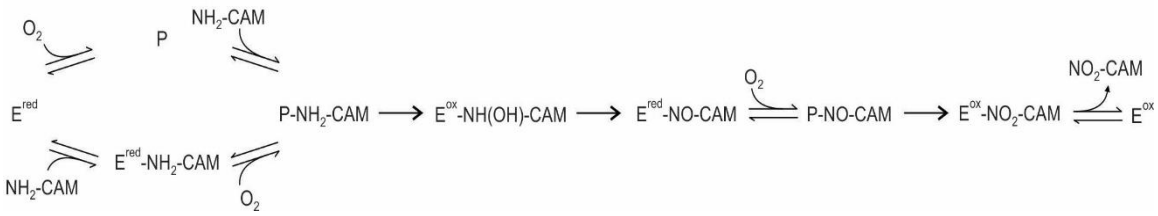

Scheme 4-5: Proposed scheme for the reaction of CmlI^{red} with NH_2-CAM and O_2. For simplicity CmlI^{ox} and CmlI^{red} are abbreviated as E^{ox} and E^{red}, respectively.

As discussed above, an integrated rate equation for a complex scenario such as the reaction depicted by Scheme 4-5 can be derived; however, the number of reversible steps would make the resulting equation quite complex. Another approach is to fit the observed time courses by numerical integration using the rate constants derived from the individual steps described in the sections above to limit the number of unknown parameters. The rate constants for the simulation (Figure 4-16 B) are shown in Scheme 4-6, below. However, the bounds of the simulated rate constants are quite large and not sufficient for accurately reporting such constants. Thus these rate constants describe a solution, but certainly not a unique one. It is likely that additional data points (i.e., additional concentrations of NH_2-CAM) are required to accurately fit a scheme as complex as this one. The input rate constants for the simulation came from the plots in Figure 4-17.

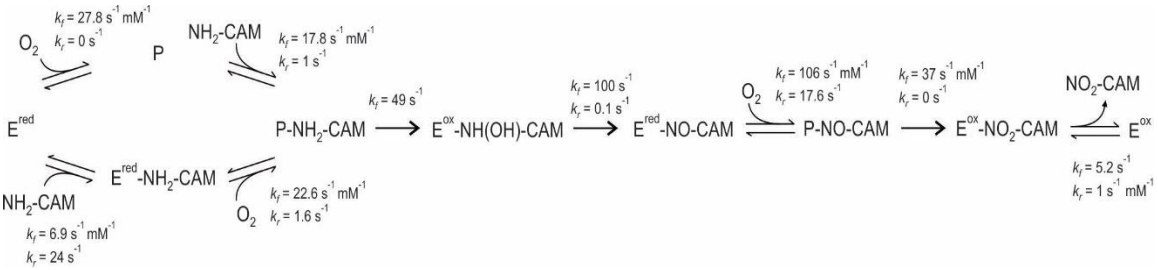

Scheme 4-6: Proposed scheme for the full cycle reaction of CmlI^{red} with NH_2-CAM and O_2, with rate constants from numerical integration of the model.

To simplify analysis and prevent the final stage of the reaction shown in Figure 4-16, where multiple processes are occurring at the same time, the experiment was repeated using limiting O_2. In this scenario, 400 µM CmlI^{red} was mixed in a 1:1 ratio with buffer containing 360 µM O_2 and a range of NH_2-CAM in pseudo-first order concentrations. Unfortunately, under these conditions **P** did not form as quickly, and thus did not accumulate enough to allow fitting of two

or more separate phases. Figure 4-19 shows the difference between maximum **P** accumulation and the **P** accumulation that was observed under these conditions.

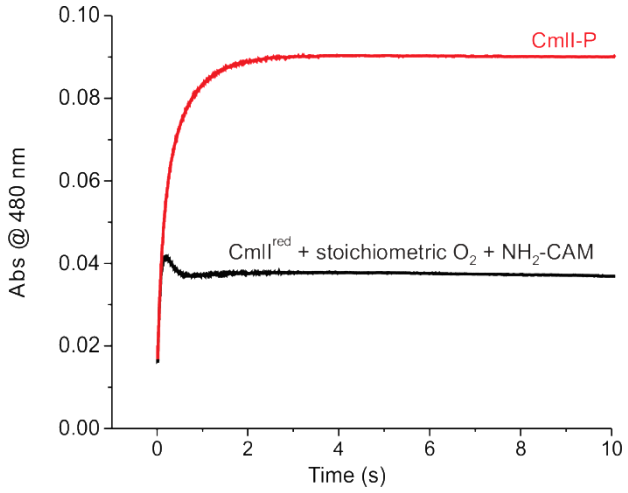

Figure 4-19: Comparison of maximum **P** formation achieved by mixing 200 µM CmlI^{red} with 0.9 mM O_2 (red trace) versus **P** formation and decay when 200µM CmlI^{red} is mixed with 180 µM O_2 and 2mM NH_2-CAM (black trace). All concentrations reported are final, post mix values. Optical changes monitored by stopped flow at 480 nm. 50 mM Bicine pH 9, 4°C.

Discussion

The CmlI cycle was described kinetically by monitoring absorbance changes resulting from different combinations of CmlI and the various substrates. Both the individual steps of the cycle and the cycle as a whole were monitored. The extracted rate constants and insight into binding order obtained from these experiments now allow us to construct a kinetic model of the CmlI cycle.

Applying Kinetic Insight to Evaluate the Proposed Mechanism. Elucidating the kinetics of the CmlI cycle required close analysis by UV-vis spectroscopy. All of the observed absorbance changes were consistent with the previously proposed mechanistic model, presented in Figure 4-1. As expected, the reaction of **P** and NH_2-CAM in the absence of O_2 resulted in CmlI^{red} due to the NH(OH)-CAM-mediated reduction step. The reaction of CmlI^{red}, O_2, and NH_2-CAM carries through the whole cycle due to excess O_2, but the traces show a slight dip and rise after the initial **P** decay, again indicative of the substrate-mediate reduction step. Finally, NO-CAM reacts with CmlI^{red} in the presence of O_2 to form first **P**, which then rapidly decays to the

CmlI^{ox} resting state. This work also provides experimental evidence for the earlier supposition that **P** is the active oxidant in both oxygenation steps of the cycle, via Mössbauer analysis of the oxidant responsible for the conversion of NO-CAM to NO_2-CAM.

Evaluation of the Single Active Site Hypothesis. In our previous work we showed that the entire six-electron amine to nitro conversion could occur in a single CmlI active site. This work provides further evidence for the retention of the organic intermediates in the active site. Firstly, the cluster reduction mediated by NH(OH)-CAM occurs at a very fast rate (estimated > 100 s^{-1}) when NH(OH)-CAM is generated in the active site by reaction of **P** and NH_2-CAM, as shown by the analysis of Figure 4-5. The reduction rate is much slower, $k_f \sim 1\ s^{-1}$, when NH(OH)-CAM is added to the system externally to diferric CmlI. This suggests that the NH(OH)-CAM likely does not leave the active site in which it was formed to bind at another active site during the native cycle. Secondly, NO-CAM only reacts with **P** when the substrate is already bound in the active site, and no reaction with **P** occurs if NO-CAM is added externally to **P**. Again, this suggests that NO-CAM stays in the active site to avoid decoupling of the reaction. Based on the relatively slow rebinding of the organic intermediates, enforcing a single site mechanism allows the reaction to happen more quickly. Equally importantly, this ensures that the relatively reactive organic intermediates are not allowed into the cell to neutralize each other through coupling reactions, or have deleterious effects by reaction with other cell components.

The Formation of Intermediate P. We have shown previously that a stable **P** intermediate is formed when the diferrous enzyme is rapidly mixed with O_2, and that **P** is reactive towards the native substrate to form the native product CAM. In an effort to understand the kinetics of **P** formation, CmlI^{red} was reacted with a range of pseudo-first-order concentrations of O_2 and the resulting RRTs were plotted to obtain kinetic constants. In the absence of substrate, **P** forms via three parallel pathways, indicating that either O_2 can bind the same active site in the three different fashions, or there are three different configurations of the active site present in the bulk enzyme. The latter explanation is supported by the fact that Mössbauer spectroscopy shows at least two different configurations of the diiron cluster active site in diferric state. We hypothesized that the presence of substrate might enforce a particular active site conformation that would subsequently enforce a single **P** formation process, so we did the same set of reactions in the presence of the product CAM. CAM is analogous to the substrate in shape, size, and

chemical makeup, but it is not reactive towards **P**. Introduction of CAM to the reaction mixture resulted in two linearly O_2-dependent phases, compared with three such phases in the absence of CAM. Comparing the second order rate constants obtained from each scenario suggests that the presence of CAM eliminates the fastest **P** formation pathway.

Further evidence for the impact of substrate presence on **P** formation comes from the reactions of the diferrous enzyme with substrate (NH_2-CAM or NO-CAM) and O_2. In both cases the presence of substrate resulted in a single exponential phase with a negative amplitude, indicating that the number of **P** formation pathways is reduced to one, or one pathway becomes significantly dominant so that a second pathway cannot be detected. Simulations of the reaction of $CmlI^{red}$ with O_2 and NH_2-CAM case gave **P** formation rate constants of 27.8 mM^{-1} s^{-1} and 22.6 mM^{-1} s^{-1} (Scheme 4-6), comparable to the fastest **P** formation rate in the presence of CAM and a slight increase in the middle rate in the substrate-free **P** formation. When NO-CAM is added to the reaction of E^{red} with O_2, the rate constant for **P** formation increases 3 - 130 fold compared to the case in which substrate is absent. This effect is visualized in Figure 4-11, where increasing NO-CAM causes **P** to form earlier (faster) and to accumulate more. Altogether, this data indicates that substrate has an impact on **P** formation, both by enforcing a single pathway and by accelerating O_2 binding. Whether the effects are due to direct binding to the active site, or are hysteretic, remains unknown.

Importance of Binding Order and Hysteretic Effects. This work reveals the importance of binding order when O_2 and substrate are presented to an enzyme. Both NH_2-CAM and NO-CAM require O_2 to react, so binding order is a consideration. Curiously, the two substrates have different binding order preferences versus O_2.

The reaction of $CmlI^{red}$ with O_2 and NH_2-CAM results in formation of **P** and product regardless of which substrate binds first. In addition to experimental data, simulation of the reaction of the three species ($CmlI^{red}$, NH_2-CAM, O_2) showed that a two-pathway model is required to obtain a fit with the observed trends in the data. In contrast, the reaction with NO-CAM shows a clear preference. **P** does not react with NO-CAM, as shown by spectroscopic and product analysis. One possible explanation for this contrast is that the peroxo species (**P**) that forms in the absence of substrate and reacts with NH_2-CAM is not the same peroxo species that reacts with NO-CAM. However, Mössbauer analysis of the reactive species that forms in the presence of O_2 and NO-CAM shows that it is **P**, or if it is different, the differences are small enough not to be resolvable by Mössbauer. Clearly, some other mechanism is at play such that the

enzyme is set up to react NO-CAM and **P** only if NO-CAM is bound first (i.e., already in the active site from the NH(OH)-CAM reduction).

Unlike binding NH_2-CAM, which necessarily is initiated when NH_2-CAM enters from the exterior of the enzyme, there may be no efficient pathway for NO-CAM bind when introduced exterior to the enzyme. CmlI is designed to have this substrate already positioned correctly in the active site from the oxidation of NH(OH)-CAM. When NO-CAM is introduced mid-cycle, as in some of the experiments reported, it may exchange rapidly with a second site before binding the active site. This explanation would account for the rapid rate constants from NO-CAM binding predicted by the simulation of the reaction of $CmlI^{red}$ with O_2 and NO-CAM, but the experimentally observed relatively slow exchange of NO-CAM from the active site (discussed above).

An important observation from this body of work is that hysteretic effects of substrate binding are likely playing a role in enzyme regulation. One example of this is the convergence of the **P** formation pathways into one pathway in the presence of substrate. Another example is the fact that O_2 binding is reversible in the presence of substrate but not in the absence. A third example is that O_2 is seemingly not allowed to bind $CmlI^{red}$ when NO-CAM is present but not bound. Taken together it appears that substrate binds to some site other than the active site to convert the enzyme to an active form prior to the binding of any small molecule or organic molecule.

Overall Kinetic Model. A kinetic model of the overall reaction was constructed using reactivity information and rate constants from all the reactions performed, as well as insight gained from the simulations. Scheme 4-7 shows the model that assembles all of the available information. The portions of the scheme printed in black represent the portions that are part of the native cycle, the portions in blue represent the off-pathway components that are accessible by experimental manipulation but are not thought to be part of the in-vivo cycle based on the current study.

The reaction begins when $CmlI^{red}$ is mixed with its substrates O_2 and NH_2-CAM. First, we recognize that the organic substrate presence has a hysteretic effect on O_2 binding. Thus, the first step of the reaction is rapid binding of NH_2-CAM to some location on the enzyme other than the active site, to convert the enzyme into a different form. The substrates bind to E^{red} to form **P**-NH_2-CAM via one of two pathways; currently there is no evidence to indicate whether only one, or both, of these pathways is valid in-vivo. We know from previous work that $CmlI^{red}$ can react

with O_2 to form a stable **P** species that can react with substrate in a subsequent step.[52] The rate constant for **P** formation is taken from the plots in Figure 4-3; justification for choosing the middle rate was explained earlier and is supported by the simulation-generated rates in Scheme 4-5. The rate for subsequent **P** reaction with NH_2-CAM is based on the K_D in Figure 4-7 A and on the simulation-generated rates. Second, we showed that pre-equilibration of $CmlI^{red}$ with NH_2-CAM followed by exposure to O_2 also results in **P** formation and subsequent generation of product. For this second pathway, the rate constant for $CmlI^{red}$ binding NH_2-CAM is taken from Figure 4-17 and for subsequent O_2 binding the rate constant is that for O_2 binding to an ES complex (Figure 4-4).

P-NH_2-CAM rapidly reacts to form $CmlI^{ox}$-NH(OH)-CAM (Figure 4-7) and the subsequent oxidation of NH(OH)-CAM to NO-CAM is fast. If NH(OH)-CAM escapes the active site before the reaction can occur, then the reduction occurs at a much slower rate, probably due to slow rebinding or incorrect binding followed by a necessary reorganization in the active site (Scheme 4-1). NO-CAM appears to be loosely bound in the active site when CmlI is in the diferrous form, and based on spectroscopic and product analysis, no reaction ensues if O_2 binds when NO-CAM is not present. However, NO-CAM dissociation from the active site is prevented by rapid binding of O_2 in vivo. O_2 binds rapidly but reversibly to the E^{red}-NO-CAM complex to form **P**-NO-CAM, which reacts to form the NO_2-CAM product and the resting state CmlI. An observed concentration- independent step with $k_f = 5.2\ s^{-1}$ may be product release from the active site (rate constants from Figure 4-10).

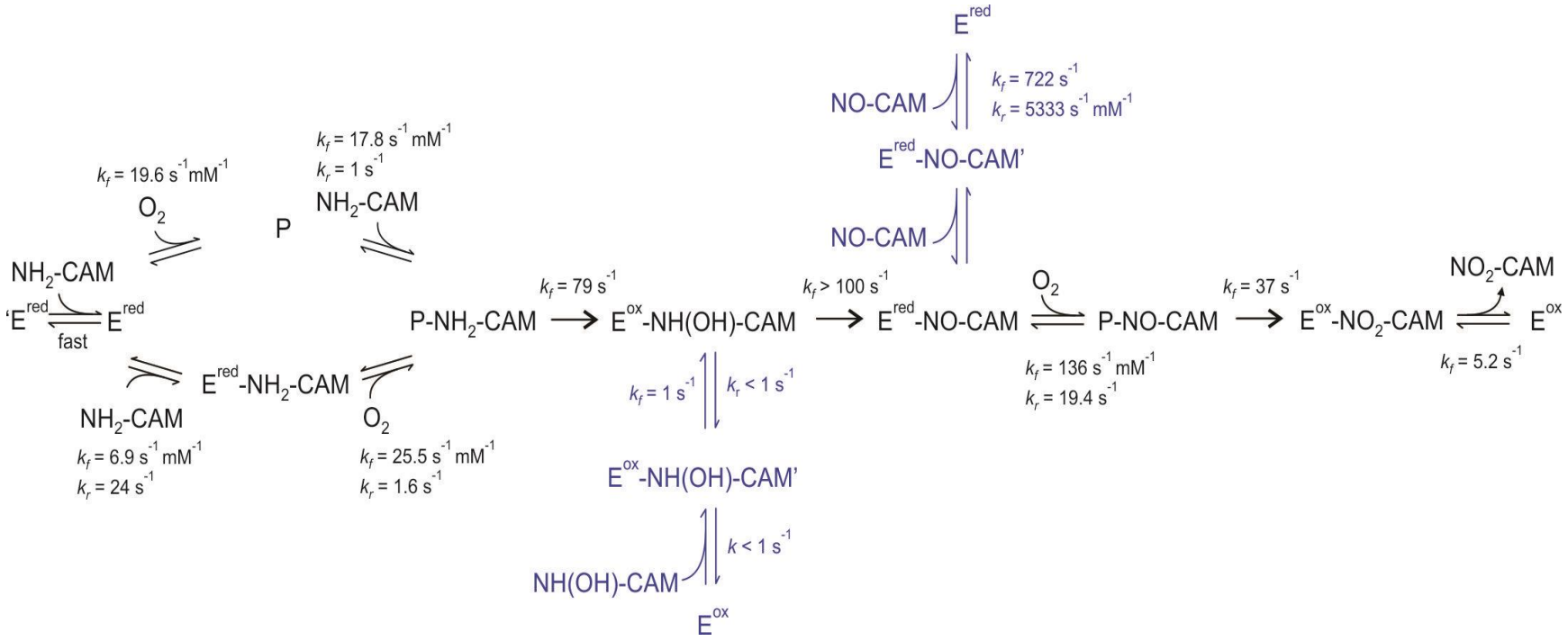

Scheme 4-7: Proposed scheme for the reaction of CmlI^{red} with NH_2-CAM and O_2 to form NO_2-CAM. For simplicity CmlI^{ox} and CmlI^{red} are abbreviated as E^{ox} and E^{red}, respectively. Black text represents components of the native cycle, blue components are experimentally accessible but not thought to be part of the native cycle. The steps in which NO-CAM and NH(OH)-CAM bind from the exterior may be multiple steps, i.e., initially binding to region other than the site or to the active site in the incorrect orientation, followed by reorganization.

Future Work

This work provides support for the substrate-mediated reduction model of N-oxygenation by diiron-cluster containing enzymes. A couple of additional pieces of data would help to corroborate the conclusions stated in this work. First, additional data points in the reaction investigating NH_2-CAM concentration dependence on the reaction of $CmlI^{red}$, O_2, and NH_2-CAM (as seen in Figure 4-15) would likely provide a better platform for numerical integration of the proposed reaction model. Second, photo-diode array (300 – 800 nm) absorbance data of the reactions monitored here by single wavelength may provide additional information about rapid substrate binding, as is proposed in many steps. This may lead to the ability to monitor substrate binding and determine rate constants therein at different wavelengths than the reactions were initially monitored, or at least inform on any expected optical changes when substrate binds. Mössbauer analysis of enzyme-substrate complexes may confirm that the binding of substrate, to the active site or otherwise, changes the electronics of the CmlI active site. Finally, a method of evaluating overall flux in the cycle would inform on which rate constants are part of the productive cycle and which correspond to decoupled side reactions. This additional information about substrate interaction with the enzyme will help finalize the model presented in Scheme 4-7. This model, combined with previous analytical and spectroscopic work, supports the hypothesis that the full six-electron conversion of an aryl-amine to an aryl-nitro product can occur in a single enzyme active site, requiring neither dissociation of the organic intermediates, nor mid-cycle injection of external electrons.

Acknowledgements

Dr. Brent Rivard provided assistance in carrying out the stopped-flow experiments and the preparation of the rapid-freeze-quench samples. Dr. Rahul Banerjee also assisted with the rapid-freeze-quench samples, as well as training and assistance with the numerical integration using KinTek. Both Drs. Rivard and Banerjee, as well as Dr. Melanie Rogers, provided invaluable kinetic insight and help troubleshooting the stopped-flow instrumentation. The Mössbauer samples were analyzed by Dr. Yisong (Alex) Guo and Ruixi Fan at Carnegie Mellon University, Pittsburg, PA.

Chapter 5

Experimental methods

Summary

This chapter describes all of the reagents and methods used to perform the experiments reported in the previous three chapters. An effort was made to be informative without overwhelming with detail or repetitiveness. To that end, the reader is recommended to use this chapter in conjunction with the text of the experiment in the appropriate previous chapter to provide a complete picture of how an experiment was completed.

Reagents

General Reagents. Water used in all experiments was purified with a Millipore Super-Q system. ^{57}Fe (95.5 %) was purchased from Cambridge Isotope Laboratories (Andover, MA). Amino-chloramphenicol (D-threo-1-(4-aminophenyl)-2-dichloroacetylamino-1,3-propanediol hydrochloride) (NH_2-CAM) was purchased from Toronto Research Chemicals, Inc. *p*-aminophenol (pAP), *p*-aminobenzoate (pABA), and L-p-aminophenylalanine (L-pAPA) were purchased from Sigma-Aldrich. Bicine and other standard reagents used were purchased from Fisher. $^{18}O_2$ gas (98 atom %) was purchased from Icon Isotopes, Summit, NJ.

Synthesis and Characterization of NO-CAM and NH(OH)-CAM. The nitroso and hydroxylamine derivatives of chloramphenicol (NO-CAM and NH(OH)-CAM, respectively) were synthesized according to published methods.[151] The reported final purification of NO-CAM with Sephadex LH20 was not performed. Instead, normal phase chromatography (SiO_2, ethyl acetate) was used as a final purification step for both compounds. The final purity, estimated via integration of the ^{1}H-NMR, was 90% for NO-CAM and 80% for NH(OH)-CAM. Residual proteated solvent (δ 3.31) was the reference compound for ^{1}H-NMR. These products were characterized and found to have the spectral characteristics listed below.

2,2-dichloro-N-[(1R,2R)-1,3-dihydroxy-1-(4-nitroso)propan-2-yl]acetamide (NO-CAM). Green solid: λ_{max} = 316 nm (aqueous 0.1% formic acid). R_f = 0.40 (SiO_2, ethyl acetate). ^{1}H NMR (500 MHz, CD_3OD): δ_H 7.85 (2H, d, J_1 = 8 Hz), 7.71 (2H, d, J_1 = 8 Hz), 6.24 (1H, s), 5.14 (1H, d, J_1 = 3 Hz), 4.18-4.08 (1H, m), 3.82 (1H, dd, J_1 = 7 Hz, J_2 = 11 Hz), 3.62 (1H, dd, J_1 = 6 Hz, J_2 = 11 Hz).

2,2-dichloro-N-[(1R,2R)-1,3-dihydroxy-1-(4-hydroxylamine)propan-2-yl]acetamide (NH(OH)-CAM-). λ_{max} = 237 nm (aqueous 0.1% formic acid).Pale yellow gum: ^{1}H NMR (500 MHz, CD_3OD): δ_H 7.25 (2H, d, J_1 = 8Hz), 6.94 (2H, d, J_1 = 9Hz), 6.930 (1H, s), 4.90 (1H, d, J_1 = 4Hz), 4.05-4.02 (1H, m), 3.72 (1H, dd, J_1 = 6Hz, J_2 = 11Hz), 3.50 (1H, dd, J_1 = 6Hz, J_2 = 11Hz).

Preparation of Wild Type CmlI and ^{57}Fe CmlI

Cloning and Heterologous Expression of CmlI. CmlI was cloned from genomic DNA isolated from *Streptomyces venezuelae* mycelia. The primers used for PCR amplification of CmlI are shown with restriction sites underlined:

Forward: CCATATGGCGATCGCCCGTGACCACACGGACGAGAAA

Reverse: CCATATGGTTTAAACTCATCGGGTCACCGTCGTGCC

PCR products were digested with AsiSI and PmeI and ligated to similarly digested pVP91A, obtained from the DNASU plasmid repository, to produce the N-terminal His_8 tagged enzyme. The final CmlI-containing plasmid was verified by sequencing at the University of Minnesota Biomedical Genomics Center. Plasmid stocks are maintained by regeneration ~ every six months using the QIAprep Spin Miniprep Kit (Qiagen).

Expression of CmlI. Expression of CmlI was performed in *E. coli* BL21(DE3) in M9 minimal medium in the presence of 100 μg/mL ampicillin. Cells were grown to an OD ~ 1.0 and induced with 150 μM IPTG and 50 μM $FeCl_3$ at which point the temperature was lowered to 20 °C, and growth was allowed to continue for an additional 15 h. Cells were harvested by centrifugation and stored at -70 °C until further use. ^{57}Fe enriched CmlI was prepared similarly from cells grown in M9 media with the addition ^{57}Fe metal dissolved in a minimal volume of *aqua regia* to a final concentration of 25 μM.

Purification of CmlI. To purify CmlI, cells were resuspended in 50 mM potassium phosphate pH 7.4, 300 mM NaCl, 10 mM imidazole, lysed via sonication, and centrifuged. The resulting supernatant was loaded onto a Ni nitrilotriacetic acid column (Qiagen) equilibrated in the same buffer. After loading, the protein was eluted using an imidazole gradient. Protein-containing fractions were pooled and dialyzed against 25 mM Bicine pH 9 and stored at -80 °C until further use. CmlI concentrations were determined by calculated extinction coefficient checked against denatured protein ($\varepsilon 280 = 50\ mM^{-1}\ cm^{-1}$). To assess metal content, CmlI quantified by 280 nm absorbance was treated in 4 M nitric acid for 2 hours. The denatured sample was centrifuged at 25,000 x g for 20 min and the supernatant transferred to a volumetric flask for dilution to 5 ml

with dH_2O. The metals present in the sample were quantitated using inductively-coupled plasma mass-spectrometry (ICP-MS) at the UMN Earth Sciences Department.

Generation of Diferrous and Peroxo-Diferric CmlI

Preparation of CmlI Diferrous Intermediate ($CmlI^{red}$). As isolated diferric CmlI (0.5 – 1.5 mM) was reduced under anaerobic conditions with an excess amount of dithionite in the presence of 0.05 - 0.1 equivalent of methylviologen. Excess reductant and methylviologen were removed using a PD-10 desalting column (G-25, GE Healthcare) in an anaerobic chamber. If high concentrations were required (i.e., for spectroscopic samples), protein was concentrated using a centrifuge located in the anaerobic chamber and 10 or 30 kDa cutoff filters (Amicon Ultra-0.5 ml centrifugal filters).

Preparation of CmlI Diferric Peroxo Intermediate (P). Aliquots of reduced CmlI were exposed to either $^{16}O_2$ or $^{18}O_2$ at ~ 4 °C for several min. **P** concentration was determined by absorbance at 500 nm ($\varepsilon = 500\ M^{-1}\ cm^{-1}$) under the assumption of nearly stoichiometric formation of the intermediate.

Preparation of P in D_2O or $H_2{}^{18}O$. P in D_2O was generated as described above, except that the enzyme was passed through a PD-10 size exclusion column equilibrated with buffer prepared with D_2O (50 mM Bicine, pD 9) after the reduction step. Concentration and re-dilution with D_2O buffer a minimum of two times ensured nearly complete isotope exchange. $H_2{}^{18}O$ were prepared in the same manner as their corresponding standard water samples, with the addition of several concentration and dilution cycles to exchange the $H_2{}^{16}O$-containing buffer with the $H_2{}^{18}O$-containing buffer. In **P** preparation, the exchange was performed on the diferrous enzyme in an anaerobic chamber. To prepare $H_2{}^{18}O$-containing buffer, 2 mL of standard buffer (50 mM Bicine, pH 9) was lyophilized for 24 h. The resulting salts were then dissolved in 2 mL $H_2{}^{18}O$ water in the anaerobic chamber.

Analytical Methods

Metabolite Analysis. To analyze products in the reaction of CmlI with substrate, 150 μL aliquots of **P** diluted to 100-300 μM were promptly transferred to pre-cooled Reacti-Vials with stir bars at 4 °C. The indicated equivalents of substrate were added to the stirring **P**. (Substrate stocks were 2-20 mM in 10% MeOH, 90% water, kept at 4 °C. Normal substrate addition was 1-15 μL, so the amount of MeOH added to the reaction was minimal). Substrate equivalents were calculated vs. concentration of **P** unless otherwise stated. The reactions were run for 10 min unless otherwise indicated, at which point they were quenched with 150 μL 5% TFA or 75 μL 10 M HCl/50 μL 7.5 M HCOONa/50 μL 10 M NaOH. The reaction mixture was centrifuged at 4 °C at maximum speed for 20 min to pellet the protein precipitate, and then the supernatant was transferred to a clean Eppendorf microcentrifuge tube and either stored at -80 °C or analyzed by HPLC immediately.

Under the highly acidic conditions of the quench procedure, NH(OH)-CAM converts to NO-CAM which may subsequently dimerize.[83] To control for this non-enzymatic conversion, some reactions were spin-quenched instead of acid-quenched by centrifuging an aliquot for 20 min in an Amicon Ultra-0.5 mL 10K (Millipore), washing the retentate with 150 μL of buffer, and centrifuging again for another 20 min. Some experimental procedures required an acid quench. After surveying several acid quench procedures, the 5.0% TFA acid quench was found to be the least damaging, with retention of >95% of CAM product and ~70% of the NO-CAM product.

HPLC. HPLC analysis was performed using a Waters 1525 binary HPLC pump and Waters 2487 dual λ absorbance detector with an Agilent Zorbax SB-C18 column. Products were monitored in dual wavelength mode at 280 nm and 316 nm. The method was isocratic 75% buffer A (water with 0.1% v/v formic acid) and 25% buffer B (MeOH with 0.1% v/v formic acid) for 15 min followed by a 5 min wash with buffer B at a flow rate of 2.5 mL/min. By this method, NH_2-CAM elutes at 1.2 min, NO-CAM at 11.2 min and CAM at 10 min.

UPLC/MSe and Analysis. Instrumentation for UPLC/MS^e analysis was a Waters Acquity UPLC with a Waters HSS T3 C_{18} 2.1 mm x 100 mm column (1.7 μm diameter particles) coupled to a Waters Synapt G2 HDMS quadrupole orthogonal acceleration time of flight mass

spectrometer (Waters Corp., Milford, MA USA). A 15 min linear gradient separation was run at a flow rate of 0.400 mL/min at 35 °C using A: water containing 0.1% v/v formic acid and B: acetonitrile containing 0.1% v/v formic acid: 3% B, 0 min to 1 min; 3% B to 97% B, 1 min to 9 min; 97% B, 9 min to 11 min; 97% B to 3% B, 11 min to 12 min; 3% B 12 min to 15 min. Spectra were collected in negative mode.

Determination of ^{18}O incorporation into product was complicated by the fact that the substrate and product both contain two Cl atoms, for which two common isotopes, ^{35}Cl and ^{37}Cl, are two mass units apart just as ^{16}O and ^{18}O. To establish a baseline for the isotope patterns, the reaction of **P** and NH_2-CAM was performed under an $^{16}O_2$ atmosphere in quadruplicate and the natural abundance at each m/z was noted. These were loaded into an excel spreadsheet to be iteratively subtracted from the value obtained from reactions with $^{18}O_2$. Under the these conditions, the retention time for CAM and NO-CAM was 4.5 min and the retention time for NH_2-CAM was 1.3 min. The m/z values for NH_2-CAM are 291.03, 293.03 and 295.03, for NO-CAM are 305.01, 307.01, 309.01 and 311.01, and for CAM are 321.01, 323.01, 325.01, 327.01 and 329.01.

Spectroscopic Methods

UV-visible Spectroscopy. Absorbance spectra were taken on an Agilent Cary 60 UV-Vis spectrophotometer at room temperature. For the titration of **P** with NH_2-CAM, **P** was prepared as described above at 500 µM concentration and stored in a quartz cuvette on ice. Small aliquots of a 1 mM NH_2-CAM solution in 50 mM Bicine buffer, pH 9 were added each representing approximately 0.05 equivalents relative to the starting CmlI-peroxo concentration. The optical spectrum was scanned and used to construct plots. About 3 % of the **P** decays spontaneously during the experiment. No correction was made for this loss. The end point of the reaction was analyzed by reverse phase HPLC and an authentic standard of CAM was run by the same HPLC method to confirm that the UV-Vis titration was producing CAM.

UV-Vis Stopped-Flow. Stopped-flow experiments were performed using an Applied Photophysics model SX.18MV stopped-flow device. Specific experiments and fitting procedures are described in the Kinetic Methods section.

Resonance Raman Studies. CmlI (2 mM) was reduced under anaerobic conditions with an excess amount of dithionite in the presence of 0.1 equivalent of methylviologen. Excess reductant and methylviologen were removed using a PD-10 desalting column (G-25, GE Healthcare) in an anaerobic chamber. The removal of methylviologen is essential as it can be photoreduced by the laser, which results in the reduction of the peroxo species and thus loss of rRaman signal. Aliquots of reduced CmlI from the same batch were exposed to either $^{16}O_2$ or $^{18}O_2$ at ~ 4 °C for several minutes. The samples were then flash-frozen with liquid nitrogen and kept at 77 K for future experiments. $^{16}O_2$ and $^{18}O_2$ samples were repeated three times. Multiple measurements were carried out for each sample. For each measurement, a ~ 70 μL aliquot of samples was thawed and transferred to flat-bottomed NMR quartz tubes and maintained at a temperature range of -10 °C to 10 °C. For the isotopically labeled samples, the tubes were sealed with septa and equilibrated with argon prior to sample transfer to minimize the exchange of the peroxo ligand with atmospheric dioxygen (this step was later determined to be unnecessary as the O_2 ligand does not exchange in the absence of substrate).

Resonance Raman experiments were performed on an Acton AM-506 spectrophotometer (1,200-groove grating) with a Princeton Instruments LN_CCD-1100-PB_UVAR detector cooled to -120 °C with liquid nitrogen. The 488 nm excitation line at 100 – 600 mW power was provided by a Spectra-Physics BeamLok 2060-KR-RS Argon ion laser, which is filtered out by a Kaiser Optical holographic super notch filter. Spectra were collected in 90° scattering geometry at resolution of 4 cm^{-1}, and referenced to indene. Multiple spectra were continuously collected over 10 or 20 minutes with each spectrum obtained from a 15-second exposure. Spectra within desired time range were added to improve the signal-to-noise ratio. Multiple measurements were performed for each CmlI-peroxo sample. GRAMS/AI (Thermo Galactic, Salem, NH) was utilized data processing.

EPR sample preparation and analysis. EPR spectra were collected using a Bruker Elexsys E-500 spectrometer equipped with a Bruker dual mode cavity and an Oxford ESR 910 liquid helium cryostat. Mixed valent CmlI was prepared via photoreduction of the diferric enzyme (1 mM) at 4 °C with 50 μM 5-deazaflavin in the presence of 10 mM phenazine methosulfate using a standard 100 W lamp. Mössbauer spectroscopy was performed as previously described.[88] Spectra were analyzed using the software WMOSS (SEE Co., Edina, MN).

Mössbauer sample preparation and analysis. Samples for Mössbauer analysis were removed at various points of the catalytic cycle in which ^{57}Fe-enriched CmlI replaced natural abundance enzyme. Samples include diferric (as-isolated), **P** and diferrous, all described previously, and samples from the catalytic walks, as described in the next section. To freeze the anaerobic samples, the Mössbauer cup containing the sample was placed in a large Reacti-Vial (Thermo Scientific) while still inside the anaerobic chamber and sealed. After removal from the chamber, the entire vial was promptly frozen in liquid nitrogen. The vial was unsealed for spectral studies.

Mössbauer spectra were recorded with home-built spectrometers using Janis Research Super-Varitemp dewars, which allowed studies in the temperature range from 1.5 to 200 K and applied magnetic fields up to 8.0 T. Mössbauer spectral simulations were performed using the WMOSS software package (SEE Co., Edina, MN). Isomer shifts are quoted relative to Fe metal at 298 K. All Mössbauer figures were prepared using SpinCount software.[162]

Obtaining Snapshots of the CmlI Catalytic Cycle

NH_2-CAM Catalytic Walk. All samples were kept at ~4 °C unless otherwise stated and all experiments were performed in 50 mM Bicine buffer pH 9. A sample of **P** (600 μM) was prepared as described above. A 200 μL aliquot was removed and an absorbance spectrum was taken. This sample was then left on the benchtop to decay; a spectrum was later taken to serve as the **P** decay control. The remaining **P** was degassed to remove excess O_2, first by purging with Ar gas for 20 min, and then by transferring to the anaerobic chamber and stirring for 10 min in the anaerobic atmosphere. After excess O_2 was removed, one equivalent of NH_2-CAM (freshly prepared in the anaerobic chamber, 10% MeOH, 90% water) was added and allowed to stir for 5 min. A 100 μL aliquot of this sample was removed and quenched in the anaerobic chamber with 100 μL 5% TFA for HPLC analysis. The remaining enzyme substrate mixture was transferred into a sealable cuvette and brought out of the anaerobic chamber. An absorbance spectrum was taken, after which the sample was exposed to a stream of O_2 for 2 min. The spectrum of the

resulting sample was taken and an aliquot was removed and quenched in equal volume 5% TFA for HPLC analysis.

NH(OH)-CAM and NO-CAM Catalytic Walks. Diferric resting state CmlI (560 μM) or **P** (300 μM, prepared as described above) was degassed first by purging with Ar gas for 20 min, and then by transferring to the anaerobic chamber and stirring for 10 min in the anaerobic atmosphere. After excess O_2 was removed, one equivalent of NH(OH)-CAM or NO-CAM (freshly prepared in the anaerobic chamber, 10% MeOH, 90% water) was added and allowed to stir for 5 min. A 100 μL aliquot of this sample was removed and quenched in the anaerobic chamber with 100 μL 5% TFA for HPLC analysis. The remaining enzyme substrate mixture was transferred into a sealable cuvette and brought out of the anaerobic chamber. An absorbance spectrum was taken, after which the sample was exposed to a stream of O_2 for 2 min. The spectrum of the resulting sample was taken and an aliquot was removed and quenched in equal volume 5% TFA for HPLC analysis.

Capturing the Oxidant in the Reaction of $CmlI^{red}$ with NO-CAM. Reduced CmlI (400 μM) was mixed 1:1 with reaction buffer (50 mM Bicine, pH 9) saturated with O_2 (1.8 mM at 4 °C) containing NO-CAM (4 mM). Rapid quenches used an Update 715 Ram Syringe Controller to mix and dispense the reactants at time points < 30 sec. The reaction mixture was dispensed onto rapidly spinning LN_2-cooled metal wheels of a home-built instrument. Contact with the cooled wheels causes the reaction solution to freeze instantly into a powder. The powder is then scrapped off into a LN_2 bath and packed into Mössbauer cups for analysis. Samples at time points > 30 seconds are mixed by a magnetic sir bar in a reaction vial and then frozen by hand. Reaction time points are chosen by inspecting the UV-vis trace of the formation and decay of the intermediate in question.

Determining Kinetic Trends and Constants

General Procedures. All stopped flow experiments were performed in 50 mM Bicine pH 9 at 4 °C. In reactions of the diferrous enzyme with O_2 and aryl-amine-derived substrates (including NH_2-CAM, NH(OH)-CAM and NO-CAM), CmlI was reduced as described above and then

loaded anaerobically using a Hamilton syringe to the stopped-flow device which had been previously scrubbed with dithionite and anaerobic buffer. Reactions of the pre-formed CmlI-peroxo complex with aryl-amine substrates were performed similarly, with the diferrous enzyme extensively oxygenated prior to loading the stopped flow syringe. The resultant traces were fit as described below.

Trace Fitting and Rate Constant Determination. The kinetic data were analyzed to extract reciprocal relaxation times (RRTs) using the nonlinear regression function of the Applied Photophysics ProData Viewer program. Each reaction time course was fit to a summed exponential expression, Eq. 1, which is appropriate for a series of first order or pseudo-first order reactions.[163] In this equation, Abs_t is the observed absorbance at time t, Amp_i is the observed amplitude for exponential phase *i*, τ_i is the relaxation time for phase *i*, and Abs_{inf} is the final absorbance at the end of the reaction. For a linear series of *n* reaction steps, *n* phases are required for the fit. Fitting statistics were reported by the fitting program, and each reaction was repeated at least 10 times to determine the average fitting parameters and errors.

$$Abs_t = (\sum_{i=1}^{n} Amp_i\, e^{-\frac{t}{\tau i}}) + Abs_{inf} \qquad \text{(Eq. 1)}$$

For a two-step reaction where the first step is fast reversible binding, a hyperbolic dependence of the $1/\tau_{obs}$ on substrate or O_2 concentration may apply if the observable step that follows is comparatively slow: [164]

$$\text{E} + \text{ligand} \underset{k_{-1}}{\overset{k_1}{\rightleftarrows}} \text{E·ligand} \underset{k_{-2}}{\overset{k_2}{\rightleftarrows}} \text{E-ligand'} \qquad \text{(Eq. 2)}$$

Plots of $1/\tau_{obs}$ versus either substrate or oxygen concentration were fit to the hyperbolic function below using Origin:

$$\frac{1}{\tau_{obs}} = \frac{k_2[\text{ligand}]}{(\frac{k_{-1}}{k_1})+[\text{ligand}]} + k_{-2} \qquad \text{(Eq. 3)}$$

The parameters of the equation yield the apparent K_D for the binding reaction (k_{-1}/k_1) and forward and reverse rate constants for observable conversion which follows binding. The accuracy of the

K_d value depends upon how closely the binding reaction approaches rapid equilibrium, and specifically, whether k_{-1} is >> than k_2.

Extraction of the rate constants from the sum and product plots of the RRTs (as in Chapter 4, Figure 4-18) was performed using previously described methods.[164-165] Three relaxations are observed in the transient reaction implying that there are at least three steps in the reaction. The first two phases have a clear dependence on substrate concentration. The nonlinear dependence on substrate concentration of the second relaxation is consistent with a sequential rather than parallel sequence of steps. Moreover, a nonlinear substrate dependence on one phase would only be observed if the first step in the reaction in which substrate binds is reversible. The final step is unlikely to be reversible because the reaction observed involves the cleavage of an O-O bond and the subsequent insertion of an O atom into an N-H bond. This leads to the following initial model for the reaction with O_2 and substrate:

$$E^{red} + O_2 \underset{k_{-1}}{\overset{k_1}{\rightleftarrows}} \boldsymbol{P} + NH_2 - CAM \underset{k_{-2}}{\overset{k_2}{\rightleftarrows}} E^{ox} + NH(OH) - CAM \qquad \text{(Eq. 4)}$$

The rate constants for the individual steps cannot be determined directly from the exponential fits due to mixing of the relaxations through the reversible step(s). Under the assumption that the final irreversible step is slow, the analysis can be performed by solving a series of differential rate equations describing the first two steps of the reaction. This analysis shows that the first and second RRTs correspond to the negative roots of a quadratic equation given by Equations 5 and 6, where S is any substrate:

$$\lambda^2 + (k_2[S] + k_{-2} + k_1 + k_{-1})\lambda + (k_2[S](k_1 + k_{-1}) + k_{-2}k_{-1}) \qquad \text{(Eq. 5)}$$

$$\frac{1}{\tau 1}, \frac{1}{\tau 2} = \frac{1}{2}\{(k_2[S] + k_{-2} + k_1 + k_{-1}) \pm \sqrt{[(k_2[S] + k_{-2} + k_1 + k_{-1})^2 - 4 + (k_2[S](k_1 + k_{-1}) + k_{-2}k_{-1})]}\} \qquad \text{(Eq. 6)}$$

The rate constants may thus be extracted using the following relationships:

$$\frac{1}{\tau 1} + \frac{1}{\tau 2} = k_2[S] + k_{-2} + k_1 + k_{-1} \qquad \text{(Eq. 7)}$$

$$\frac{1}{\tau 1 \tau 2} = k_{-2}(k_1 + k_{-1})[S] + k_1 k_2 \qquad \text{(Eq. 8)}$$

The slopes and intercepts in the plots of the sum or product of the RRT vs. [S] can then be used to calculate the rate constants.

Numerical Integration and Simulation of Kinetic Data. KinTek Explorer (KinTek Corporation, Snow Shoe, PA) was used to simulate reactions. A model for the reaction course is built based on the number of phases observed in optical data for a particular reaction and on previously established information regarding the proposed steps. Optical absorption traces and experimentally determined rate constants are imported and fit to the model to test the model, provide refined rate constants, and determine how changing rate constants changes the shape and trend of the traces.

Reactions to Monitor P Formation. These reactions were monitored at 300 nm (no CAM present) or 320 nm (CAM present) with ~ 40 μM CmlI. (All concentrations are final, post-mix concentrations. Thus, in this case the syringe contained ~80 μM CmlI, which was diluted to ~ 40 μM when mixed 1:1 by the stopped-flow instrument). One syringe was loaded with diferrous CmlI and the second with buffer containing 3-30 equivalents O_2 (pseudo-first order conditions, ~100 – 900 μM). The reactions with CAM used 10 equivalents (400 μM) CAM in the O_2 syringe.

Reactions with NH_2-CAM. All reactions with NH_2-CAM were monitored at 480 nm with ~ 200 μM CmlI. In reactions in which both **P** formation and decay were monitored, one syringe was loaded with diferrous CmlI and the second with buffer containing either ~900 μM O_2 (pseudo-first order conditions) or ~200 μM O_2 (stoichiometric conditions). In reactions where only **P** decay was monitored, **P** was formed in-syringe by loading 800 μM diferrous CmlI into a gas tight syringe, removing it from the anaerobic chamber and cooling it to 4 °C on ice (~ 5 min). An equal volume of O_2-saturated buffer was then introduced into the syringe to dilute the enzyme to 400 μM, the syringe was inverted several times to mix, and then loaded onto the stopped-flow instrument. This method maximized **P** formation and minimized pre-reaction **P** decay. Substrate (5- 40 equivalents or 1-8 mM) was loaded either anaerobically into the enzyme syringe, or into the O_2 syringe, as the experiment dictated.

Reactions with NH(OH)-CAM. All reactions with NH(OH)-CAM were monitored at 390 nm with ~ 40 μM CmlI. One syringe contained anaerobic diferric CmlI and the second contained 5-300 equivalents NH(OH)-CAM in anaerobic buffer.

Reactions with NO-CAM. All reactions with NO-CAM were monitored at 480 nm with ~ 200 μM CmlI. Methods are the same as for reaction with NH_2-CAM (above).

Oxygen Isotope Tracing Methods

Oxygen Isotope Incorporation Experiments. **P** was prepared as above, with appropriate O_2 isotope. For the reactions in $H_2{}^{18}O$, labeled water was introduced when the enzyme was in the diferrous state by three cycles of anaerobic concentration and dilution with 50 mM Bicine buffer, pH 9, prepared in $H_2{}^{18}O$. For the reactions with ^{18}O-**P**, the vial containing the intermediate was brought into an anaerobic chamber and substrate was added. The sealed vial with **P**-substrate complex was brought out of the chamber and kept under a positive pressure of $^{18}O_2$. Reactions were run for 10 min at 4 °C and then acid-quenched. After centrifugation to remove protein precipitate, the supernatant was transferred to an LCMS vial. Reactions of ^{16}O-**P** were performed similarly expect that the substrate was introduced on the benchtop.

Experiment to Evaluate Exchange of CmlI-Peroxo with Atmospheric O_2. 1 mL of ^{18}O-**P** (200 μM) was prepared as above and stirred on ice for the duration of the experiment. A stream of $^{16}O_2$ was applied over the sample. 100 μL aliquots were removed at time points from 1 to 90 min and reacted with 0.3 equivalents of NH_2-CAM. Reactions were run for 10 min and then quenched and prepared for LCMS analysis as described above.

Exchange of Products from the Active Site. $^{18}O_2$-**P** (200 μM) was prepared as above, degassed to remove excess O_2, and equilibrated in an anaerobic chamber before 1x NH_2-CAM (200 μM) was added. After a 20 s incubation, one equivalent of $N^{16}O$-CAM (200 μM) was added. The sample was then quickly put under an $^{18}O_2$ headspace and allowed to react for 10 min. Samples were acid quenched and analyzed by LCMS. Control samples were made by adding buffer instead of NO-CAM.

References

1. Bekker, A.; Holland, H. D.; Wang, P. L.; Rumble, D.; Stein, H. J.; Hannah, J. L.; Coetzee, L. L.; Beukes, N. J., Dating the rise of atmospheric oxygen. *Nature* **2004,** *427* (6970), 117-120.
2. Sessions, A. L.; Doughty, D. M.; Welander, P. V.; Summons, R. E.; Newman, D. K., The continuing puzzle of the great oxidation event. *Curr Biol* **2009,** *19* (14), R567-74.
3. Raymond, J.; Segre, D., The effect of oxygen on biochemical networks and the evolution of complex life. *Science* **2006,** *311* (5768), 1764-7.
4. Catling, D. C.; Glein, C. R.; Zahnle, K. J.; McKay, C. P., Why O_2 is required by complex life on habitable planets and the concept of planetary "oxygenation time". *Astrobiology* **2005,** *5* (3), 415-438.
5. Wood, P. M., The potential diagram for oxygen at pH 7. *Biochem. J.* **1988,** *253* (1), 287-9
6. Stenkamp, R. E.; Sieker, L. C.; Jensen, L. H.; McCallum, J. D.; Sanders-Loehr, J., Active site structures of deoxyhemerythrin and oxyhemerythrin. *Proc. Natl. Acad. Sci. USA* **1985,** *82*, 713-716.
7. Fox, B. G.; Lyle, K. S.; Rogge, C. E., Reactions of the diiron enzyme stearoyl-acyl carrier protein desaturase. *Acc. Chem. Res.* **2004,** *37* (7), 421-429.
8. Wallar, B. J.; Lipscomb, J. D., Dioxygen activation by enzymes containing binuclear non-heme iron clusters. *Chem. Rev.* **1996,** *96* (7), 2625-2657.
9. Lipscomb, J. D., Mechanism of extradiol aromatic ring-cleaving dioxygenases. *Curr. Opin. Struct. Biol.* **2008,** *18* (6), 644-649.
10. Shanklin, J.; Achim, C.; Schmidt, H.; Fox, B. G.; Münck, E., Mössbauer studies of alkane omega-hydroxylase - Evidence for a diiron cluster in an integral-membrane enzyme. *Proc. Natl. Acad. Sci. USA* **1997,** *94* (7), 2981-2986.
11. Newman, L. M.; Wackett, L. P., Purification and characterization of toluene 2-monooxygenase from Burkholderia cepacia G4. *Biochemistry* **1995,** *34* (43), 14066-76.
12. Byrne, A. M.; Kukor, J. J.; Olsen, R. H., Sequence analysis of the gene cluster encoding toluene-3-monooxygenase from *Pseudomonas pickettii* Pko1. *Gene* **1995,** *154* (1), 65-70.
13. Sazinsky, M. H.; Bard, J.; Di Donato, A.; Lippard, S. J., Crystal structure of the toluene/o-xylene monooxygenase hydroxylase from *Pseudomonas stutzeri* OX1. Insight into the substrate specificity, substrate channeling, and active site tuning of multicomponent monooxygenases. *J. Biol. Chem.* **2004,** *279* (29), 30600-30610.
14. Makris, T. M.; Chakrabarti, M.; Münck, E.; Lipscomb, J. D., A family of diiron monooxygenases catalyzing amino acid beta-hydroxylation in antibiotic biosynthesis. *Proc. Natl. Acad. Sci. USA* **2010,** *107* (35), 15391-15396.
15. Vu, V. V.; Emerson, J. P.; Martinho, M.; Kim, Y. S.; Münck, E.; Park, M. H.; Que, L., Jr., Human deoxyhypusine hydroxylase, an enzyme involved in regulating cell growth, activates O_2 with a nonheme diiron center. *Proc. Natl. Acad. Sci. USA* **2009,** *106* (35), 14814-14819.
16. Lu, T.-T.; Lee, S. J.; Apfel, U.-P.; Lippard, S. J., Aging-associated enzyme human clock-1: substrate-mediated reduction of the diiron center for 5-demethoxyubiquinone hydroxylation. *Biochemistry* **2013,** *52*, 2236-44.
17. Mathevon, C.; Pierrel, F.; Oddou, J.-L.; Garcia-Serres, R.; Blondin, G.; Latour, J.-M.; Menage, S.; Gambarelli, S.; Fontecave, M.; Atta, M., tRNA-modifying MiaE protein from *Salmonella typhimurium* is a nonheme diiron monooxygenase. *Proc. Natl. Acad. Sci. USA* **2007,** *104* (33), 13295-13300.

18. He, J.; Hertweck, C., Biosynthetic origin of the rare nitroaryl moiety of the polyketide antibiotic aureothin: Involvement of an unprecedented N-oxygenase. *J. Am. Chem. Soc.* **2004,** *126* (12), 3694-3695.
19. Lu, H. G.; Chanco, E.; Zhao, H. M., CmlI is an N-oxygenase in the biosynthesis of chloramphenicol. *Tetrahedron* **2012,** *68* (37), 7651-7654.
20. Stubbe, J., Ribonucleotide reductase. *Adv. Enzymol. and Related Areas of Mol. Biol.* **1990,** *63*, 349-419.
21. Aukema, K. G.; Makris, T. M.; Stoian, S. A.; Richman, J. E.; Münck, E.; Lipscomb, J. D.; Wackett, L. P., Cyanobacterial aldehyde deformylase oxygenation of aldehydes yields n - 1 aldehydes and alcohols in addition to alkanes. *ACS Catal.* **2013,** *3* (10), 2228-2238.
22. Brown, C. D.; Neidig, M. L.; Neibergall, M. B.; Lipscomb, J. D.; Solomon, E. I., VTVH-MCD and DFT studies of thiolate bonding to $\{FeNO\}^7/\{FeO_2\}^8$ complexes of isopenicillin N synthase: Substrate determination of oxidase versus oxygenase activity in nonheme Fe enzymes. *J. Am. Chem. Soc.* **2007,** *129* (23), 7427-7438.
23. McSorley, F. R.; Wyatt, P. B.; Martinez, A.; DeLong, E. F.; Hove-Jensen, B.; Zechel, D. L., PhnY and PhnZ comprise a new oxidative pathway for enzymatic cleavage of a carbon-phosphorus bond. *J. Am. Chem. Soc.* **2012,** *134* (20), 8364-7.
24. Park, M. H.; Nishimura, K.; Zanelli, C. F.; Valentini, S. R., Functional significance of eIF5A and its hypusine modification in eukaryotes. *Amino Acids* **2010,** *38* (2), 491-500.
25. Schirmer, A.; Rude, M. A.; Li, X.; Popova, E.; del Cardayre, S. B., Microbial synthesis of alkanes. *Science* **2010,** *329*, 559-562.
26. Brazeau, B. J.; Lipscomb, J. D., Kinetics and activation thermodynamics of methane monooxygenase compound Q formation and reaction with substrates. *Biochemistry* **2000,** *39* (44), 13503-13515.
27. Sturgeon, B. E.; Burdi, D.; Chen, S.; Huynh, B.-H.; Edmondson, D. E.; Stubbe, J.; Hoffman, B. M., Reconsideration of **X**, the diiron intermediate formed during cofactor assembly in *E. coli* ribonucleotide reductase. *J. Am. Chem. Soc.* **1996,** *118*, 7551-7557.
28. Krebs, C.; Fujimori, D. G.; Walsh, C. T.; Bollinger, J. M., Jr., Non-heme Fe(IV)-oxo intermediates. *Acc. Chem. Res.* **2007,** *40* (7), 484-492.
29. McDonald, A. R.; Que Jr, L., High-valent nonheme iron-oxo complexes: Synthesis, structure, and spectroscopy. *Coord. Chem. Rev.* **2013,** *257* (2), 414-428.
30. Makris, T. M.; von Koenig, K.; Schlichting, I.; Sligar, S. G., The status of high-valent metal oxo complexes in the P450 cytochromes. *J. Inorg. Biochem.* **2006,** *100* (4), 507-518.
31. Banerjee, R.; Proshlyakov, Y.; Lipscomb, J. D.; Proshlyakov, D. A., Structure of the key species in the enzymatic oxidation of methane to methanol. *Nature* **2015,** *518* (7539), 431-434.
32. Banerjee, R.; Meier, K. K.; Münck, E.; Lipscomb, J. D., Intermediate P* from soluble methane monooxygenase contains a diferrous cluster. *Biochemistry* **2013,** *52* (25), 4331-4342.
33. Lee, S. K.; Lipscomb, J. D., Oxygen activation catalyzed by methane monooxygenase hydroxylase component: Proton delivery during the O-O bond cleavage steps. *Biochemistry.* **1999,** *38* (14), 4423-4432.
34. Liu, K. E.; Wang, D.; Huynh, B. H.; Edmondson, D. E.; Salifoglou, A.; Lippard, S. J., Spectroscopic detection of intermediates in the reaction of dioxygen with the reduced methane monooxygenase hydroxylase from *Methylococcus capsulatus* (Bath). *J. Am. Chem. Soc.* **1994,** *116*, 7465-7466.

35. Lee, S. K.; Nesheim, J. C.; Lipscomb, J. D., Transient intermediates of the methane monooxygenase catalytic cycle. *J. Biol. Chem.* **1993,** *268* (29), 21569-21577.
36. Tshuva, E. Y.; Lippard, S. J., Synthetic models for non-heme carboxylate-bridged diiron metalloproteins: strategies and tactics. *Chem. Rev.* **2004,** *104* (2), 987-1011.
37. Han, W. G.; Noodleman, L., Structural model studies for the peroxo intermediate P and the reaction pathway from P-->Q of methane monooxygenase using broken-symmetry density functional calculations. *Inorg. Chem.* **2008,** *47* (8), 2975-86.
38. Murray, L. J.; Naik, S. G.; Ortillo, D. O.; Garcia-Serres, R.; Lee, J. K.; Huynh, B. H.; Lippard, S. J., Characterization of the arene-oxidizing intermediate in ToMOH as a diiron(III) species. *J. Am. Chem. Soc.* **2007,** *129* (46), 14500-14510.
39. Song, W. J.; Behan, R. K.; Naik, S. G.; Huynh, B. H.; Lippard, S. J., Characterization of a peroxodiiron(III) intermediate in the T201S Variant of toluene/o-xylene monooxygenase hydroxylase from *Pseudomonas sp.* OX1. *J. Am. Chem. Soc.* **2009,** *131* (17), 6074-6075.
40. Skulan, A., J.; Brunold, T., C.; Baldwin, J.; Saleh, L.; Bollinger, J. M., Jr.; Solomon, E., I., Nature of the peroxo intermediate of the W48F/D84E ribonucleotide reductase variant: implications for O_2 activation by binuclear non-heme iron enzymes. *J. Am. Chem. Soc.* **2004,** *126* (28), 8842-55.
41. Bollinger, J. M., Jr.; Krebs, C.; Vicol, A.; Chen, S.; Ley, B. A.; Edmondson, D. E.; Huynh, B. H., Engineering the diiron site of *Escherichia coli* ribonucleotide reductase protein R2 to accumulate an intermediate similar to H_{peroxo}, the putative peroxodiiron(III) complex from the methane monooxygenase catalytic cycle. *J. Am. Chem. Soc.* **1998,** *120* (5), 1094-1095.
42. Moenne-Loccoz, P.; Baldwin, J.; Ley, B. A.; Loehr, T. M.; Bollinger, J. M., Jr., O_2 activation by non-heme diiron proteins: identification of a symmetric μ-1,2-peroxide in a mutant of ribonucleotide reductase. *Biochemistry* **1998,** *37* (42), 14659-63.
43. Broadwater, J. A.; Achim, C.; Münck, E.; Fox, B. G., Mössbauer studies of the formation and reactivity of a quasi-stable peroxo intermediate of stearoyl-acyl carrier protein Δ(9)-desaturase. *Biochemistry.* **1999,** *38* (38), 12197-12204.
44. Jasniewski, A. J.; Engstrom, L. M.; Vu, V. V.; Park, M. H.; Que, L., X-ray absorption spectroscopic characterization of the diferric-peroxo intermediate of human deoxyhypusine hydroxylase in the presence of its substrate eIF5a. *J. Biol. Inorg. Chem.* **2016,** *21*, 605-618.
45. Han, Z.; Sakai, N.; Boettger, L. H.; Klinke, S.; Hauber, J.; Trautwein, A. X.; Hilgenfeld, R., Crystal structure of the peroxo-diiron(III) intermediate of deoxyhypusine hydroxylase, an oxygenase involved in hypusination. *Structure* **2015,** *23* (5), 882-892.
46. Pandelia, M. E.; Li, N.; Noergaard, H.; Warui, D. M.; Rajakovich, L. J.; Chang, W.-c.; Booker, S. J.; Krebs, C.; Bollinger, J. M., Jr., Substrate-triggered addition of dioxygen to the diferrous cofactor of aldehyde-deformylating oxygenase to form a diferric-peroxide intermediate. *J. Am. Chem. Soc.* **2013,** *135* (42), 15801-15812.
47. Bailey, L. J.; Fox, B. G., Crystallographic and catalytic studies of the peroxide-shunt reaction in a diiron hydroxylase. *Biochemistry* **2009,** *48* (38), 8932-8939.
48. Knoot, C. J.; Kovaleva, E. G.; Lipscomb, J. D., Crystal structure of CmlI, the arylamine oxygenase from the chloramphenicol biosynthetic pathway. *J. Biol. Inorg. Chem.* **2016,** *21*, 589-603.
49. Broadwater, J. A.; Ai, J.; Loehr, T. M.; Sanders-Loehr, J.; Fox, B. G., Peroxodiferric Intermediate of stearoyl-acyl carrier protein Δ^9 desaturase: Oxidase reactivity during single turnover and implications for the mechanism of desaturation. *Biochemistry* **1998,** *37* (42), 14664-14671.

50. Yun, D.; Garcia-Serres, R.; Chicalese, B. M.; An, Y. H.; Huynh, B. H.; Bollinger, J. M., Jr., (μ-1,2-peroxo)diiron(III/III) complex as a precursor to the diiron(III/IV) intermediate X in the assembly of the iron-radical cofactor of ribonucleotide reductase from mouse. *Biochemistry* **2007,** *46* (7), 1925-1932.
51. Lyle, K. S.; Moeenne-Loccoz, P.; Ai, J.; Sanders-Loehr, J.; Loehr, T. M.; Fox, B. G., Resonance Raman studies of the stoichiometric catalytic turnover of a substrate-stearoyl-acyl carrier protein Δ^9 desaturase complex. *Biochemistry* **2000,** *39* (34), 10507-10513.
52. Makris, T. M.; Vu, V. V.; Meier, K. K.; Komor, A. J.; Rivard, B. S.; Münck, E.; Que, L., Jr.; Lipscomb, J. D., An unusual peroxo intermediate of the arylamine oxygenase of the chloramphenicol biosynthetic pathway. *J. Am. Chem. Soc.* **2015,** *137* (4), 1608-1617.
53. Korboukh, V. K.; Li, N.; Barr, E. W.; Bollinger, J. M., Jr.; Krebs, C., A long-lived, substrate-hydroxylating peroxodiiron(III/III) intermediate in the amine oxygenase, AurF, from *Streptomyces thioluteus*. *J. Am. Chem. Soc.* **2009,** *131* (38), 13608-13609.
54. Ookubo, T.; Sugimoto, H.; Nagayama, T.; Masuda, H.; Sato, T.; Tanaka, K.; Maeda, Y.; Okawa, H.; Hayashi, Y.; Uehara, A.; Suzuki, M., *cis*-μ-1,2-peroxo diiron complex: Structure and reversible oxygenation. *J. Am. Chem. Soc.* **1996,** *118*, 701-702.
55. Menage, S.; Brennan, B. A.; Juarez-Garcia, C.; Münck, E.; Que, L., Jr., Models for iron-oxo proteins: Dioxygen binding to a diferrous complex. *J. Am. Chem. Soc.* **1990,** *112*, 6423-6425.
56. Dong, Y.; Yan, S.; Young, V. G., Jr.; Que, L., Jr., The crystal structure of a synthetic nonheme diiron-O_2 adduct: Insight into oxygen activation. *Angew. Chem. Int. Ed.* **1996,** *35* (6), 618-620.
57. Kim, K.; Lippard, S. J., Structure and Mössbauer spectrum of a (μ-1,2-peroxo)bis(μ-carboxylato)diiron(III) model for the peroxo intermediate in the methane monooxygenase hydroxylase reaction cycle. *J. Am. Chem. Soc.* **1996,** *118*, 4914-4915.
58. Zhang, X.; Furutachi, H.; Fujinami, S.; Nagatomo, S.; Maeda, Y.; Watanabe, Y.; Kitagawa, T.; Suzuki, M., Structural and spectroscopic characterization of (μ-hydroxo or μ-oxo)(μ-peroxo)diiron(III) complexes: Models for peroxo intermediates of non-heme diiron proteins. *J. Am. Chem. Soc.* **2005,** *127* (3), 826-827.
59. Parry, R.; Nishino, S.; Spain, J., Naturally-occurring nitro compounds. *Nat. Prod. Rep.* **2011,** *28* (1), 152-167.
60. Schlunzen, F.; Zarivach, R.; Harms, J.; Bashan, A.; Tocilj, A.; Albrecht, R.; Yonath, A.; Franceschl, F., Structural basis for the interaction of antibiotics with the peptidyl transferase center in eubacteria. *Nature* **2001,** *413* (6858), 814-821.
61. Fernandez, M.; Conde, S.; de la Torre, J.; Molina-Santiago, C.; Ramos, J.-L.; Duque, E., Mechanisms of Resistance fo Chloramphenicol in *Pseudemonas putida* KT2440. *Antimicrobial Agents and Chemotherapy* **2012,** *56* (2), 1001 - 1009.
62. Savini, V.; Catavitello, C.; D'Aloisio, M.; Balbinot, A.; Astolfi, D.; Masciarelli, G.; Pompilio, A.; Di Bonaventura, G.; D'Antonio, D., Chloramphenicol and rifampin may be the only options against *Stenotrophomonas maltophilia.* A tale of a colonized bladder device in a patient with myelofibrosis. *Infez. Med.* **2010,** *18* (3), 193-197.
63. He, J.; Magarvey, N.; Piraee, M.; Vining, L. C., The gene cluster for chloramphenicol biosynthesis in *Streptomyces venezuelae* ISP5230 includes novel shikimate pathway homologues and a monomodular non-ribosomal peptide synthetase gene. *Microbiology* **2001,** *147* (10), 2817-2829.
64. Piraee, M.; White, R. L.; Vining, L. C., Biosynthesis of the dichloroacetyl component of chloramphenicol in *Streptomyces venezuelae* ISP5230: Genes required for halogenation. *Microbiology* **2004,** *150* (1), 85-94.

65. Fernández-Martínez, L. T.; Borsetto, C.; Gomez-Escribano, J. P.; Bibb, M. J.; Al-Bassam, M. M.; Chandra, G.; Bibb, M. J., New Insights into chloramphenicol biosynthesis in *Streptomyces venezuelae* ATCC 10712. *Antimicrob. Agents Chemother.* **2014,** *58* (12), 7441-7450.
66. Lee, J.; Simurdiak, M.; Zhao, H., Reconstitution and characterization of aminopyrrolnitrin oxygenase, a Rieske N-oxygenase that catalyzes unusual arylamine oxidation. *J. Biol. Chem.* **2005,** *280*, 36719-27.
67. Zocher, G.; Winkler, R.; Hertweck, C.; Schulz, G. E., Structure and action of the N-oxygenase AurF from *Streptomyces thioluteus*. *J. Mol. Biol.* **2007,** *373* (1), 65-74.
68. Indest, K. J.; Eberly, J. O.; Hancock, D. E., Expression and characterization of an N-oxygenase from *Rhodococcus jostii* RHAI. *J. Gen. Appl. Microbiol.* **2015,** *61* (6), 217-223.
69. Platter, E.; Lawson, M.; Marsh, C.; Sazinsky, M. H., Characterization of a non-ribosomal peptide synthetase-associated diiron arylamine N-oxygenase from *Pseudomonas syringae* pv. *phaseolicola*. *Arch. Biochem. Biophys.* **2011,** *508* (1), 39-45.
70. Kelly, W. L.; Townsend, C. A., Mutational analysis of *nocK* and *nocL* in the nocardicin A producer *Nocardia uniformis*. *J. Bacteriol.* **2005,** *187* (2), 739-746.
71. Thoden, J. B.; Branch, M. C.; Zimmer, A. L.; Bruender, N. A.; Holden, H. M., Active site architecture of a sugar N-oxygenase. *Biochemistry* **2013,** *52* (19), 3191-3193.
72. Chang, A.; Hartmann, T., Solubilization and characterization of a senecionine N-oxygenase from *Crotalaria scassellatii* seedlings. *Phytochemistry* **1998,** *49* (7), 1859-1866.
73. Lang, D. H.; Yeung, C. K.; Peter, R. M.; Ibarra, C.; Gasser, R.; Itagaki, K.; Philpot, R. M.; Rettie, A., Isoform specificity of trimethylamine N-oxygenation by human flavin-containing monooxygenase (FMO) and P450 enzymes: Selective catalysis by FMO3. *Biochem. Pharmacol.* **1998,** *56* (8), 1005-1012.
74. Hirata, Y.; Nakata, H.; Yamada, K.; Okuhara, K.; Naito, T., Structure of aureothin, a nitro compound obtained from *Streptomyces thioluteus*. *Tetrahedron* **1961,** *14*, 252-74.
75. Simurdiak, M.; Lee, J.; Zhao, H., A new class of arylamine oxygenases: evidence that p-aminobenzoate N-oxygenase (AurF) is a di-iron enzyme and further mechanistic studies. *ChemBioChem* **2006,** *7* (8), 1169-1172.
76. Winkler, R.; Zocher, G.; Richter, I.; Friedrich, T.; Schulz, G. E.; Hertweck, C., A binuclear manganese cluster that catalyzes radical-mediated N-oxygenation. *Angew. Chem. Int. Ed.* **2007,** *46* (45), 8605-8608.
77. Krebs, C.; Matthews, M. L.; Jiang, W.; Bollinger, J. M., Jr., AurF from *Streptomyces thioluteus* and a possible new family of manganese/iron oxygenases. *Biochemistry* **2007,** *46* (37), 10413-10418.
78. Choi, Y. S.; Zhang, H.; Brunzelle, J. S.; Nair, S. K.; Zhao, H., In vitro reconstitution and crystal structure of p-aminobenzoate N-oxygenase (AurF) involved in aureothin biosynthesis. *Proc. Natl. Acad. Sci. USA.* **2008,** *105* (19), 6858-6863.
79. Reem, R. C.; McCormick, J. M.; Richardson, D. E.; Devlin, F. J.; Stephens, P. J.; Musselman, R. L.; Solomon, E. I., Spectroscopic studies of the coupled binuclear ferric active site in methemerythrins and oxyhemerythrin: the electronic structure of each iron center and the iron-oxo and iron-peroxide bonds. *J. Am. Chem. Soc.* **1989,** *111*, 4688-4704.
80. Darchen, A.; Moinet, C., Observation d'une N-phényl N,N-dihydroxylamine lors de la réduction d'un mononitrobenzène. *J. Electroanal. Chem. Interfacial Electrochem.* **1975,** *61* (3), 373-375.

81. Laviron, E.; Rouillier, L., The reduction mechanism of aromatic nitro compounds in aqueous medium: Part I. Reduction to dihydroxylamines between pH 0 and 5. *J. Electroanal. Chem.* **1990,** *288* (1), 165-175.
82. Lacasse, R.; Meunier-Prest, P.; Laviron, E., The reducation mechanism of aromatic nitro compounds in aqueous medium. Part IV. The reduction of p-nitrobenophenone between H = -5 and pH 14. *J. Electroanal. Chem.* **1994,** *375*, 263-274.
83. Winkler, R.; Hertweck, C., Sequential enzymatic oxidation of aminoarenes to nitroarenes via hydroxylamines. *Angew. Chem. Int. Ed.* **2005,** *44* (26), 4083-4087.
84. Lee, J.; Zhao, H., Mechanistic studies on the conversion of arylamines into arylnitro compounds by aminopyrrolnitrin oxygenase: identification of intermediates and kinetic studies. *Angew. Chem. Int. Ed.* **2006,** *45*, 622-5.
85. Li, N.; Korboukh, V. K.; Krebs, C.; Bollinger, J. M., Jr., Four-electron oxidation of p-hydroxylaminobenzoate to p-nitrobenzoate by a peroxodiferric complex in AurF from *Streptomyces thioluteus*. *Proc. Natl. Acad. Sci. USA* **2010,** *107* (36), 15722-7.
86. Entwistle, I. D.; Gilkerson, T.; Johnstone, R. A. W.; Telford, R. P., Rapid catalytic transfer reduction of aromatic nitro compounds to hydroxylamines. *Tetrahedron* **1978,** *34* (2), 213-215.
87. Pilkington, S. J.; Dalton, H., Soluble methane monooxygenase from *Methylococcus capsulatus* (Bath). *Methods Enzymol.* **1990,** *188*, 181-190.
88. Makris, T. M.; Chakrabarti, M.; Münck, E.; Lipscomb, J. D., A family of diiron monooxygenases catalyzing amino acid beta-hydroxylation in antibiotic biosynthesis. *Proc. Natl. Acad. Sci. U.S.A.* **2010,** *107* (35), 15391-6.
89. Vu, V. V.; Emerson, J. P.; Martinho, M.; Kim, Y. S.; Münck, E.; Park, M. H.; Que, L., Jr., Human deoxyhypusine hydroxylase, an enzyme involved in regulating cell growth, activates O_2 with a nonheme diiron center. *Proc. Natl. Acad. Sci. U.S.A.* **2009,** *106* (35), 14814-14819.
90. Wallar, B. J.; Lipscomb, J. D., Dioxygen activation by enzymes containing binuclear non-heme iron clusters. *Chem. Rev.* **1996,** *96* (7), 2625-2657.
91. Tinberg, C. E.; Lippard, S. J., Dioxygen activation in soluble methane monooxygenase. *Acc. Chem. Res.* **2011,** *44* (4), 280-288.
92. Moenne-Loccoz, P.; Baldwin, J.; Ley, B. A.; Loehr, T. M.; Bollinger, J. M., Jr., O_2 activation by non-heme diiron proteins: identification of a symmetric µ-1,2-peroxide in a mutant of ribonucleotide reductase. *Biochemistry* **1998,** *37* (42), 14659-63.
93. Beauvais, L. G.; Lippard, S. J., Reactions of the peroxo intermediate of soluble methane monooxygenase hydroxylase with ethers. *J. Am. Chem. Soc.* **2005,** *127* (20), 7370-7378.
94. Lee, S.-K.; Nesheim, J. C.; Lipscomb, J. D., Transient intermediates of the methane monooxygenase catalytic cycle. *J. Biol. Chem.* **1993,** *268* (29), 21569-21577.
95. Lee, S. K.; Fox, B. G.; Froland, W. A.; Lipscomb, J. D.; Münck, E., A transient intermediate of the methane monooxygenase catalytic cycle containing a Fe(IV)Fe(IV) cluster. *J. Am. Chem. Soc.* **1993,** *115*, 6450-6451.
96. Shu, L.; Nesheim, J. C.; Kauffmann, K.; Münck, E.; Lipscomb, J. D.; Que, L., Jr., An $Fe(IV)_2O_2$ diamond core structure for the key intermediate Q of methane monooxygenase. *Science* **1997,** *275* (5299), 515-518.
97. Bollinger, J. M., Jr.; Edmondson, D. E.; Huynh, B. H.; Filley, J.; Norton, J. R.; Stubbe, J., Mechanism of assembly of the tyrosyl radical-dinuclear iron cluster cofactor of ribonucleotide reductase. *Science* **1991,** *253* (5017), 292-298.

98. Baldwin, J.; Krebs, C.; Saleh, L.; Stelling, M.; Huynh, B. H.; Bollinger, J. M., Jr.; Riggs-Gelasco, P., Structural characterization of the peroxodiiron(III) intermediate generated during oxygen activation by the W48A/D84E variant of ribonucleotide reductase protein R2 from *Escherichia coli*. *Biochemistry* **2003,** *42* (45), 13269-13279.
99. Broadwater, J. A.; Ai, J.; Loehr, T. M.; Sanders-Loehr, J.; Fox, B. G., Peroxodiferric intermediate of stearoyl-acyl carrier protein Δ^9 desaturase: oxidase reactivity during single turnover and implications for the mechanism of desaturation. *Biochemistry* **1998,** *37* (42), 14664-71.
100. Bollinger, J. M., Jr.; Krebs, C.; Vicol, A.; Chen, S.; Ley, B. A.; Edmondson, D. E.; Huynh, B. H., Engineering the diiron site of *Escherichia coli* ribonucleotide reductase protein R2 to accumulate an intermediate similar to H_{peroxo}, the putative peroxodiiron(III) complex from the methane monooxygenase catalytic cycle. *J. Am. Chem. Soc.* **1998,** *120* (5), 1094-1095.
101. Broadwater, J. A.; Achim, C.; Münck, E.; Fox, B. G., Mössbauer studies of the formation and reactivity of a quasi-stable peroxo intermediate of stearoyl-acyl carrier protein Δ^9-desaturase. *Biochemistry* **1999,** *38* (38), 12197-12204.
102. Valentine, A. M.; Stahl, S. S.; Lippard, S. J., Mechanistic studies of the reaction of reduced methane monooxygenase hydroxylase with dioxygen and substrates. *J. Am. Chem. Soc.* **1999,** *121* (16), 3876-3887.
103. Kitajima, N.; Tamura, N.; Amagai, H.; Fukui, H.; Moro-oka, Y.; Mizutani, Y.; Kitagawa, T.; Mathur, R.; Heerwegh, K.; Reed, C. A.; Randall, C. R.; Que Jr., L.; Tatsumi, K., Monomeric carboxylate ferrous complexes as models for the dioxygen binding sites in non-heme iron proteins. The reversible formation and characterization of μ-peroxo diferric complexes. *J. Am. Chem. Soc.* **1994,** *116* (20), 9071-9085.
104. Zhang, X.; Furutachi, H.; Fujinami, S.; Nagatomo, S.; Maeda, Y.; Watanabe, Y.; Kitagawa, T.; Suzuki, M., Structural and spectroscopic characterization of (μ-hydroxo or μ-oxo)(μ-peroxo)diiron(III) complexes: models for peroxo intermediates of non-heme diiron proteins. *J Am Chem Soc* **2005,** *127* (3), 826-7.
105. Song, W. J.; Lippard, S. J., Mechanistic studies of reactions of peroxodiiron(III) intermediates in T201 variants of toluene/o-xylene monooxygenase hydroxylase. *Biochemistry* **2011,** *50* (23), 5391-5399.
106. Saleh, L.; Krebs, C.; Ley, B. A.; Naik, S.; Huynh, B. H.; Bollinger, J. M., Jr., Use of a chemical trigger for electron transfer to characterize a precursor to cluster X in assembly of the iron-radical cofactor of *Escherichia coli* ribonucleotide reductase. *Biochemistry* **2004,** *43* (20), 5953-5964.
107. Que, L., Jr.; Tolman, W. B., Bis(μ-oxo)dimetal "diamond" cores in copper and iron complexes relevant to biocatalysis. *Angew. Chem. Int. Ed.* **2002,** *41* (7), 1114-1137.
108. Girerd, J.-J.; Banse, F.; Simaan, A. J., Characterization and properties of non-heme iron peroxo complexes. *Struct. Bonding (Berlin)* **2000,** *97* (Metal-Oxo and Metal-Peroxo Species in Catalytic Oxidations), 145-177.
109. Moenne-Loccoz, P.; Krebs, C.; Herlihy, K.; Edmondson, D. E.; Theil, E. C.; Huynh, B. H.; Loehr, T., The ferroxidase reaction of ferritin reveals a diferric μ-1,2 bridging peroxide intermediate in common with other O_2-activating non-heme diiron proteins. *Biochemistry* **1999,** *38*, 5290-5295.
110. Fiedler, A. T.; Shan, X.; Mehn, M. P.; Kaizer, J.; Torelli, S.; Frisch, J. R.; Kodera, M.; Que, L., Jr., Spectroscopic and computational studies of (μ -Oxo)(μ -1,2-peroxo)diiron(III) complexes of relevance to nonheme diiron oxygenase intermediates. *J. Phys. Chem. A* **2008,** *112* (50), 13037-13044.

111. Frisch, J., R.; Vu, V., V.; Martinho, M.; Münck, E.; Que, L., Jr., Characterization of two distinct adducts in the reaction of a nonheme diiron(II) complex with O_2. *Inorg. Chem.* **2009,** *48* (17), 8325-36.
112. Roelfes, G.; Vrajmasu, V.; Chen, K.; Ho, R. Y. N.; Rohde, J.-U.; Zondervan, C.; la Crois, R. M.; Schudde, E. P.; Lutz, M.; Spek, A. L.; Hage, R.; Feringa, B. L.; Münck, E.; Que, L., Jr., End-on and side-on peroxo derivatives of non-heme iron complexes with pentadentate ligands: Models for putative intermediates in biological iron/dioxygen chemistry. *Inorg. Chem.* **2003,** *42* (8), 2639-2653.
113. Li, F.; Meier, K. K.; Cranswick, M. A.; Chakrabarti, M.; Van Heuvelen, K. M.; Münck, E.; Que, L., Jr., Characterization of a high-spin non-heme Fe^{III}−O intermediate and its quantitative conversion to an Fe^{IV} = O complex. *J. Am. Chem. Soc.* **2011,** *133* (19), 7256-7259.
114. Mirica, L. M.; Ottenwaelder, X.; Stack, T. D. P., Structure and spectroscopy of copper-dioxygen complexes. *Chem. Rev.* **2004,** *104* (2), 1013-1045.
115. Mathe, C.; Mattioli, T. A.; Horner, O.; Lombard, M.; Latour, J.-M.; Fontecave, M.; Niviere, V., Identification of iron(III) peroxo species in the active site of the superoxide reductase SOR from *Desulfoarculus baarsii*. *J. Am. Chem. Soc.* **2002,** *124* (18), 4966-4967.
116. Kitajima, N.; Moro-oka, Y., Copper-dioxygen complexes. Inorganic and bioinorganic perspectives. *Chem. Rev.* **1994,** *94* (3), 737-57.
117. Vetting, M. W.; Ohlendorf, D. H., Structural studies of protocatechuate 3,4-dioxygenase from Acinetobacter sp. ADP1. *Trans. Am. Cryst. Assoc.* **2001,** *35* (Using Crystallography to Understand Enzyme Mechanism), 65-73.
118. Elango, N.; Radhakrishnan, R.; Froland, W. A.; Wallar, B. J.; Earhart, C. A.; Lipscomb, J. D.; Ohlendorf, D. H., Crystal structure of the hydroxylase component of methane monooxygenase from *Methylosinus trichosporium* OB3b. *Protein Sci.* **1997,** *6* (3), 556-568.
119. Rosenzweig, A. C.; Frederick, C. A.; Lippard, S. J.; Nordlund, P., Crystal structure of a bacterial non-haem iron hydroxylase that catalyses the biological oxidation of methane. *Nature* **1993,** *366* (6455), 537-543.
120. Pacholec, M.; Sello, J. K.; Walsh, C. T.; Thomas, M. G., Formation of an aminoacyl-S-enzyme intermediate is a key step in the biosynthesis of chloramphenicol. *Org. Biomol. Chem.* **2007,** *5* (11), 1692-1694.
121. Vining, L. C.; Malik, V. S.; Westlake, D. W. S., Biosynthesis of chloramphenicol. *Lloydia* **1968,** *31* (4), 355-63.
122. Dunham, W. R.; Harding, L. J.; Sands, R. H., Mössbauer spectroscopy of metalloproteins and the use of Fourier transforms. *Eur. J. Biochem.* **1993,** *214*, 1-8.
123. Dibar-Ure, M. C.; Flinn, P. A., A technique for the removal of the" blackness" distortion of Mössbauer spectra In *Mössbauer Effect Methodology*, Gruverman, I. G., Ed. Plenum Press: New York, New York, 1971; Vol. 7, p 245−262.
124. Banerjee, R.; Meier, K. K.; Münck, E.; Lipscomb, J. D., Intermediate P* from soluble methane monooxygenase contains a diferrous cluster. *Biochemistry* **2013,** *52*, 4331–4342.
125. Rosenzweig, A. C.; Nordlund, P.; Takahara, P. M.; Frederick, C. A.; Lippard, S. J., Geometry of the soluble methane monooxygenase catalytic diiron center in two oxidation states. *Chem. Biol.* **1995,** *2* (6), 409-418.
126. Voegtli, W. C.; Khidekel, N.; Baldwin, J.; Ley, B. A.; Bollinger, J., J. M.; Rosenzweig, A. C., Crystal structure of the ribonucleotide reductase R2 mutant that accumulates a μ-1,2-peroxodiiron(III) intermediate during oxygen activation. *J. Am. Chem. Soc.* **2000,** *122*, 3255-3261.

127. Andersson, M. E.; Hoegbom, M.; Rinaldo-Matthis, A.; Andersson, K. K.; Sjoeberg, B.-M.; Nordlund, P., The crystal structure of an azide complex of the diferrous R2 subunit of ribonucleotide reductase displays a novel carboxylate shift with important mechanistic implications for diiron-catalyzed oxygen activation. *Journal of the American Chemical Society* **1999,** *121* (11), 2346-2352.
128. Boal, A. K.; Cotruvo, J. A., Jr.; Stubbe, J.; Rosenzweig, A. C., Structural basis for activation of Class Ib ribonucleotide reductase. *Science* **2010,** *329* (5998), 1526-1530.
129. Ambundo, E. A.; Friesner, R. A.; Lippard, S. J., Reactions of methane monooxygenase intermediate Q with derivitized methanes. *J. Am. Chem. Soc.* **2002,** *124* (30), 8770-8771.
130. Chavez, F., A.; Ho, R., Y. N.; Pink, M.; Young, V., G., Jr.; Kryatov, S., V.; Rybak-Akimova, E., V.; Andres, H.; Münck, E.; Que, L., Jr.; Tolman, W., B., Unusual peroxo intermediates in the reaction of dioxygen with carboxylate-bridged diiron(II,II) paddlewheel complexes. *Angew. Chem.* **2002,** *41* (1), 149-52.
131. Liu, K. E.; Valentine, A. M.; Wang, D. L.; Huynh, B. H.; Edmondson, D. E.; Salifoglou, A.; Lippard, S. J., Kinetic and spectroscopic characterization of intermediates and component interactions in reactions of methane monooxygenase from *Methylococcus capsulatus* (Bath). *J. Am. Chem. Soc.* **1995,** *117* (41), 10174-10185.
132. Krebs, C.; Bollinger, J. M., Jr.; Theil, E. C.; Huynh, B. H., Exchange coupling constant J of peroxodiferric reaction intermediates determined by Mössbauer spectroscopy. *J. Biol. Inorg. Chem.* **2002,** *7* (7-8), 863-9.
133. Hwang, J.; Krebs, C.; Huynh, B. H.; Edmondson, D. E.; Theil, E. C.; Penner-Hahn, J. E., A short Fe-Fe distance in peroxodiferric ferritin: Control of Fe substrate versus cofactor decay. *Science* **2000,** *287* (5450), 122-125.
134. Chufan, E. E.; Puiu, S. C.; Karlin, K. D., Heme-copper/dioxygen adduct formation, properties, and reactivity. *Acc. Chem. Res.* **2007,** *40* (7), 563-572.
135. Naruta, Y.; Sasaki, T.; Tani, F.; Tachi, Y.; Kawato, N.; Nakamura, N., Heme-Cu complexes as oxygen-activating functional models for the active site of cytochrome c oxidase. *J. Inorg. Biochem.* **2001,** *83* (4), 239-246.
136. Lewis, E. A.; Tolman, W. B., Reactivity of dioxygen-copper systems. *Chem. Rev.* **2004,** *104* (2), 1047-1076.
137. Li, F.; Van Heuvelen, K. M.; Meier, K. K.; Münck, E.; Que, L., Jr., Sc^{3+}-triggered oxoiron(IV) formation from O_2 and its non-heme iron(II) precursor via a Sc^{3+}-peroxo-Fe^{3+} intermediate. *Journal of the American Chemical Society* **2013,** *135* (28), 10198-201.
138. Lee, Y.-M.; Bang, S.; Kim, Y. M.; Cho, J.; Hong, S.; Nomura, T.; Ogura, T.; Troeppner, O.; Ivanovic-Burmazovic, I.; Sarangi, R.; Fukuzumi, S.; Nam, W., A mononuclear nonheme iron(III)-peroxo complex binding redox-inactive metal ions. *Chem. Sci.* **2013,** *4* (10), 3917-3923.
139. Dong, Y.; Zang, Y.; Kauffmann, K.; Shu, L.; Wilkinson, E. C.; Münck, E.; Que, L., Jr., Models for nonheme diiron enzymes. Assembly of a high-valent $Fe_2(\mu\text{-}O)_2$ diamond core from its peroxo precursor. *J. Am. Chem. Soc.* **1997,** *119* (51), 12683-12684.
140. Kodera, M.; Kano, K., Reversible O_2-binding and activation with dicopper and diiron complexes stabilized by various hexapyridine ligands. stability, modulation, and flexibility of the dinuclear structure as key aspects for the dimetal/O2 chemistry. *Bull. Chem. Soc. Jpn.* **2007,** *80* (4), 662-676.
141. Cranswick, M. A.; Meier, K. K.; Shan, X.; Stubna, A.; Kaizer, J.; Mehn, M. P.; Münck, E.; Que, L., Jr., Protonation of a peroxodiiron(III) complex and conversion to a diiron(III/IV) intermediate: Implications for proton-assisted O-O bond cleavage in nonheme diiron enzymes. *Inorg. Chem.* **2012,** *51* (19), 10417-26.

142. Costas, M.; Mehn, M., P.; Jensen, M., P.; Que, L., Jr., Dioxygen activation at mononuclear nonheme iron active sites: enzymes, models, and intermediates. *Chemical reviews* **2004,** *104* (2), 939-986.
143. Cho, J.; Jeon, S.; Wilson, S. A.; Liu, L. V.; Kang, E. A.; Braymer, J. J.; Lim, M. H.; Hedman, B.; Hodgson, K. O.; Valentine, J. S.; Solomon, E. I.; Nam, W., Structure and reactivity of a mononuclear non-heme iron(III)-peroxo complex. *Nature (London, U. K.)* **2011,** *478* (7370), 502-505.
144. Halime, Z.; Kieber-Emmons, M. T.; Qayyum, M. F.; Mondal, B.; Gandhi, T.; Puiu, S. C.; Chufan, E. E.; Sarjeant, A. A. N.; Hodgson, K. O.; Hedman, B.; Solomon, E. I.; Karlin, K. D., Heme-copper-dioxygen complexes: Toward understanding ligand-environmental effects on the coordination geometry, electronic structure, and reactivity. *Inorg. Chem.* **2010,** *49* (8), 3629-3645.
145. Platter, E.; Lawson, M.; Marsh, C.; Sazinsky, M. H., Characterization of a non-ribosomal peptide synthetase-associated diiron arylamine N-oxygenase from Pseudomonas syringae pv. phaseolicola. *Arch. Biochem. Biophys.* **2011,** *508* (1), 39-45.
146. Li, N.; Norgaard, H.; Warui, D. M.; Booker, S. J.; Krebs, C.; Bollinger, J. M., Jr., Conversion of fatty aldehydes to alka(e)nes and formate by a cyanobacterial aldehyde decarbonylase: Cryptic redox by an unusual dimetal oxygenase. *J. Am. Chem. Soc.* **2011,** *133* (16), 6158-6161.
147. Paul, B.; Das, D.; Ellington, B.; Marsh, E. N. G., Probing the mechanism of cyanobacterial aldehyde decarbonylase using a cyclopropyl aldehyde. *J. Am. Chem. Soc.* **2013,** *135* (14), 5234-5237.
148. Süssmuth, R. D.; Pelzer, S.; Nicholson, G.; Walk, T.; Wohlleben, W.; Jung, G., New advances in the biosythesis of glycopeptide antibiotics of the vancomycin type from *Amycolatopsis mediterranei*. *Angew. Chem. Int. Ed.* **1999,** *38*, 1976-1979.
149. McGrath, R. M.; Siddiqueullah, M.; Vining, L. C.; Sala, F.; Westlake, D. W. S., p-Aminophenylalanine and threo-p-aminophenylserine. Specific precursors of chloramphenicol. *Biochem. Biophys. Res. Commun.* **1967,** *29* (4), 576-581.
150. Westlake, D. W. S.; Vining, L. C., Biosynthesis of chloramphenicol. *Biotechnol. Bioeng.* **1969,** *11* (6), 1125-34.
151. Eyer, P.; Schneller, M., Reactions of the nitroso analogue of chloramphenicol with reduced glutathione. *Biochem. Pharmacol.* **1983,** *32* (6), 1029-1036.
152. Spain, J. C., *Biodegradation of Nitroaromatic Compounds*. Springer US: New York, 1995; p 232.
153. Saywell, L. G.; Cunningham, B. B., Determination of iron: Colorimetric o-phenanthroline method. *Ind. Eng. Chem. Anal. Ed.* **1937,** *9* (2), 67-69.
154. Rao, G. G.; Somidevamma, G., Volumetric determination of iron (III) with hydroxylamine as a reducing agent. *Fresen J. Anal. Chem. 165* (6), 432-436.
155. Wallar, B. J.; Lipscomb, J. D., Methane monooxygenase component B mutants alter the kinetics of steps throughout the catalytic cycle. *Biochemistry* **2001,** *40* (7), 2220-2233.
156. Liang, A. D.; Lippard, S. J., Component interactions and electron transfer in toluene/o-xylene monooxygenase. *Biochemistry* **2014,** *53* (47), 7368-7375.
157. Bailey, L. J.; Acheson, J. F.; McCoy, J. G.; Elsen, N. L.; Phillips, G. N., Jr.; Fox, B. G., Crystallographic analysis of active site contributions to regiospecificity in the diiron enzyme toluene 4-monooxygenase. *Biochemistry* **2012,** *51* (6), 1101-1113.
158. Bollinger, J. M., Jr.; Diao, Y.; Matthews, M. L.; Xing, G.; Krebs, C., myo-Inositol oxygenase: a radical new pathway for O_2 and C-H activation at a nonheme diiron cluster. *Dalton Trans.* **2009,** (6), 905-914.

159. Tinberg, C. E.; Lippard, S. J., Oxidation reactions performed by soluble methane monooxygenase hydroxylase intermediates H_{peroxo} and Q proceed by distinct mechanisms. *Biochemistry* **2010,** *49* (36), 7902-7912.
160. Xing, G.; Barr, E. W.; Diao, Y.; Hoffart, L. M.; Prabhu, K. S.; Arner, R. J.; Reddy, C. C.; Krebs, C.; Bollinger, J. M., Jr., Oxygen activation by a mixed-valent, diiron(II/III) cluster in the glycol cleavage reaction catalyzed by myo-inositol oxygenase. *Biochemistry* **2006,** *45* (17), 5402-5412.
161. Komor, A. J.; Rivard, B. S.; Fan, R.; Guo, Y.; Que, L., Jr.; Lipscomb, J. D., Mechanism for six-electron aryl-N-oxygenation by the non-heme diiron enzyme CmlI. *J. Am. Chem. Soc.* **2016,** *138* (23), 7411-7421.
162. Petasis, D. T.; Hendrich, M. P., Quantitative interpretation of multifrequency multimode EPR spectra of metal containing proteins, enzymes, and biomimetic complexes. *Methods Enzymol.* **2015,** *563*, 171-208.
163. Groce, S. L.; Miller-Rodeberg, M. A.; Lipscomb, J. D., Single-turnover kinetics of homoprotocatechuate 2,3-dioxygenase. *Biochemistry* **2004,** *43* (48), 15141-15153.
164. Whittaker, J. W.; Lipscomb, J. D., Transition state analogs for protocatechuate 3,4-dioxygenase. Spectroscopic and kinetic studies of the binding reactions of ketonized substrate analogs. *J. Biol. Chem.* **1984,** *259* (7), 4476-86.
165. Vergé, D.; Arrio-Dupont, M., Interactions between apoaspartate aminotransferase and pyridoxal 5'-phosphate. A stopped-flow study. *Biochemistry* **1981,** *20* (5), 1210-1216.